Dissertation

submitted to the
Faculty of Mathematics and Physics
of the University of Freiburg, Germany
for the degree of
Doctor of Natural Sciences

Put forward by
Arturo Rodríguez Rodríguez
born in Havana

universität freiburg

Characterization of Silicon Strip Modules for the ATLAS Inner Tracker and Passive CMOS Strip Sensors for Future Collider Experiments

Dissertation

zur Erlangung des Doktorgrades
der Fakultät für Mathematik und Physik
der Albert-Ludwigs-Universität Freiburg im Breisgau

Vorgelegt von:

Arturo Rodríguez Rodríguez

June 2023

Dekan:

Prof. Dr. Michael Thoss

1. Gutachter:

Dr. Ulrich Parzefall

2. Gutachter:

Prof. Dr. Markus Schumacher

Datum der Prüfung:

26.09.2023

Abstract

The ALTAS experiment will replace its Inner Detector with an all-silicon Inner Tracker (ITk) to cope with the stringent requirements of detector occupancy and radiation damage expected during the High-Luminosity LHC (HL-LHC) operation period. The ITk consists of a pixel and a strip detector. An exhaustive R&D program has been carried out to guarantee that the new radiation-hard sensors and readout electronic deliver the required performance. In addition, a series of beam test campaigns have been performed to characterize the strip module prototypes. This work analyzes the performance of ITk Strip barrel and endcap modules before and after irradiation to the maximum expected fluence, including safety factors. The analysis of the hit detector efficiency, noise occupancy, and resolution showed that the current modules satisfied the operational requirements of the ITk Strip detector, ensuring satisfactory performance during their entire operational lifetime at the HL-LHC.

As the physics potential of other collider experiments with higher energies and luminosities is under study, it is crucial to investigate new sensor technologies that allow producing large areas of radiation-hard sensors cost-effectively. CMOS sensors are attractive as the technology is widely available in commercial foundries. This thesis studies novel passive CMOS sensors fabricated using the 150 nm CMOS process from LFoundry. Up to five reticles were stitched together to produce sensors up to four times the individual reticle size. Electrical characterization and charge collection measurements before and after irradiation showed that the stitching process has no impact on the electrical behavior and the amount of collected charge. Moreover, the sensors collected the expected amount of charge before irradiation and exhibited performance consistent with radiation-induced degradation after irradiation. The results presented in this thesis demonstrate that the CMOS technology and the reticle stitching process can be successfully employed to produce large-area silicon sensors for applications in high-energy particle detectors.

Zusammenfassung

Das ALTAS-Experiment wird seinen derzeitigen inneren Detektor durch einen ausschließlich mit Siliziumsensoren bestückten inneren Tracker (ITk) ersetzen, um den strengen Anforderungen an die Detektorbelegung und die Strahlungsschäden gerecht zu werden, die während des Betriebs am LHC (HL-LHC) zu erwarten sind. Der ITk besteht aus einem Pixel- und einem Streifendetektor. Es wurde ein umfassendes R&D-Programm durchgeführt, um sicherzustellen, dass die neuen strahlungsharten Sensoren und die Ausleseelektronik die erforderliche Leistung erbringen. Darüber hinaus wurde eine Reihe von Testbeam-Kampagnen durchgeführt, um die Prototypen der Streifenmodule zu charakterisieren. In dieser Arbeit wird die Leistung der ITk Strip Barrel- und Endcap-Module vor und nach der Bestrahlung mit der inklusive Sicherheitsfaktoren maximal erwarteten Fluenz analysiert. Die Analyse der Effizienz des Detektors, der Rauschbelegung und der Auflösung hat gezeigt, dass die aktuellen Module die Anforderungen des ITk-Strip-Detektors erfüllen und während ihrer gesamten Betriebsdauer am HL-LHC eine ausreichende Leistung gewährleisten.

Für geplante neue Collider-Experimente mit höheren Energien und Luminositäten ist es von entscheidender Bedeutung, neue Sensortechnologien zu erforschen, die es ermöglichen, große Flächen strahlungsharter Sensoren kostengünstig herzustellen. CMOS-Sensoren sind attraktiv, da diese Technologie in kommerziellen Foundries weithin verfügbar ist. In dieser Arbeit werden neuartige passive CMOS-Streifensensoren untersucht, die mit dem 150 nm CMOS-Prozess von LFoundry hergestellt wurden. Bis zu fünf Reticles wurden zusammengefügt, um Sensoren mit einer bis zu vierfachen Größe der Stitches herzustellen. Elektrische Charakterisierung und Ladungssammlungsmessungen vor und nach der Bestrahlung zeigen, dass der Stitching-Prozess keinen Einfluss auf das elektrische Verhalten und die Menge der gesammelten Ladung hat. Die untersuchten CMOS-Sensoren zeigen sowohl vor als auch nach der Bestrahlung die erwartete Ladungssammlungseffizienz. Die in dieser Arbeit vorgestellten Ergebnisse zeigen, dass die CMOS-Technologie und das Stitching-Verfahren erfolgreich eingesetzt werden können, um großflächige Siliziumsensoren für Anwendungen in Teilchendetektoren in der Hochenergiephysik herzustellen.

Contents

List of Figures

List of Tables

Chapter 1

Introduction

The use of solid-state detectors in physics dates back to the early ideas of solid-state ionization chambers developed in 1943 [1]. With the pioneering work of Shockley on the p-n junction [2] and the invention of the bipolar transistor at the Bell Laboratories in 1949 [3], an unparalleled technological development started, which led to the discovery of the excellent photon and charged particle detection capabilities of silicon and germanium. As early as 1949, the first semiconductor detector was developed as a germanium counter [4]. In the 1960s, semiconductor detectors were already present in particle physics, nuclear physics, and astronomy. Developing more sophisticated fabrication techniques allowed producing high-quality semiconductor materials with improved properties, advancing detector designs, enabling better energy resolution, increased sensitivity, and enhanced efficiency.

Further developments, in the form of "miniature particle spectrometers", were motivated by the nuclear and research industry.In 1980, Heijne and Jarron introduced the silicon microstrip detector with a parallel readout for tracking in particle physics experiments [5]. Josef Kemmer transferred the highly developed silicon technology from electronic manufacturing to detector fabrication in the late 70s [6]. Consequently, the first silicon strip detectors fabricated using the planar technology were employed in the NA11 experiment at European Council for Nuclear Research (CERN by its French acronym) in 1983 [7].

The great success of the NA11 experiment in measuring charm physics properties demonstrated the excellent performance of Si-strip detectors and, later, pixel detectors in the NA32 experiment. Subsequent collider experiments further highlight the importance of silicon detectors in particle physics. The unstoppable progress of the semiconductor industry, especially in close collaboration with the scientific community, allowed for lower costs, smaller feature sizes, and faster development times. Therefore, for the last 30 years, silicon detectors have been a cornerstone of every collider experiment's central tracking detector technology, including the four large experiments at the Large Hadron Collider (LHC).

The discovery of the Higgs boson in 2012 by the ATLAS [8] and CMS [9] collaborations at CERN confirmed the mechanism behind the origin of the mass of subatomic particles within the Standard Model (SM). While the SM successfully describes the fundamental particles and their interactions, it leaves unanswered questions and gaps in our understanding of the universe arising from astronomical observations and neutrino oscillation [10]. The SM model does not incorporate gravity [11] or explain the nature of dark matter [12] and dark energy [13], which constitute a significant portion of the universe's mass that remains up to now undetectable by current experiments. In addition, it does not explain the matter-antimatter asymmetry [14] or why neutrinos have mass [15]. These phenomena have opened the doors to further theories, like supersymmetry, extra dimensions, and grand unification [10], commonly known as "Beyond Standard Model" theories.

To explore these lines of research and continue precision measurements of the SM parameters, the LHC at CERN will receive a boost in the number of particles colliding simultaneously. This upgrade, known as High-Luminosity LHC (HL-LHC) [16], will allow the scientific community, particularly from the ATLAS and CMS collaborations, to reach unseen levels of precision in physics analysis and observe rare new phenomena that might reveal themselves.

The accelerator upgrade will pose stringent requirements for the sensors. High track densities will increase detector occupancy and radiation damage. The detectors will have to endure integrated radiation doses five to ten times higher than at the LHC over the lifetime of the HL-LHC period [17, 18]. Because radiation damage deteriorates the performance of the sensors, it is critical that the employed sensor technology can deliver a signal-to-noise ratio large enough to maintain detection efficiency and track reconstruction requirements during the entire lifetime of the experiment.

The tracking systems currently installed in the LHC experiments are unable fully profit from the accelerator upgrade as they can not cope with the radiation damage and tracking requirements during operation at the HL-LHC. Therefore, the experiments are upgrading their tracking systems. The work presented in this thesis was conducted in the framework of the Tracking Detector upgrade of the ATLAS experiment in preparation for the LHC upgrade, focusing on the beam test characterization of silicon strip detector modules before and after irradiation.

In addition, given the ongoing study of the physics potential of collider experiments with higher energies and luminosities, exploring novel sensor technologies that enable the cost-effective production of large radiation-hard sensor areas is imperative. Looking at sensor requirements beyond LHC experiments, a feasibility study of using CMOS standard processes for silicon strip sensors is also presented.

The thesis is outlined as follows:

Chapter 2 introduces the Large Hadron Collider and the ATLAS Experiment. It discusses the LHC and the ATLAS Experiment with an overview of the current ATLAS Inner Detector. The HL-LHC and the ATLAS detector upgrade are also introduced and discussed. Finally, the new ATLAS Inner Tracker, particularly the Strip Detector modules, including its components, such as strip sensors and front-end electronics, are described.

Chapter 3 examines silicon detectors in particle physics experiments. The chapter begins with a short review of the main interaction mechanisms of particles with matter. The properties of silicon are then discussed, followed by an overview of silicon sensors, including doping, p-n junction properties, and diode characteristic curves. The chapter also covers signal formation in silicon detectors and radiation damage, particularly its effect on the sensor bulk. The working principle of silicon strip sensors for tracking, sources of noise, and detector operation is also discussed.

Chapter 4 details the beam test measurements conducted at the DESY-II accelerator. A detailed description of the ATLAS ITk Strip beam test setup is provided, followed by a discussion of data-taking procedures. It also covers the reconstruction and analysis of the beam test data and the particularities of the reconstruction using the Corryvreckan framework. The chapter concludes with discussions of spatial resolution, hit reconstruction efficiency, noise occupancy, and the electrical characterization of ITk Strip modules at the beam test.

Chapter 5 presents the analysis results of beam test measurements conducted at the DESY-II test beam facility from the barrel and endcap ITk Strip detector modules. The analysis evaluates module performance regarding hit detection efficiency, position resolution, and optimal operating threshold. In addition, the threshold dependence of module observables, like the hit detection efficiency, noise occupancy, and resolution, is discussed. Finally, the reconstruction of space points from strip stereo layers is evaluated.

A feasibility study for evaluating Passive CMOS Strip sensors produced in a commercial foundry is presented in Chapter 6. The chapter includes an overview of CMOS technology in particle detectors and the particularities of the reticle stitching process employed in manufacturing the investigated sensors. It describes the investigated designs and presents results from the electrical characterization and charge collection measurements before and after irradiation.

Finally, the conclusions are presented in Chapter 7.

Chapter 2

The Large Hadron Collider and the ATLAS Experiment

2.1. The Large Hadron Collider

The Large Hadron Collider (LHC) [19], the most precise synchrotron ever built, is part of the European Organization for Nuclear Research's (CERN) accelerator complex, shown in Figure 1. The LHC, located in Geneva at the border between Switzerland and France and about 100 m underground, combines superconducting magnets with several acceleration stages in a 26.7 km circumference.

Two proton beams circulate near the speed of light inside the machine in opposite directions in two different beam pipes, providing proton-proton (p-p) collisions at a center of mass energy of 13 TeV every 25 ns (bunch-crossing) at the four collision points. Superconducting magnets drive the beams, and insertion quadrupole magnets squeeze them to increase collision probability.

The LHC's center of mass energy for collisions is not the only exceptional parameter of the accelerator. Its instantaneous luminosity also achieves unparalleled values. The collider instantaneous luminosity is the ratio between the number of produced events in a given time and the cross-section of the process:

$$\mathcal{L} = \frac{1}{\sigma}\frac{\mathrm{d}N}{\mathrm{d}t}$$

where $\mathrm{d}N/\mathrm{d}t$ is the event rate and σ the interaction cross-section. The luminosity is given in units of $\mathrm{cm}^{-2}\mathrm{s}^{-1}$ and measures the accelerator performance. Additionally, the integrated luminosity measures how much useful data the machine can deliver in a defined time. The LHC has a nominal instantaneous luminosity of 10^{34} $\mathrm{cm}^{-2}\mathrm{s}^{-1}$, and after Run[1] 3, it is foreseen to have delivered a total integrated luminosity of approximately 400 fb^{-1} [21].

---

[1] A data-taking period is known as Run, while a technical maintenance period is called Long Shutdown (LS)

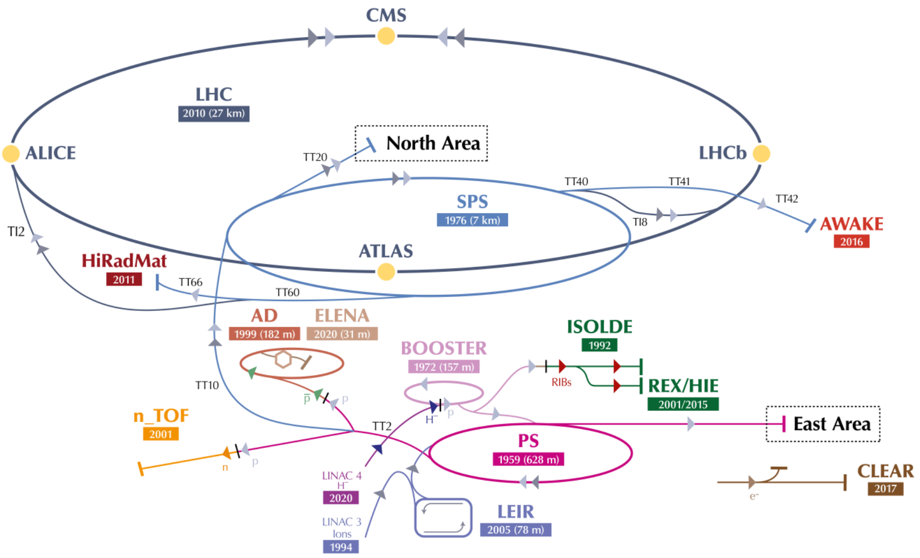

Figure 1.: The CERN accelerator complex. The LHC is the largest ring and the last acceleration stage for protons and heavy ions. Particles go through smaller accelerators to boost their energy before entering the final stage at the LHC. Light and dark gray triangles depict the path followed by protons and heavy ions. In addition, the smaller machines provide beams to many other experiments and beam test and irradiation facilities (adapted from [20]).

Every proton accelerated at the LHC starts with extracting a Hydrogen atom, whose electrons are stripped. The protons are then injected into the *Booster* at an energy of 50 MeV from the *Linac2*. The Booster accelerates them to 1.4 GeV after delivering to the *Proton Synchroton* (PS), where they reach an energy of 25 GeV. The protons are then fed to the *Super Proton Synchroton* (SPS), where the protons' energy is boosted to 450 GeV before transferring them to the LHC. In the LHC, during Run 2, protons are accelerated for 20 minutes to 6.5 TeV.

The LHC's high energy and luminosity make the accelerator unique, allowing the outstanding physics program of its four large-scale experiments. While the high interaction rates, energies, and particle multiplicities are desired for physics measurements, they impose stringent conditions on the detectors regarding radiation damage, triggering, and data transfer. The requirement for more precise measurements of SM processes and searches for Beyond Standard Model (BSM) physics led to new design standards for multipurpose particle detectors.

There are two general-purpose detectors, ATLAS [22] (an acronym for A Toroidal LHC ApparatuS) and CMS [23] (Compact Muon Solenoid), which are designed to explore p-p and, to a lesser extent, Pb-Pb collisions. Two more specific detectors, LHCb (Large Hadron Collider beauty) [24] and ALICE (A Large Ion Collider Experiment) [25] exist. The LHCb physics program is focused on bottom and charm quark physics, and ALICE investigates the Quark-Gluon Plasma in Pb-Pb collisions.

In 2012, the program had its crowning moment when the ATLAS [8] and CMS [9] collaborations announced the discovery of the Higgs boson. The discovery led to the Nobel Prize in Physics for Peter Higgs and François Englert in 2013, confirming the existence of the Higgs field and the mechanism behind how particles acquired mass.

The LHC has been in operation since 2008, with subsequent data-taking and technical maintenance periods. There have been two Run periods. In Run 1, the machine operated at an energy of 7 TeV and later at 8 TeV until 2013. The first Long Shutdown (LS 1) ended in early 2015, and during Run 2, the LHC delivered proton-proton collisions at a center of mass energy of 13 TeV and reached its design luminosity. LS 2 started in 2019 and was scheduled to end by 2021. Due to the Covid-19 pandemic, LS 2 was extended until 2022.

Run 3 started in July of 2022, and the LHC has provided p-p collisions at 13.6 TeV center-of-mass energy. At the end of Run 3, the accelerator is expected to operate at its design energy of 14 TeV. The current future of the LHC includes an LS 3, during which a major performance upgrade will increase the machine luminosity to unprecedented values. This phase is known as the *High-Luminosity LHC* (HL-LHC)[2]. During LS3, the ATLAS and the CMS experiments will also introduce major upgrades to their detectors to cope with the new challenges imposed by the new operating parameters of the LHC. The HL-LHC physics program focuses on more precise measurements of the Higgs coupling to Standard Model particles, BSM physics, and dark matter searches.

2.2. The ATLAS Experiment

The ATLAS detector is a multipurpose detector with a height of 25 m, a width of 44 m, and a weight of 7000 t [22]. A schematic view of the detector, built around the LHC beam pipe, is shown in Figure 2. The ATLAS detector comprises three detector subsystems whose designs allow for particle identification and measurements of their properties.

From the beam pipe[3] and moving up in radius, the first subsystem is the Inner Detector (ID) [26, 27], which provides measurements of charged particle tracks with high efficiency. The ID consists of the Pixel Detector [28, 29], the Semiconductor Tracker (SCT) [30, 31, 32], and the Transition Radiation Tracker (TRT) [33, 34, 35]. In May 2014, a new layer, the Insertable B-Layer (IBL) [36], was installed 3.3 cm from the beam pipe. An exploded technical view of the ID and all its subdetectors is shown in Figure 3. The ID runs immersed in the magnetic field supplied by the solenoid magnet [37].

---

[2] It is also called Phase-II LHC Upgrade

[3] The beam pipe runs through the middle of the detector in Figure 2

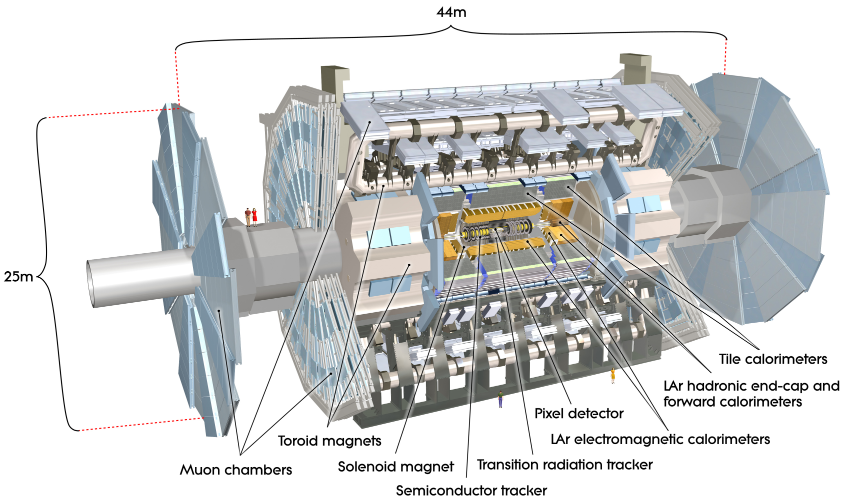

Figure 2.: Computer generated cut-away view of the entire ATLAS detector. The different subsystems are labeled [22].

The calorimeter system [38] is located around the ID. The system comprises a liquid Argon (LAr) electromagnetic sampling calorimeter [39] and a hadronic calorimeter [40] built of steel-scintillator-tiles in the barrel region and LAr in the endcaps. The muon detector subsystem [41] is positioned in the outermost region, and it is composed of drift tubes and resistive-plate, cathode-strip, and thin-gap chambers. All systems are within a toroidal magnetic field [42].

ATLAS uses a right-handed coordinate system with the origin in the interaction point and the z-axis running along the beamline. The xy plane, known as the transverse plane, is oriented with the positive x-axis pointing to the center of the LHC. The transverse plane is regularly described in $r - \phi$ coordinates with the azimuthal angle ϕ measured from the x-axis around the beam. The radial coordinate (r) measures the distance from the beamline, and the polar angle θ is defined from the positive z-axis. For most of the physics analysis, the polar angle is better represented by the so-called pseudorapidity, defined as $\eta = -\ln\tan(\theta/2)$. The pseudorapidity is also used to describe the detector layout.

2.3. The ATLAS Inner Detector

The Inner Detector aims to measure charged particles' position and transverse momentum (p_T) as they travel across the detector. The system is built with almost 100 million channels (fine granularity) to cope with the high particle densities produced by proton-proton collisions. The high granularity allows transverse momentum resolutions of $\sim 0.1\%$ and a reconstruction efficiency higher than 95% for isolated leptons in the TeV range [26, 27].

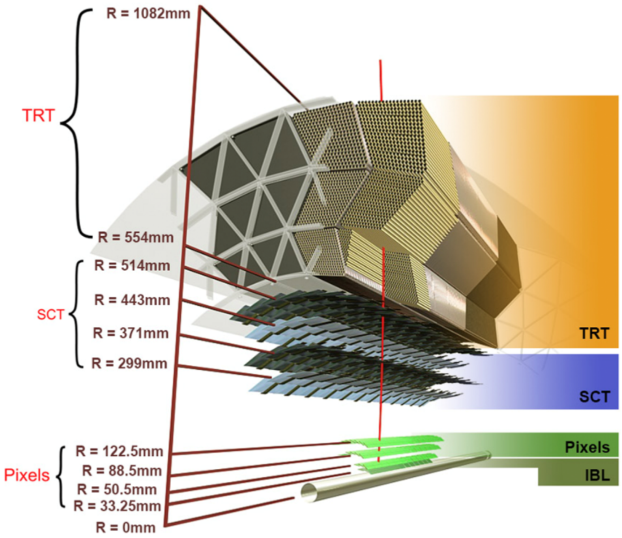

Figure 3.: Computer generated sectional view of the ATLAS Inner Detector. The different subdetectors and their position in radius with respect to the beam pipe are marked (adapted from [43]).

The solenoid magnet surrounding the ID provides a 2 Tesla magnetic field that curves the particle trajectories, allowing the track and momentum reconstruction. Only charged particles with transverse momentum above 500 MeV are reconstructed in the ID. The ID also keeps the amount of material to a minimum to reduce the effects of multiple scattering and electromagnetic showers (Sections 3.1.3 and 3.1.4). In addition, the ID has withstood the radiation damage (Section 3.5) created by the LHC environment, and it has maintained the required performance during Run 1 and Run 2.

Table 1 summarizes some of the main features of each subdetector that build the ID. The Pixel detector consists of three barrel layers plus the IBL and two endcaps of three disks each. The pixel modules are built from silicon n^+-in-n pixel sensors with a pitch of 50×400 µm^2, 16 Front-End (FE) readout chips, and a hybrid that controls the detector, provides power for the readout and the biasing of the sensor and data transmission. In the IBL, the pixel size is 50×250 µm^2, and 25 % of the modules use the novel 3D-sensor [44] technology. The inclusion of the IBL aimed to mitigate the effects of module failure due to radiation damage.

The SCT has four detector layers in the barrel region and two endcaps with nine discs each. The detector modules are built with two p^+-in-n silicon strip sensors, glued back-to-back with a 40 mrad stereo-angle to provide a two-dimensional measurement of the hits. Each sensor has 768 strips, and the barrel sensors have a rectangular geometry with a pitch of 80 µm. The sensors are fan-shaped with nearly radial strips in the endcaps, and the pitch varies from 54.4 to 94.8 µm.

Table 1.: Main features of the different subdetector systems of the Inner Detector [45].

Feature	Pixel detector	SCT	TRT
Area/Volume	1.9 m^2	60 m^2	12 m^3
Channels	92 millions	6 millions	350 thousands
Modules/Straws	1736 (barrel) 288 (endcap)	4,088 (two-sided)	50,000 (Barrel) 250,000 (endcap)
$\lvert\eta\rvert$ coverage	2.5	2.5	2.0

The azimuthal angle ϕ is measured with high precision for both types. The z-coordinate in the barrel and the radial distance R from the beam axis are determined with less precision. The modules are read out by six radiation-hard ASICs, with 128 channels each, on both sides of the module. The SCT can measure between four and nine hits per particle with 17 μm resolution in the $r - \phi$ plane and 580 μm along z.

The TRT is the largest of the subdetectors in the ID. It provides about 36 hits per particle with a precision of about 170 μm. In addition, when particles cross the boundary between two media with different dielectric constants, transition radiation [46] is emitted. This radiation allows particle identification, particularly for electrons and hadrons between 1 GeV/c and 150 GeV/c [10].

2.4. High-Luminosity LHC and the ATLAS Upgrade

From the beginning of its operation in 2010 until the end of Run 2, the LHC has delivered 190 fb^{-1} of proton-proton collisions. This integrated luminosity has served to the development of an intense program in fundamental physics by the different associated experiments.

A sequence of upgrades is expected for the accelerator to continue the physics program, including the search for dark matter and supersymmetry and pushing the standard model predictions to unparalleled limits with more precision measurements in the Higgs sector. The upgrades will occur during the LS 3, and Run 4 is scheduled to start in 2029 (HL-LHC) [16].

After the upgrades, the instantaneous luminosity of the collider will increase by a factor of seven. In parallel to the tenfold increment in the delivered data, the number of inelastic proton-proton collisions per bunch crossing (pile-up) will rise from $\langle\mu\rangle \sim 50$ to $\langle\mu\rangle \sim 200$ [47].

Under the conditions above, the current ATLAS Inner Detector would be inoperable. The current pixel and strip systems were designed for operating after accumulated radiation damage corresponding to 850 and 700 fb^{-1} integrated luminosities, respectively. To continue operations beyond that point would imply a decrease in the charge collection efficiency, an increase in leakage current, and the risk of thermal runaway, surpassing the cooling system and power supplies capabilities. Radiation damage will also impact the readout electronics with the corresponding decline in performance. Finally, the increase in detector occupancy due to pile-up would result in near 100% occupancy of the TRT, compromising pattern recognition and track reconstruction efficiency.

Faced with the above-mentioned challenges, the ATLAS Collaboration is building a new Inner Tracker to maintain the current Inner Detector performance under more challenging conditions.

2.5. The New ATLAS Inner Tracker

The ATLAS detector will be upgraded with a new all-silicon Inner Tracker for the HL-LHC period, known as the ITk. The new detector comprises a pixel [18] and strip [17] system. Figure 4 shows a sketch of the layout of the ITk depicting the pixel (red) and strip (blue) systems.

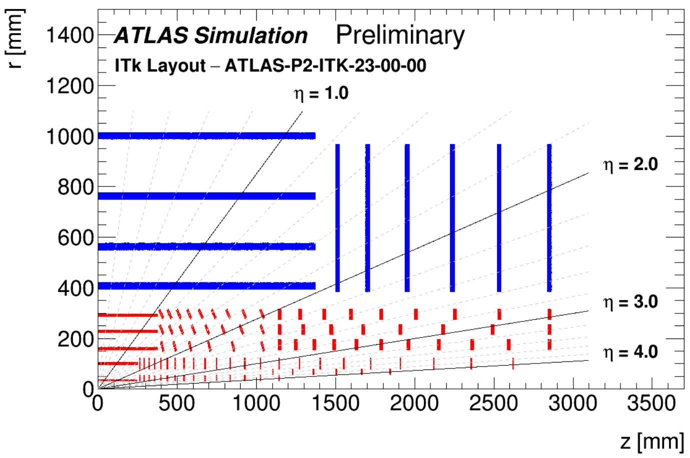

Figure 4.: Current ATLAS ITk layout used for physics benchmark studies [48]. Only one-quarter of the ITk is shown. The ITk Pixel is depicted in red, while the ITk Strip detector is blue. The horizontal axis is the axis along the beamline, with zero being the interaction point

Both systems consist of barrel layers in the central region around the interaction point and two endcaps in the forward region. The design features high modularity and an extension of the pseudorapidity coverage from $|\eta| \leq 2.5$ to $|\eta| \leq 4$. It also provides at least nine space points per track. The detector will use n^+-in-p silicon sensors, which are more radiation-hard than the commonly employed p^+-in-n (Section 3.5). The pixel system uses planar and 3D sensors, while the strip only uses planar sensors. The design reduces material with respect to the current ID by using an evaporative CO_2 cooling system with titanium pipes, carbon structures for mechanical stability, and the optimization of readout cabling using link sharing [18]. The ITk detector, designed with more radiation hard sensors and readout electronics, is expected to maintain, if not improve, the tracking performance of the current ID under more demanding conditions.

2.6. ATLAS ITk Strip Detector

The ATLAS ITk Strip detector is positioned around the pixel system covering a silicon area of ~ 165 m^2. The system is six meters long and comprises a central barrel region and two endcaps. The barrel is constructed using four cylinders surrounding the beam pipe, and the endcaps have six disks each. The primary mechanical support of the barrel is the stave. For the endcaps, each disk is built from the so-called petals. Both structures feature a central low-mass carbon core for mechanical stability and module support. They also house the common electrical, optical, and cooling services and offer precise alignment and fixation points. In addition, every stave and petal has an end-of-substructure card (EoS), which channels all the power and data links and serves as the interface to the off-detector electronics.

Barrel layers consist of several staves, ranging from 28 in the innermost layer to 72 in the outermost. Each stave is populated with 28 detector modules, 14 on each stave side. The two innermost layers are equipped with Short Strip (SS) detector modules, and the two outer layers are populated with Long Strip (LS) modules. The SS modules feature a rectangular sensor with a strip length of 24.1 mm, while the strips of LS modules are 48.2 mm long. The modules are rotated by ± 26 mrad with respect to the beamline on each side of the staves giving a total stereo angle of 52 mrad. In addition, the sensors on the staves are tilted by approximately 12° in the $r-\phi$ plane to ensure closure between neighboring sensors for tracks with momentum below 1 GeV [17].

Wedge-shaped structures, known as petals, are the mechanical building block of the endcaps. An endcap disk comprises 32 identical petals, and each petal has six modules per side, named R0-R5 (Ring 0-5) from the lowest to the highest radius, covering the whole petal surface. The three outermost modules (R3-R5) have two equal sensors, while in the three inner rings (R0-R2), the modules consist of only one sensor. The sensors have a 20 mrad stereo angle directly implemented in the sensor design. A total stereo angle of 40 mrad is obtained at the sensor's center when they are glued back to back. Staves and petals are loaded into the global support structures, which are part of the common mechanics of the ATLAS ITk [17].

The highly modular design allows multiple-site construction, making the construction effort of the tracking system worldwide, with more than 20 participating institutes.

2.7. ITk Strip Modules

The primary unit of the ITk Strip detector is the silicon-strip detector module. Barrel and endcap modules use the same conceptual module design and use comparable components. However, the ITk Strip employs eight different module designs, two in the barrel and six in the endcaps, as mentioned in Section 2.6. A strip module is built from one or two silicon sensors, flexible printed circuit boards (PCB) called hybrids [17], and one powerboard [49] glued directly onto the sensor. The number of hybrids depends on the module type and ranges from one to four. Figure 5 shows an exploded technical view and a picture of a barrel SS module where the different components are depicted and labeled.

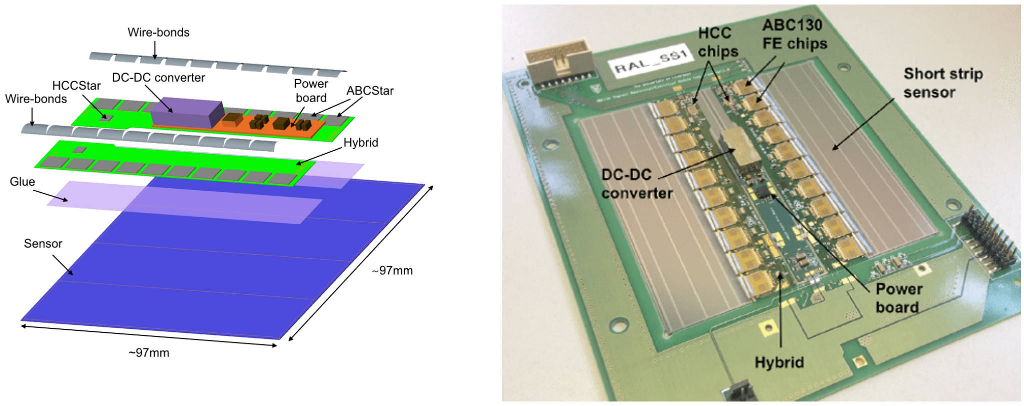

(a) **(b)**

Figure 5.: (a) Exploded view of a Short Strip module with labeled components and "Star" electronics [17]. (b) Picture of Short Strip module on a test frame [50].

The hybrids hold the front-end Application-Specific Integrated Circuits (ASICs) named ATLAS Binary Chip (ABC) and an aggregator chip called Hybrid Control Chip (HCC). The modules studied in this thesis use two different chip prototypes, the ABC130 [51] and the ABCStar [50], where the latter is the final version that will be employed in the experiment. The powerboards contain a DC-DC converter, a monitoring and control chip, and a high-voltage bias filter. The ASICs are glued onto the hybrids, and all connections are implemented via wire bonding using 25 µm thick aluminum wires.

2.7.1. Strip Sensors

The ITk Strip modules feature 320 µm thick n^+-in-p floatzone silicon sensors implemented on 6-inch wafers. The strips are AC-coupled, and biasing is achieved via resistors implemented by poly-silicon implants [52]. The strip isolation is implemented using p-stops implants [53].

The sensors are rectangular in the barrel, with an active area of approximately 10 × 10 cm^2. The strips are parallel to the sensor edge with a pitch of 75.5 μm. Each sensor has 1280 channels. For the endcap, the sensors have a wedge shape (with curved edges), as shown in Figure 6. This geometry is called *Stereo Annulus* [54]. The inner and outer edges are concentric arcs of a circumference centered in the beam axis. The two sides are straight, but their origin, named the focal point, is rotated by the 20 mrad stereo angle concerning the center of the discs. The sensors need to measure the azimuthal angle ϕ, and the radius R. Therefore, the strips are not parallel but have a common origin in the focal point. The strip length is optimized to keep occupancy below 1% [17].

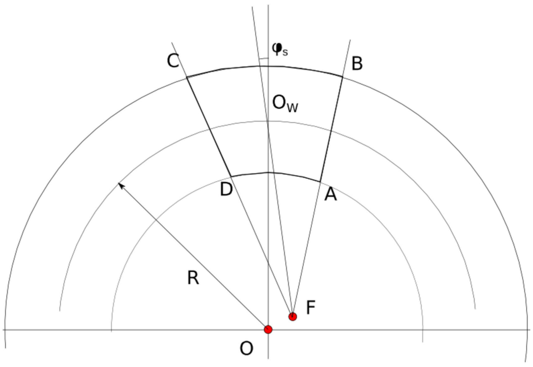

Figure 6.: Radial geometry of the ATLAS ITk Strip endcap sensors. The lower (arc DA) and upper (arc CB) edges of the sensor have their center in the beam axis O. The lateral edges, CD and AB, and the strips point to the "focal" point F, displaced by the stereo angle of 20 mrad [17].

Consequently, the sensors have two or four rows of strips with lengths varying from 19.0 mm in the innermost ring to 60.1 mm in the outermost region. Having radial strips imply a constant angular pitch for each strip row. To facilitate the bonding to the readout AISC, the strip pitch was kept as close as possible to 75.5 μm at the bond pad region, allowing direct wire bonding between the read-out ASIC and the sensor. As a result, the strip pitch ranges from 70 to 80 μm [54]. The angular pitch changes for different strip rows and varies from 85.7 to 193.1 μrad [53].

2.7.2. Front-end, Hybrids, and Powerboard

Two sets of front-end electronics ASICs, developed in the Global Foundries 130 nm CMOS process, have been studied. The first set is composed of the ABC130 and HCC130 chips. The second set comprises the ABCStar and the HCCStar ASICs. The second group was developed due to the change in the trigger rates from 500 kHz to 1 MHz for the ATLAS upgrade, where studies showed that the ABC130 and HCC130 could not handle the increased trigger rate [17].

The principal difference between the two sets is the interface between the ABCs and the HCCs, as seen in Figure 7. The 130 chipset uses a daisy-chain readout architecture, where the data are serially transmitted through a group of ABCs to the HCC. Data are also serially sent in the "Star" chipset, but in this case, each ABCStar has a direct connection to the HCCStar. The star configuration removes the bandwidth bottleneck in transferring data to the HCC while reducing the complexity of the system [50].

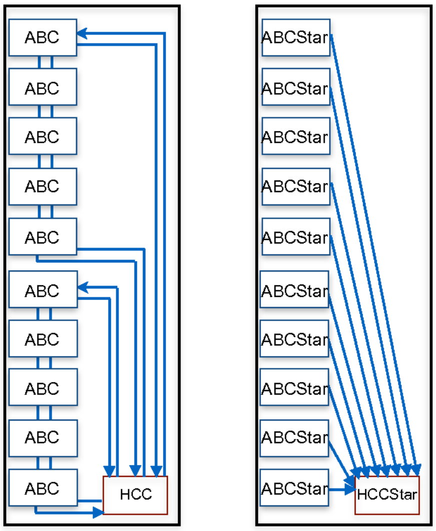

Figure 7.: ABC130 (left) and ABCStar (right) interface to the HCC chip. ABC130 uses daisy chain signal routing while the ABCStar uses the new design, where each ABC has a direct link to the HCC [17].

The analog components of the ABC130 and ABCStar are the same. In both cases, the chips have 256 readout channels with preamplifier-shapers, discriminators with individual threshold and trimming capabilities, a buffer, an event builder, and a cluster finder [17]. In every case, the channel's signal is amplified, shaped, and then discriminated to provide a binary output.

The HCCs are the interface ASIC between the stave or petal signals and the ABCs. They receive a bunch-crossing clock and control signals like the trigger and general commands from the off-detector electronics through the EoS [17]. These signals are processed and sent via the hybrid bus to the ABCs. The HCCs also receive the signals from the ABCs, build packets and transmit them via the stave/petal bus service to the EoS. The HCCStar had to be redesigned almost entirely to support the new readout architecture shown in Figure 7.

However, the hybrid requires one additional routing layer to maintain a safety factor of two on the bandwidth to support this new topology. In addition, the HCC requires a 640 Mbit down-link bandwidth back to the EoS card.

Hybrids are radiation-hard circuits consisting of four-layer copper on polyimide PCBs resulting in flexible circuitry with low mass. The total target thickness is 300 µm, and measurements have shown that 275 µm are a typical value for the thickness [55]. Due to the sensor geometries, there are 13 different endcap layouts and one unique barrel design. The principal function of the hybrids is to host the readout ASICs and provide the required services for them, including single power and ground lines and the connection of the external clock and control of the ABCs to the HCCs [56]. Two types of hybrids have been studied in this thesis in correspondence with the two versions of the front-end ASICs. A single hybrid can handle up to 11 ABCs, and thus, in the endcap, two hybrids are needed to read out a single strip segment in the R3-R5 modules.

The powerboard provides DC-DC conversion [57], from 11 to 1.5 V, for the front-end and the power for the on-detector electronics used for monitoring and control. It also provides the power for the sensor high voltage biasing. Moreover, it carries an Autonomous Monitor and Control (AMAC) ASIC [17], which measures temperature, voltages, currents, and control of low voltage, power states, and a high voltage switch.

All the components discussed are radiation tolerance and designed for mass production and low cost. Likewise, the designs ensure material reduction to minimize the effect on the tracking performance. Performance studies before and after irradiation of the different components can be found in [17], sections 6.2.3, 6.2.4. and in [51, 50].

Chapter 3

Silicon Detectors

Silicon (Si) is a semiconductor material that has been at the heart of the electronic industry and, in particular, the Integrated Circuit (IC) one since the second half of the 20th century. Silicon's success is based on its properties but more significantly on its abundance. Silicon is the second most abundant element on Earth, and its silicate minerals account for more than 90% of Earth's crust. The utilization of silicon for microelectronics has made the usage of silicon detectors more affordable. As a consequence, nowadays, silicon sensors are covering larger areas of the central tracking detector systems in the main LHC experiments.

Before discussing the silicon properties and its use for particle detectors, it is imperative to understand the different interaction mechanisms of particles with matter. Therefore, the following section briefly describes the main interaction mechanisms of interest for the energies encountered at the LHC experiments. Section 3.2 presents the most important properties of silicon that make it suitable for particle detection. Section 3.3 introduces key technological concepts that enable silicon usage as a particle sensing material and the physics of p-n junctions. The signal formation after the passage of a particle is discussed in Section 3.4, while the radiation effects of silicon are discussed in Section 3.5. Finally, Section 3.6 summarizes the main characteristics, design specifications, and working principle of strip sensors for tracking applications.

3.1. Interaction of Particles with Matter

The interaction mechanisms depend on the particle type and energy. The next sections describe the interaction of charged particles, followed by a short discussion on multiple scattering and finalizing with the interaction process of photons.

3.1.1. Interaction Mechanisms of Heavy Charge Particles

Heavy charged particles, referring to any particle heavier than an electron, interact predominantly via Coulomb interaction with the shell electrons of the material's atoms and can either produce ionization or excitation of the atoms in the medium. Bethe and Bloch [58, 59] were the first to investigate the energy loss of heavy charged particles. Their work gives the average energy lost per unit length for a heavy charged particle as [60]

$$-\left\langle \frac{\mathrm{d}E}{\mathrm{d}x} \right\rangle = Kz^2 \frac{Z}{A} \frac{1}{\beta^2} \left[\frac{1}{2} \ln \frac{2m_e c^2 \beta^2 \gamma^2 T_{max}}{I^2} - \beta^2 - \frac{\delta\left(\beta\gamma\right)}{2} \right] , \tag{1}$$

with:

$K = 4\pi r_e^2 m_e c^2 N_A \approx 0.307$ MeVcm^2/mol, with m_e and r_e being the rest mass and the classical radius of the electron

z, $\beta = v/c$ are the charge number and relative velocity of the projectile particle

Z, A are the atomic number and atomic mass number of the material

I is the mean excitation energy of the material

T_{max} is the maximum kinetic energy transfer to a free electron in a single collision

$\delta\left(\beta\gamma\right)$ is the density correction

Equation 1 is valid in the region where $0.1 \leq \beta\gamma \leq 1000$. For a given material, the particle energy loss is a function of its velocity alone.

The Bethe-Bloch equation describes how particles lose their energy until they reach the thermal energy and stop in the media. Therefore, it is also known as *stopping power*. It is common to normalize the stopping power to the density of the material and define the mass stopping power as $\mathrm{d}E/\mathrm{d}x$ in units of MeVg^{-1}cm^2. Figure 8 shows the mass stopping power of pions in silicon as a function of $\beta\gamma$.

The stopping power shows a broad minimum around $\beta\gamma \approx 3 - 3.5$, corresponding to $\beta \approx 0.95$. A particle with energy in this range is referred to as *Minimum Ionizing Particle* or MIP. If a detector system yields a measurable signal when a MIP transverses the material, it should respond to any other more ionizing particle.

Particle energy loss is a statistical process, and hence, it is subject to statistical fluctuations, which are described by a Landau-Vavilov distribution function [62, 63]

$$L(\lambda) = \frac{1}{\pi} \int_0^\infty e^{-t\ln t - \lambda t} \sin(\pi t)\, \mathrm{d}t \ , \tag{2}$$

The standard form in Equation 2 can be adjusted to the energy loss distribution, and the relation between the energy loss and λ is

$$\lambda = \frac{\Delta E - (\Delta E)_{\mathrm{m.p.v.}}}{\xi} \quad \text{with} \quad \xi = \frac{1}{2} K \frac{Z}{A} \frac{z^2}{\beta^2} \cdot d \ , \tag{3}$$

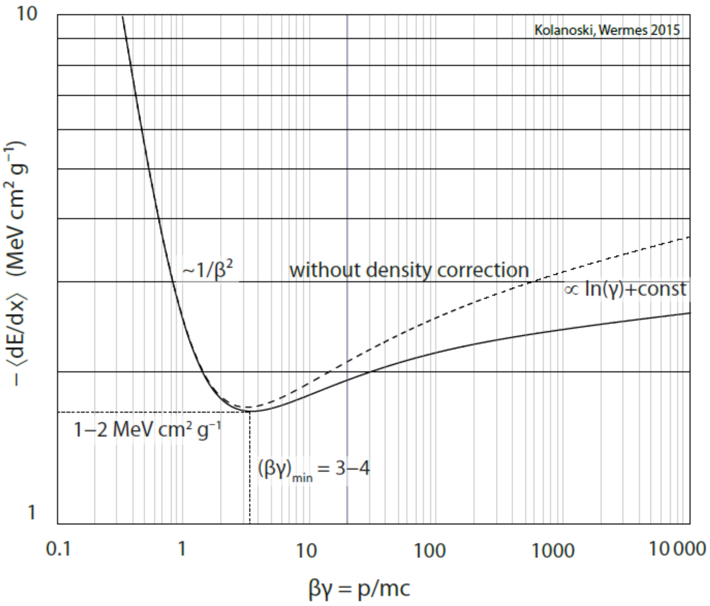

Figure 8.: Density weighted mean energy loss of charged pions in silicon as a function of $\beta\gamma = p/mc$ [61].

where d is the thickness of the medium and

$$(\Delta E)_{\text{m.p.v.}} = \xi \left[\ln \frac{2m_e c^2 \beta^2 \gamma^2}{I} + \ln \frac{\xi}{I} + j - \beta^2 - \delta(\beta\gamma) \right] \, , \tag{4}$$

stands for the most probable value of the total energy deposition, where the density correction $\delta(\beta\gamma)$ has been included [64] and the correction term $j = 0.2$ [60] is used. While $\mathrm{d}E/\mathrm{d}x$ is independent of the thickness, $(\Delta E)_{\text{m.p.v.}}/d$ depends of the material thickness via $\ln \xi$.

The distribution, shown in Figure 9, can be viewed as the convolution of a Gaussian and a Landau distribution given by the many ionization processes with small energy transfer and a long tail towards large energy losses. The long tail is associated with head-on collisions, which lead to δ electrons. Events with significant single-collision energy losses bias the mean energy loss, making it inadequate for characterizing energy loss in a detector. A better, more stable description is given by the most probable energy loss, which is noticeably smaller than the mean value given by Equation 1.

3.1.2. Interaction Mechanisms of Electrons

For light charged particles such as electrons, radiative losses cannot be neglected. Therefore, the total mean energy loss involves various interaction mechanisms. At low velocities, energy loss mainly results from inelastic collisions with the shell electrons, leading to excitation and ionization similar to heavy charged particles. For relativistic velocities, the mean energy loss is almost exclusively given by *bremsstrahlung*, which

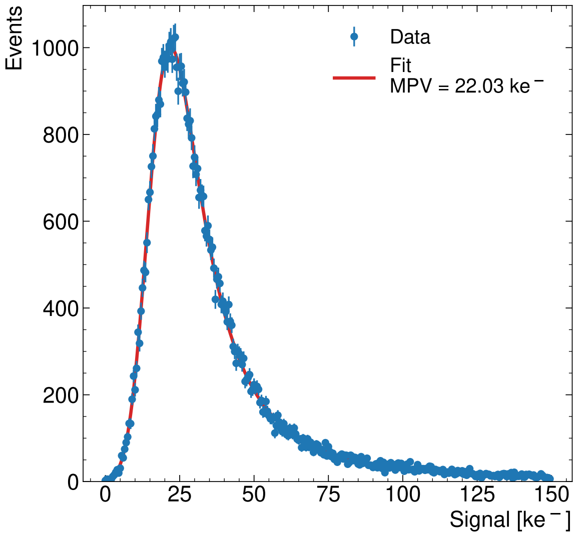

Figure 9.: Landau-Gaussian convoluted distribution for minimum ionizing particles in silicon measured in a charge collection measurement setup. The data is fitted using the `pylandau` package provided in [65].

takes place when a charged particle is accelerated in the electric field of the nucleus, and the emission of individual photons accounts for the total momentum change of the electron. The bremsstrahlung cross-section is proportional to Z^2/m^2, where Z^2 and m^2 are the atomic number of the medium and the mass of the projectile particle. Therefore, for energies below 100 GeV, bremsstrahlung is only significant for electrons and positrons [61]. The Z^2/m^2 dependence also implies that the predominant energy loss mechanism is ionization for β particles, whose energies are in the 0.5-2 MeV range. These particles are used for detector characterization, as will be shown in Section 6.5.

A third mechanism, the emission of Cherenkov radiation [66], becomes predominant when the particle's velocity is larger than the phase velocity of the light in the medium. Even though electromagnetic radiation is emitted, the particle does not emit Cherenkov light. In contrast, the emission results from the deexcitation of the dipoles created by the incident particle's electromagnetic field. As a result, the Cherenkov losses are much smaller than the ionization or bremsstrahlung and can be, in most cases, neglected. Hence, the total mean energy loss of light charged particles can be considered as follows:

$$\left(\frac{\mathrm{d}E}{\mathrm{d}x}\right)_{\textbf{total}} = \left(\frac{\mathrm{d}E}{\mathrm{d}x}\right)_{\textbf{ion.}} + \left(\frac{\mathrm{d}E}{\mathrm{d}x}\right)_{\textbf{brem.}} \quad . \tag{5}$$

The ionization term, given by Bethe-Bloch's equation, is different for electrons and positrons and differs from Equation 1 because of kinematics, spin, charge, and the indistinguishability of identical particles in quantum mechanics, which leads to a maximum energy transfer given by $m_e c^2(\gamma - 1)/2$. However, experimentally, it has been shown that the stopping power of electrons, positrons, and heavy charged particles does not differ greatly [60].

As stated, the radiative loss is proportional to the particle's energy, and the proportionality constant only depends on particle and media properties. Thus the radiative term in Equation 5 can be expressed in terms of the *radiation length* X_0 as

$$\left(\frac{\mathrm{d}E}{\mathrm{d}x}\right)_{\textbf{ion.}} = -\frac{E}{X_0}\ . \tag{6}$$

The radiation length is material-dependent, and it combines the proportionality constants of the bremsstrahlung energy loss. After an electron has traveled one X_0 inside the material, it would have radiated, on average, 63% of its energy. Values for different materials can be found in [67]. For silicon, the radiation length is $X_0 = 21.82\ \mathrm{gcm}^{-1}$. This value means that an electron with an energy greater than the critical energy [60] would radiate 63% of its energy after traversing 9.36 cm of silicon. The radiation length is used to characterize the electromagnetic showers, which encompass bremsstrahlung, pair production (see Section 3.1.4), and multiple Coulomb scattering, discussed in the next section.

3.1.3. Multiple Coulomb Scattering

Charged particles can also interact via inelastic collisions with the nuclei of the material. These collisions are governed by the Rutherford scattering cross-section [68], where small-angle deflections are favored. When a particle passes through a material, many small-angle, individually independent scattering processes described by the Rutherford formula occur. This process is known as multiple Coulomb scattering, resulting in a total scattering angle θ, as shown in Figure 10.

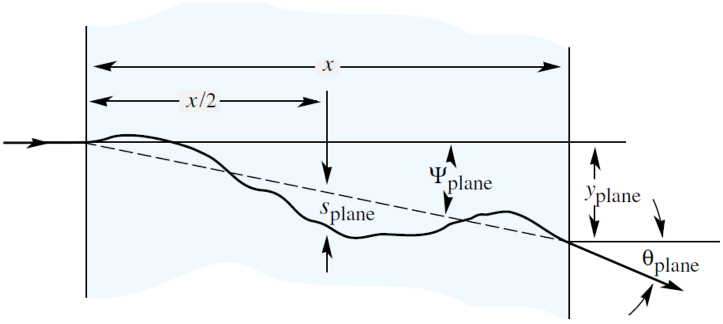

Figure 10.: Multiple Coulomb scattering of a charged particle in a material layer. The total scattering angle θ_{plane} is depicted [60].

The total scattering angle can be considered to follow a Gaussian distribution with mean value equal to zero, and the standard deviation given by [60]

$$\sigma_\theta = \frac{13.6\ MeV}{\beta c p} z \sqrt{\frac{x}{X_0}} \left(1 + 0.038 \ln \frac{x}{X_0}\right) \ , \tag{7}$$

where z, p, and β are the charge number, momentum, and relative velocity of the scattered particle, x the thickness, and X_0 the radiation length of the material, respectively. The dependence with the inverse of the momentum in Equation 7 makes clear that for low momentum tracks, multiple scattering effects are more significant. Therefore, the precision of tracking and momentum resolution measurements can be considerably affected if the impact of multiple scattering is not considered when designing a tracking system. Because the total scattering angle scales with the square root of the ratio between the material thickness and the radiation length, the detector layers should be kept as thin as possible to minimize the impact of multiple Coulomb scattering on the tracking layer.

3.1.4. Interaction Mechanisms of Photons

Photon interaction with matter differs considerably from charged particles, and it comprises three main processes which occur depending on the photon energy.

- **Photoelectric effect**: It is the dominant process for photons with energies in the lower keV range but above the binding energy of shell electrons. The incident photon completely transfers its energy onto an atom, which delivers back the absorbed energy by emitting an electron with kinetic energy equal to the difference between the photon's energy and the binding energy.

- **Compton effect**: The Compton effect is the scattering of a photon of a quasi-free shell electron. This condition is fulfilled when the photon's energy is well above the electron's binding energy. As a result, a fraction of the photon energy is transferred to the electron. The Compton effect takes place in an energy range of around 1 MeV. This energy range becomes larger as the material's atomic number decrease.

- **Pair production**: A photon is converted into an electron-positron pair in the Coulomb field of a charge. The photon energy must be at least twice as large as the electron mass, plus the recoil energy transferred to the field where the charges are produced. The process occurs mainly in the nucleus field where the recoil energy can be neglected, and the energy threshold can be set at $E_\gamma \approx 2m_ec^2$.

3.2. Silicon Properties

The conductivity of a material is defined as the inverse of its resistivity, which is a fundamental property of a material that measures how much it opposes the flow of an electric current. In terms of their conductivity, solid materials can be classified into three categories: conductors, semiconductors, and insulators. The conductivity of a solid is determined by its band structure. The large number of atoms in a periodic lattice of a crystalline material enables the formation of energy bands for the electrons, whose energies must be confined to one of the bands. The bands are available energy states arising from the solution of the Schroedinger equation for electrons in a periodic potential, according to Bloch's theorem [69]. Energy levels that are not solutions to the equation appear as energy "gaps". The lowermost band is called the valence band, and the uppermost conduction band. The size of the energy gap primarily determines the conductivity. Conductors do not have an energy gap, while insulators show energy gaps of several eV.

Semiconductors have bandgap energies ranging from a few hundred meV to a few eV. In semiconductors at $T = 0$ K, the valence band is fully occupied with electrons, and the conduction band is empty, making the conductivity of the material zero. At higher temperatures, thermal energy can excite an electron to the conduction band, leaving an empty state, known as a hole, in the valence band and increasing the material's conductivity. Holes are treated as positive particles with an effective mass greater than the electron's mass.

Silicon is a semiconductor with a bandgap energy of $E_g = 1.12$ eV [70] at room temperature. However, Si is an indirect semiconductor. Hence, further phonons are required to account for the misalignment in momentum between the valence band's maximum and the conduction band's minimum when energy is deposited. The average energy needed to excite an electron to the conduction band and create an electron-hole pair is $E_{Si} = 3.6$ eV [61].

When a particle passes through Si, it interacts with the medium, and if it deposits an amount of energy greater than E_{Si}, several electron-hole pairs are generated. The number of electron-hole pairs is proportional to the energy deposited. For example, a MIP would create $\sim 3.2 \cdot 10^4$ e-h pairs in 300 µm of Si, while at room temperature ($T = 300$K), the intrinsic amount of charged carriers in the same volume is $\sim 4.35 \cdot 10^8$ e-h pairs. Under these conditions, the signal can not be measured because the number of e-h pairs produced by the particle is indistinguishable from the thermally generated ones. As a result, the detection of the particle is not possible. To measure the e-h pairs created by the particle, the material needs to be depleted from the intrinsic charge carriers. In practice, particle detection in semiconductors is accomplished by using a p-n junction operated in reverse bias. The following section describes the main characteristics of a p-n junction and its application as a particle detector.

3.3. Silicon Sensors

3.3.1. Doping

The conductivity of semiconductors can be modified by changing the number of free carriers with the introduction of external atoms (a few parts per million or less) in the crystal lattice. The process of introducing foreign atoms is known as doping. When present in small concentrations, the impurity atoms occupy substitutional sites in the lattice by replacing one atom from the material. For example, in the case of silicon, which has four valence electrons and forms covalent bonds, conductivity is modified by doping the material with atoms from groups III and V.

Atoms from group V, like phosphorus, have five valence electrons; therefore, when used for doping, one extra electron does not form a covalent bond. The extra electron is loosely bound to the impurity site in the lattice, and only a small amount of energy is needed to lift it into the conduction band without a reciprocal hole in the conduction band. Under these conditions, there is an excess of free electrons (majority carriers) and a lack of holes (minority carriers) regarding the intrinsic material. The material is called *n-doped*, and the impurity atom is known as *donor*. Therefore, n-doped silicon's conductivity is determined by the electrons with a small contribution from the holes. Donor impurities introduce new levels in the forbidden gap close to the conduction band. Figure 11 shows different energy levels introduced in the silicon energy gap for different impurities. Deep donor levels are marked with a "D" and can act as generation-recombination centers, increasing the current in a reversed bias junction (see Section 3.3.2), also known as leakage current.

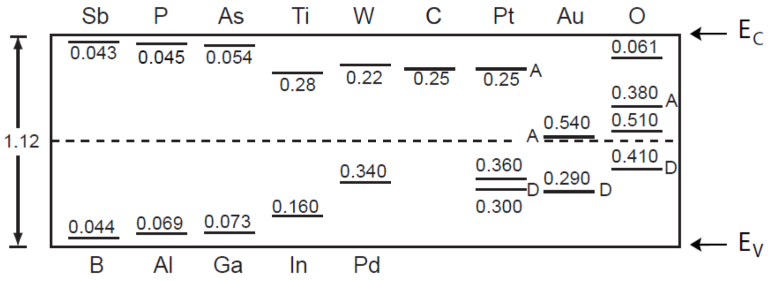

Figure 11.: Energy levels within the bandgap of silicon introduced by different impurity atoms. The numerical values are the ionization energies in eV of each impurity. Deep levels are marked with A for acceptors and D for donors [61].

The material has excess holes when impurities from group III of the periodic table, like boron, are used as dopants. In this case, one covalent bond is incomplete, leaving a vacancy equivalent to the hole left by an electron excited to the conduction band. Thus, the impurities called *acceptor* impurities produce new energy levels within the bandgap that are very close to the valence band, see Figure 11. Thermal excitation and the smaller energy difference between acceptor levels and the valence band ensure that electrons are constantly filling the vacancies created by the acceptors. Consequently, a significant fraction of the vacancies are occupied. These electrons come from other covalent bonds in the lattice, and hence, they leave holes behind in the valence band. Consequently, there will be approximately one extra hole for every acceptor atom making holes the majority of charge carriers. The holes dominate the material conductivity, and the material is known as *p-doped.*

3.3.2. P-N Junction Properties

A p-n junction is produced in the interface region between p-type and n-type materials, as shown in Figure 12. The concentration difference of majority charge carriers between the two materials creates a diffusion of carriers through the junction resulting in the recombination of electrons and holes. The diffusion of electrons and holes creates a negative space charge on the p-side and a positive space charge on the n-side of the junction. The accumulation of positive and negative charges builds an electrostatic field, which counteracts the diffusion. In equilibrium, the electrostatic field is sufficient to prevent further diffusion forming a *space charge region* (SCR) in the proximity of the junction where there are no free charge carriers. This space charge region is also known as *depletion region.*

The electrostatic potential of the junction, assuming an ideal abrupt transition region, can be obtained from the Poisson equation:

$$\frac{\mathrm{d}^2\phi}{\mathrm{d}x^2} = \frac{\rho(x)}{\varepsilon_{Si}\varepsilon_0} \quad \text{with} \quad \rho(x) = \begin{cases} -eN_A, & \text{for} \quad -x_p < x < 0, \\ eN_D, & \text{for} \quad 0 < x < x_n. \end{cases} \tag{8}$$

where N_D and N_A are the concentration of donors and acceptors, e is the unit charge, ε_{Si}, ε_0 are the dielectric constants of silicon and vacuum and x_p and x_n are the extension of the depletion zone in the p-doped and n-doped materials, respectively. Equation 8 leads to the electrostatic field given by:

$$E(x) = \begin{cases} -\dfrac{eN_A}{2\varepsilon_{Si}\varepsilon_0}(x+x_p)^2, & \text{for} \quad -x_p < x < 0, \\ \\ \dfrac{eN_D}{2\varepsilon_{Si}\varepsilon_0}(x-x_n)^2, & \text{for} \quad 0 < x < x_n. \end{cases} \tag{9}$$

The voltage drop over the depletion region, the built-in voltage V_{bi}, is derived from the potential difference between the p and n regions outside the SCR. Hence, V_{bi} is given by:

$$V_{bi} = \frac{e}{2\varepsilon_{Si}\varepsilon_0} x_p^2 \frac{N_A}{N_D}(N_A + N_D) \ , \tag{10}$$

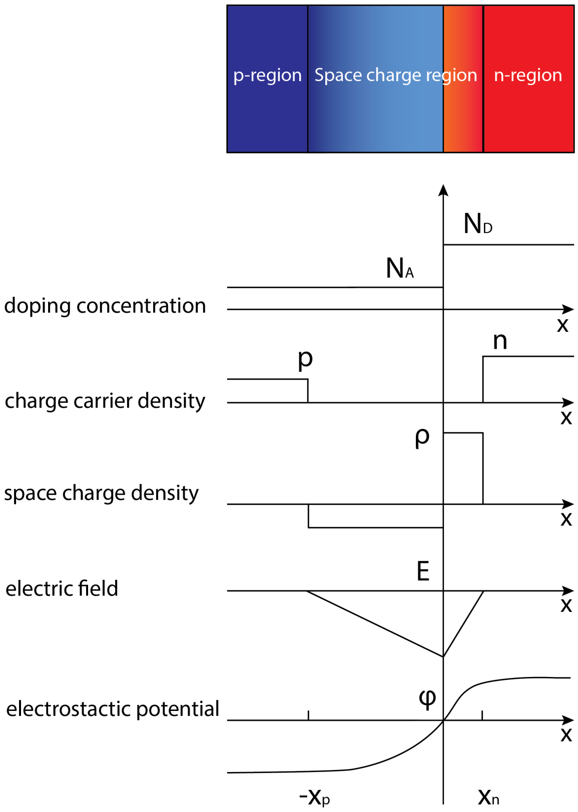

Figure 12.: Doping concentration, carrier and space charge density, electric field, and potential of an abrupt p-n junction.

To obtain the final result in Equation 10, the fact that the semiconductor is electrically neutral has been used. Therefore, the neutrality condition, $N_A x_p = N_D x_n$, holds. The extension of the depletion region is:

$$W = \sqrt{\frac{2\varepsilon_{Si}\varepsilon_0}{e} V_{bi} \left(\frac{1}{N_A} + \frac{1}{N_D} \right)} \ . \tag{11}$$

The space charge region extension is larger in the lightly doped part of the material, making the width of the depletion region approximately equal to the extension of the lightly doped part. Taking the effective doping concentration as $N_{\text{eff}} \simeq N_D$, Equation 11 takes the form:

$$W \approx \sqrt{\frac{2\varepsilon_{Si}\varepsilon_0}{e} V_{bi} \frac{1}{N_{\text{eff}}}} \ , \tag{12}$$

which can also be used in the case of p^+-n[1] junctions with $N_{\text{eff}} \simeq N_A$.

---

[1] p^+ refers to a heavily doped material with either acceptors or donors (n^+). The exact doping concentration required for p+ doping will vary depending on the bandgap of the material and the dopant used. In silicon, p^+ doping is typically achieved by doping with boron at a concentration of around $1{\times}10^{20} - 1 \times 10^{21}$ cm^{-3}.

The width of the depletion region can be changed by applying an external voltage to the terminals of the junction. If a positive voltage is applied to the n side with respect to the p side, the junction is reversely biased. In reverse bias, the electrostatic potential difference between the p and n-side increases, and the diffusion current through the junction decreases. In addition, the width of the depletion region also increases with the increase of the applied reverse bias. The same analysis that led to equation 12 is also valid if the total applied potential is $V_{bi} + V_{bias}$. Hence, applying reverse bias, the depletion width is

$$W \approx \sqrt{\frac{2\varepsilon_{Si}\varepsilon_0}{eN_{\mathrm{eff}}}(V_{bi} + V_{bias})} \; . \tag{13}$$

Particle detectors employing semiconductors are operated in reverse bias. This operation mode allows for larger detection volumes, which provide larger signals.

3.3.3. Capacitance and Current-Voltage Characteristics

In a p-n junction, the depletion region behaves as an insulator material, and the n and p sides as conductors. Consequently, the p-n junction can be modeled as a parallel-plate capacitor with capacitance:

$$C = \varepsilon_{Si}\varepsilon_0 \frac{A}{W} \; , \tag{14}$$

where A is the area of the diode and W is the width of the depleted zone. For a fully depleted 300 µm thick planar silicon diode, the capacitance is of the order of $C \approx 35 \cdot A$ pF/cm^2 [61]. Combining equations 13 and 14 one obtains

$$\frac{1}{C^2} = \frac{W^2}{(A\varepsilon_{Si}\varepsilon_0)^2} = \frac{2(V_{bi} + V_{bias})}{eN_{\mathrm{eff}}\varepsilon_{Si}\varepsilon_0 A^2} \; . \tag{15}$$

Equation 15 describes a linear relationship between $1/C^2$ and V_{bias} from which it is possible to determine the *full depletion voltage*, i.e. the voltage needed to deplete the entire volume of the sensor. After full depletion, the $1/C^2$ behavior as a function of the voltage is constant, as shown in Figure 13a, since the depletion region cannot extend beyond the thickness of the sensor. The slope of the line allows us to estimate N_{eff} (the lighter dopant concentration of a one-sided junction) directly using Equation 15. In addition, the wafer resistivity [71], defined as $\rho \approx (e\mu N_{\mathrm{eff}})^{-1}$ [61] can be estimated by combining Equations 13 and 15.

A diode in reverse bias conducts a small current at temperatures above absolute zero. This current originates from thermal excitation. However, there is a reverse bias voltage, known as *breakdown voltage*, for which the junction becomes highly conductive. The reverse current rises sharply, increasing the risk of permanently

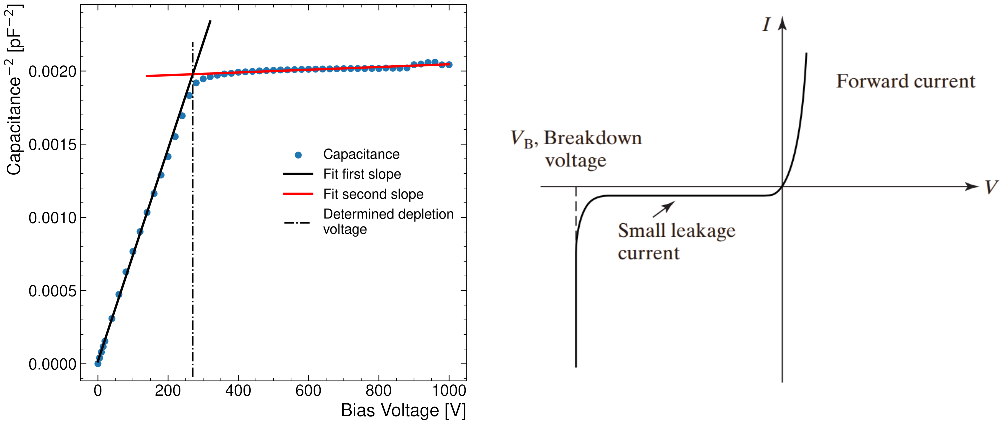

(a) **(b)**

Figure 13.: (a) Inverse of the square capacitance as a function of the applied voltage for a test diode included in the ATLAS12 sensor submission [72]. The data show the linear behavior described by Equation 15 until full depletion, after which the capacitance stays constant. The common double linear fit employed to find the bias voltage is also shown (b) Typical current-voltage characteristic of a p-n junction (adapted from [73]).

damaging the junction. Figure 13b shows the current-voltage characteristic of a diode where the breakdown voltage is observed. Junction breakdown occurs when the electric field reaches a maximum, which depends on the doping concentration and is of the order of 10^5 V/cm. At this critical electric field value, charge carriers have enough energy to produce more e-h pairs (charge multiplication) in collisions with the lattice. Another mechanism, known as tunneling or Zener breakdown [70], occurs in abrupt, heavily doped junctions but is not predominant for the typical doping concentrations used in particle detectors.

In principle, operation at voltages greater than the *breakdown voltage* is possible, as in Zener diodes. However, in detector applications, this regime does not allow the measurement of the particle's signal. Under reverse bias, the measured current is called *leakage current* and has volume and surface contributions. For detectors, the main contribution arises from the depletion volume due to the thermal generation of e-h pairs. The current largely depends on the number of impurities that create levels within the bandgap that acts as generation/recombination centers. The leakage current depends on the volume of the depleted region, the intrinsic doping concentration, and the lifetime of the charge carrier generation. It can be parameterized as

$$I_L \propto T^2 \exp\left(-\frac{E_a}{2k_bT}\right) , \tag{16}$$

where T is the temperature of the detector and E_a the activation energy or effective energy [61], which also depends on the temperature but has a best-fit value of

$E_a = 1.21$ eV [74]. In silicon detectors, the leakage current at room temperature is of the order of nA/cm^2 [75]. The leakage current increases proportionally with the radiation dose, and after high doses, it reaches values of µA/cm^2. Therefore, measurements of the leakage current offer a powerful method for characterizing the effects of irradiation. The surface contribution to the leakage current comes mostly from the manufacture and handling of the detectors.

3.4. Signal Formation

As discussed, when a particle passes through silicon, it ionizes atoms in the material, creating electron-hole pairs. The charge carrier movement towards the electrodes induces a measurable signal on them. The carrier's motion follows the Boltzmann transport equation [61] and considers the diffusion and the drift motions when an external electric field is applied across the material.

Under the effects of an external electric field, the overall velocity of electrons and holes results from the acceleration given by the electric field $\vec{E}$ and the scattering of the carriers with phonons and lattice defects. The solution to the Boltzmann transport equation, following Drude's solution [61] for the stationary case, takes the form:

$$\vec{v}_D = \frac{q\tau}{m_{\text{eff}}}\vec{E} = \mu\vec{E} \ , \tag{17}$$

where q is the unit charge, m_{eff} is the effective mass, and τ is the relaxation time, which is the average time until the next momentum change and combines several lattice effects. In silicon, τ is in the picosecond range and depends strongly on temperature [61] The parameter $\mu = \frac{q\tau}{m_{\text{eff}}}$ is known as mobility. The mobility of electrons and holes differs due to their effective mass. In silicon, at room temperature, the electron mobility is about three times larger than the hole mobility [70].

The drift velocity increases directly proportional to the applied electric field for values much lower than 10 kV/cm^2 [61] for a given temperature and doping concentration. The carriers have more energy at higher field values than the lattice, and scattering with optical phonons occurs. As a result, the charge carriers lose energy, and the mobility decreases with the increase of the $\vec{E}$. Thus, for a given temperature and doping concentration, the drift velocity saturates for high electric fields, as shown in Figure 14 for silicon and germanium. At room temperature, the drift velocity saturation is in the order of 10^7cm/s.

The spatial variation of the charge carrier concentration within the semiconductor and the thermal energy lead to the movement of electrons and holes from high to low concentration regions. This movement is called carrier diffusion. If we consider that all electron-hole pairs are created in a single point, this number can be described by a

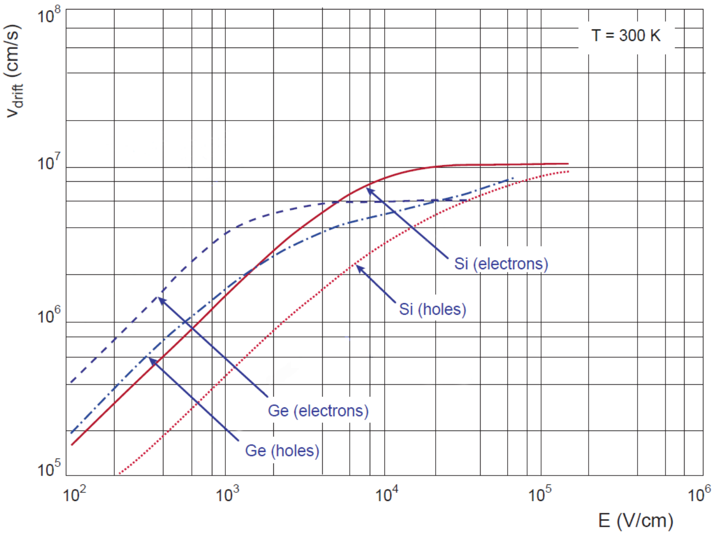

Figure 14.: Electron and hole drift velocity in silicon as a function of the applied electric field at room temperature (adapted from [61]).

δ-distributed concentration, the diffusion will broaden this distribution as a function of time. The cross-section of this distribution is given by [76]

$$\sigma = \sqrt{Dt} \ ,$$

where D is the diffusion coefficient, which is linked to the mobility by the Einstein relation [76]:

$$D = \frac{kT}{e}\mu \ , \tag{18}$$

In a silicon detector, the movement of the charge carriers is a combination of the drift and the diffusion motions. Drift motion follows the electric field lines and diffusion spreads out the charge carrier cloud.

3.4.1. Charge Induction and Shockley-Ramo Theorem

The deposited energy due to ionization inside the depleted silicon material generates charge carriers, which, neglecting the effect of diffusion, drift across the sensor following the electric field lines produced by the externally applied voltage. The movement of the carriers induces a current on the collection electrodes. This current stops when the charge carriers recombine at the electrodes, and its integral is the collected charge.

The general approach to calculate the induced current and, therefore, the collected charge on the electrodes uses the concepts of weighting field, weighting potential, and the Shockley-Ramo Theorem [77, 78]. The theorem states that the induced current

i_s and the accumulated charge Q on the electrode are:

$$i_s = q\vec{v}\vec{E}_w \quad \text{and} \quad Q = -q\Delta\phi_w \ , \tag{19}$$

where $\vec{E}_w$ and ϕ_w are the electrode system's weighting field and weighting potential, and $\vec{v}$ is the velocity of the charge. Hence, the induced charge on the electrode is independent of the trajectory of the carrier towards the electrode. Only the beginning and end positions determine the collected charge. The weighting potential and field for a given electrode are calculated by removing all charges from the system under study and setting all electrodes to ground except for the electrode of interest, which is set to 1 V. With the previous potential configuration, ϕ_w and $\vec{E}_w$ are obtained as solutions of the Laplace equation $\Delta\phi_w = -\boldsymbol{\nabla} \cdot \vec{E}_w = 0$. The weighting potential is dimensionless, and the weighting field has the dimension 1/length. It should be emphasized that the weighting field depends only on the geometrical electrode configuration and, thus, differs from the electric potential.

The detector signal is the integral over time of the induced current within the integration time of the amplifier. If the integration time is shorter than the total drift time or carriers get trapped (see Section 3.5.1), not the entire signal is measured.

In strip and pixels sensors, charges traveling close to the readout electrode will induce a higher signal for a given displacement Δx than carriers traveling the same Δx but further from the readout electrode. Consequently, the carriers drifting toward the sensing electrode contribute more to the detector signal. As a result, in a strip detector with n-type implants, the measured signal is dominated by electrons, whereas for p-type electrodes, the main contribution to the signal comes from holes. Hence, when a loss of charge is expected, for example, after irradiation, the position of the electric field regarding the weighting field should fulfill two requirements. First, that after the change of the effective doping concentration, the highest electric field should be positioned at the readout electrode, meaning that the electric field should be high where the weighting field is high. Second, the carrier type with the largest lifetime and drift distance should be collected at the readout electrode. The previous recommendations constitute the physics reasons supporting the decision of the LHC experiments to use n-in-p sensors to upgrade their tracking systems in preparation for the HL-LHC instead of the traditionally used p-in-n sensors.

3.5. Radiation Damage

Silicon sensors are operated in the closest regions to the interaction point in particle physics experiments, where the charged and neutral particle flux reaches exceptionally high intensities. The interaction of this large number of particles leads to a degradation of the material properties over time, which is known as radiation damage. Radiation damage in silicon can be divided into two types: damage to the silicon crystal, better known as bulk damage, and surface damage, which can also refer to damage of boundaries and interfaces.

Bulk damage predominantly results from collisions with the lattice nuclei that do not lead to ionization. These types of interactions are known as Non-Ionizing-Energy-Loss (NIEL). The NIEL can be normalized to the damage caused by neutrons with an energy of 1 MeV.

The primary mechanism producing bulk damage when hadrons and high energetic leptons traverse silicon material is the production of atom displacements. A direct collision with the atomic nuclei of the crystal can knock off an atom from its lattice site. The displaced atoms leave vacancies in the crystal and occupy positions outside the lattice, known as interstitials. Figure 15 shows some of these primary defects. Vacancies and interstitials are unstable and can migrate through the crystal, forming a wide range of defects or changing their configuration.

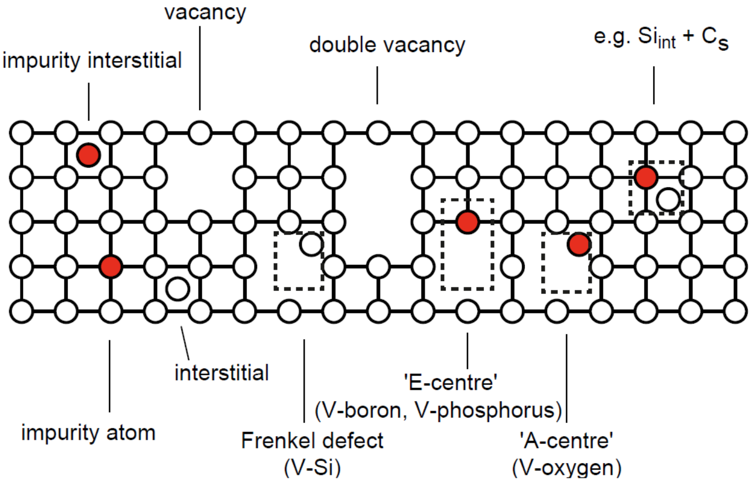

Figure 15.: Examples of primary defects produced by atom displacements in silicon. Red circles are impurity atoms. Complex defects are marked with the dashed rectangles while V, Si_{int} and C_s denote vacancies, silicon interstitial, and a carbon atom substituting silicon in a lattice site [61].

Furthermore, recombination is possible, leading to the annihilation of the defects and no remaining damage. These processes depend strongly on temperature [79, 80]; therefore, their behavior can be engineered with heat treatment. The heat treatment of materials to alter their physical properties is called annealing. The annealing process can be beneficial or unfavorable. Consequently, the temperature and time of the process need to be precisely controlled to obtain the desired effect of the material properties. The electrical properties of the defects that do not annihilate are responsible for the further macroscopic deterioration of the detector material.

Charged particles can produce atom displacement via Coulomb scattering off nuclei, while neutrons produce displacement via elastic and inelastic scattering. To displace an atom with a probability higher than 50%, the transferred energy to the nuclei has to be greater than the displacement threshold energy E_d, which for silicon is 25 eV [81]. The type of defects produced by the radiation depends on the type of particle and its energy and can be largely categorized into single defects and clusters, which are a dense accumulation of single defects usually caused by heavy particles. It is difficult to find a measurable relationship between the changes induced by radiation in the materials and the irradiation dose because of the many factors involved in producing atom displacements. The NIEL scaling hypothesis establishes a relationship between the radiation fluence and the damage caused by it in the material. This hypothesis states that any radiation damage in the material linearly scales with the NIEL and only depends on the number of primary defects, i.e., the energy loss in atom displacements, irrespective of their initial spatial and energy distribution. The non-ionizing energy loss is defined as [61]:

$$\left.\frac{\mathrm{d}E}{\mathrm{d}x}\right|_{NIEL}(E) = \frac{N_A}{A} D(E) \ , \tag{20}$$

where N_A is the Avogadro number, A the atomic mass of the material in g/mol and $D(E)$ is the damage function, which depends on the particle type and its energy and also considers the process cross sections:

$$D(E) = \sum_i \sigma_i(E) \int_{E_d}^{E_R^{max}} f_i(E, E_R) P(E_R) \mathrm{d}E_R \ , \tag{21}$$

E and E_R are the kinetic energies of the impinging particle and the recoil atom, and i goes over all the possible displacement processes with cross sections σ_i. The function $f_i(E, E_R)$ gives the probability of producing a Primary Knock-on Atom (PKA) with recoil energy E_R when a particle of energy E undergoes the interaction process i. The term $P(E_R)$ is called the partition function and yields the fraction of the recoil energy spent in generating atom displacements.

The damage functions allow us to describe the damage produced by different particle types at different energies as the ratio κ of $D_x(E)$ for particle x at an energy E to the 1 MeV neutrons damage $D_n(E = 1 \text{ MeV})$. The latter is called NIEL scaling and the ratio κ, called hardness or damage factors, is defined as [82]:

$$\kappa = \frac{\int_{E_{min}}^{E_{max}} D_x(E) \phi(E) \mathrm{d}E}{D_n(1 \text{ MeV}) \int_{E_{min}}^{E_{max}} \phi(E) \mathrm{d}E} \ , \tag{22}$$

with $\phi(E)$ is the energy spectrum of the impinging particles.

The damage of 1 MeV neutron has been set to $D_n(1\text{ MeV})$=95 MeV mb [83] to ensure independence from the energy spectrum binning used to calculate D_n. The equivalent 1 MeV neutron equivalent fluence is then calculated as:

$$\Phi_{eq} = \kappa\Phi = \kappa \int_{E_{min}}^{E_{max}} \phi(E)\mathrm{d}E \ . \tag{23}$$

The NIEL scaling hypothesis correctly describes certain aspects of radiation damage effects in silicon detectors [84] but presents some deficiencies. For example, it does not represent well the changes in the effective space charge concentration and the trap introduction rate [61].

3.5.1. Consequences of Bulk Damage in Silicon Detectors

Bulk damage creates new energy levels within the bandgap. The position of these levels within the energy gap defines their electrical behavior. Three different classes group the level position within the bandgap (a) acceptor and donor centers, which change the effective doping concentration, (b) generation-recombination centers, which increase the leakage current and (c) trapping centers, which decrease the signal amplitude.

Donor centers are very close to the conduction band, while the acceptor levels are close to the valence band. Moreover, levels in the vicinity of the middle of the bandgap produce generation-recombination centers, whereas intermediate levels create trapping centers. The Shockley-Read-Hall statistics give the quantitative description of the consequences of the different defects [61].

The change in the effective doping concentration is an effect of the deactivation of donor and acceptor atoms with irradiation. Donors are likely to be deactivated by the capture of mobile vacancies, E-centers in Figure 15, while acceptors are annihilated when interstitial oxygen atoms capture them. Likewise, completely new donor and acceptor levels can be created. The change in doping concentration is proportional to the radiation fluence and can lead to a shift in its sign. The process is known as type inversion, and it means that initial n-type silicon will eventually become p-type, as it is shown in Figure 16a.

The change in the effective doping concentration leads to a change in the depletion voltage, as shown in Figure 16a. After type inversion, the depletion voltage increases. In some cases, it can surpass the experiment's power budget and the high voltage tolerance of the sensor or power supply, forcing it to operate under depleted detectors with the corresponding reduction of the output signal.

However, the key issue is that for sensors, which were originally n-type, the junction is formed at the sensor backside. For position-sensitive sensors, having the junction on the opposite direction to the segmented electrodes implies that the electric field

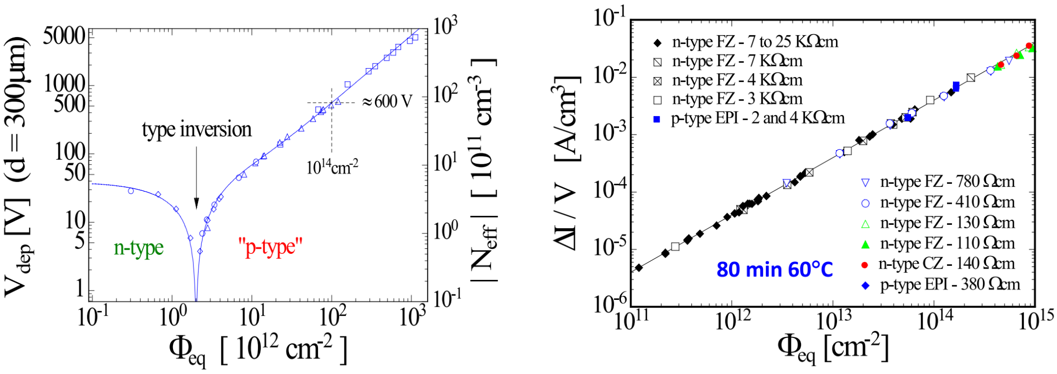

(a) (b)

Figure 16.: (a) Effective doping concentration of the silicon bulk and depletion voltage and (b) radiation-induced change of leakage current as a function of the 1 MeV neutron equivalent fluence [84].

at the electrodes becomes weak, which reduces the charge induction and, therefore, the position sensitivity is lost. High resistivity silicon gets inverted around fluences of $\phi_{eq} \approx 10^{12-13}\ n_{eq}/\text{cm}^2$. At the HL-LHC, the detectors will be exposed to these fluences before their planned lifetime, making type-inversion an important factor to consider in the detector design. The change to p-type bulk sensors for the ATLAS ITk detector (see Section 2.6) eliminates the effect of type inversion after irradiation, thus also offers the advantage of depletion from the pixel/strip implant side (front-to-back) through the entire sensor lifetime and the collection of electrons instead of holes.

The defect levels neighboring the middle of the bandgap reduce the size of the gap and, therefore, ease the generation of electron-hole pairs. In contrast, electron-hole pairs can also recombine in these levels. The macroscopic property affected is the leakage current. The leakage current increases proportionally with the radiation fluence, as shown in Figure 16b for different sensor resistivities and fabrication processes after the standard annealing time of 80 minutes at 60°C. Because the leakage current also depends on the temperature, all the current values in Figure 16b are normalized to the current measured at 20°C. The relation can be written as [85]

$$I_L = \alpha \phi_{eq} V \ , \tag{24}$$

where V is the volume under the electrode, ϕ_{eq} is the equivalent fluence, and α is the proportionality coefficient, called damage rate. The damage rate is independent of the silicon material, the manufacturing process, and the particle type of the radiation [82] for a given annealing temperature and time. The damage rate dependence with time for different annealing temperatures is shown in Figure 17a. For all temperatures, α decreases with annealing time [86], meaning that annealing reduces the sensor leakage current. The increased leakage current heats up the detector, which again increases the leakage current due to the corresponding increased temperature. This process creates a chain reaction that can lead to a "thermal runaway" which can destroy the detector. Additionally, leakage current causes an increment of the electronic noise at the input of the readout channels; see Section 3.6.2.

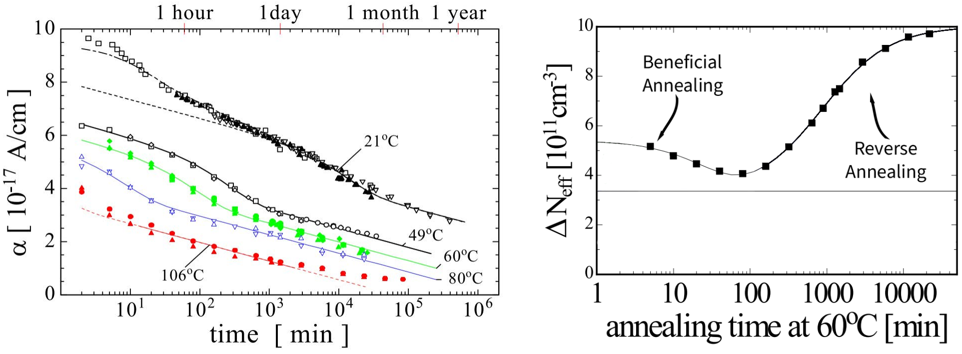

(a) **(b)**

Figure 17.: (a) Damage rate α as a function of the annealing time for different temperatures [84] (b) Change in effective doping concentration with annealing time at 60°C (adapted from [84]).

The doping concentration changes with annealing and therefore, this evolution process can be stopped, decelerated, or accelerated when the sensor is kept at low or high temperatures. For example, it has been shown [80] that keeping a detector at a temperature of 60°C for about 80 mins has a beneficial effect, so-called "beneficial annealing", due to the decrease of acceptor-like states, making the effective space charge more positive (more n-type) after irradiation. In contrast, keeping the temperature for longer times has the opposite effect, called "reverse annealing". The change of effective doping concentration at 60°C as a function of time is shown in Figure 17b, where the beneficial and reverse annealing are marked.

Defects produce trapping centers, leading to a decrease in charge collection in the detector. Charge carriers can get trapped in these defect levels when they drift toward the electrodes. If they stay trapped longer than the collection time, the charge is not integrated, and the measured signal decreases. To characterize the effect, an effective trapping time τ_{eff}, different for electrons and holes, is used with the assumption that the charge loss only depends on the drift time inside the sensor. The lost charge as a function of the drift time t can be calculated as $Q(t) = Q_0 \exp\left(-\frac{t}{\tau_{\text{eff}}}\right)$ [84]. The effective trapping time is inversely proportional to the particle fluence, and the dependence has been empirically determined as:

$$\frac{1}{\tau_{\text{eff}}} = \frac{1}{\tau_{\text{eff},0}} + \beta\phi_{eq} \ , \tag{25}$$

where the proportionality factor β is the effective trapping damage constant, and

$\tau_{\text{eff},0}$ is the effective carrier lifetime before irradiation [84]. The signal loss can be overcome by applying over-depletion[2] voltages, reducing the drift time and trapping probability. The trapping constant also depends on the annealing time the sensor has experienced. Previous research has established that the effective trapping constant for holes increases, while the electrons one decreases for 40 hours of annealing time at a temperature of 60°C [87].

3.6. Silicon Strip Sensors

A single p-n junction can act as a particle detector and is the most straightforward detector geometry. However, the most common structures for tracking applications are pixel [88] and strip sensors. Pixel detectors offer position measurements in two dimensions and many readout channels, but fabrication is costly. Strip detectors provide only one spatial coordinate but are easier to manufacture and have fewer channels. The tracking systems of HEP experiments use a combination of both, placing pixel layers close to the interaction point where high position resolution for vertex reconstruction and a larger channel density due to a higher occupancy are required. Because the detectors studied in this thesis are all strip detectors, this section describes the geometrical structure of strip sensors, biasing, and signal extraction methods.

The basic structure of a strip sensor is shown in Figure 18. The sensor consists of a silicon substrate (bulk) whose electrode is segmented into strip implants with a pitch of tens of micrometers. The strip implants act as electrodes and are produced through ion implantation. The doping concentrations of the bulk and the implants have different doping types. Therefore, a p-n junction is created at each strip implant-bulk interface, as shown in Figure 18a.

A SiO_2 layer passivates sensitive structures against dust and humidity and protects against mechanical damage, and in the specific case of the design shown in Figure 18a, it decouples the DC signals from the sensing volume. In the back side of the bulk, a thin layer, dark blue in Figure 18a, of the same dopant as the bulk but with higher doping concentration is implanted and coupled with a thin aluminum layer, depicted in gray in Figure 18a, to form an ohmic contact. This implant layer in the backplane isolates the back of the sensor from the electric field inside the bulk. To provide isolation in the lateral edges, the so-called *guard rings*, shown in Figure 18b, are used.

The guard ring is an implant using the same dopant as the strip that decouples the current generated outside the sensitive area from the one generated inside. It also shapes the field by eliminating high-field regions that could cause avalanche breakdown. In addition, to prevent channel formation [90] between the strip implants,

---

[2] Over-depletion means to operate at a voltage higher than the full depletion, increasing the electric field strenght within the sensor bulk

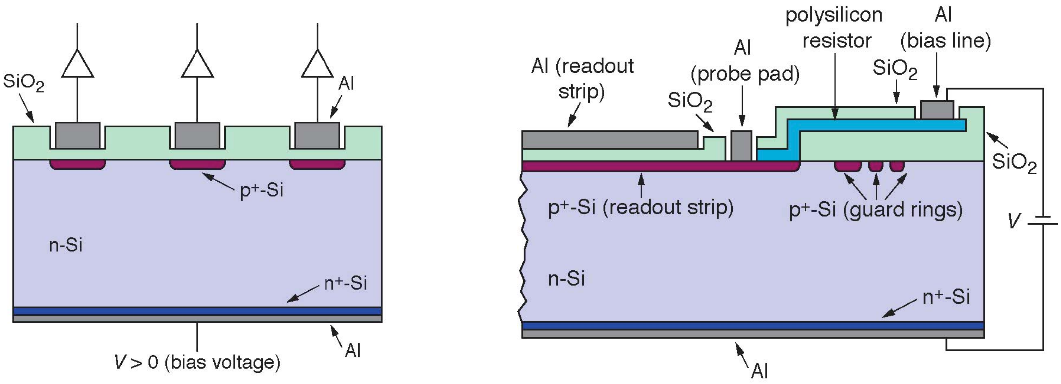

(a) (b)

Figure 18.: Orthogonal (a) and cut-through (b) schematics of an AC-coupled p^+-in-n silicon strip detector [89].

channel stopper structures like p-stop [91] or p-spray [92] are employed.

An aluminum metallization can be placed directly on the implants (DC-coupled) or a thin passivation layer, creating a capacitive coupling (AC-coupled) between the implant and the aluminum strip. The former enables good ohmic contact between the implants and the electronics. AC-coupled detectors can prevent the leakage current, a DC signal, from flowing through the readout electronics. This configuration is preferable in particle detectors, but it comes with increased fabrication costs, the necessity of a separate way of biasing the AC coupled strips, and the risk of pinholes [93]. There are different methods for biasing the sensor, but the most widely used are polysilicon resistors, depicted in Figure 18a, or the punch-through mechanism. Biasing the sensor using resistors is the most straightforward method and is more radiation hard.

3.6.1. Working Principle of Silicon Strip Sensors for Tracking

Charged particles traversing the silicon bulk lose energy via ionization, Sections 3.1.1 and 3.1.2, and part of this energy is employed to create electron-hole pairs. The carriers immediately separate in the applied electric field and drift toward the electrodes. Their movement induces a charge in the electrodes, whose magnitude and shape are determined by the number of charge carriers, their velocity, and the electrode configuration, see Section 3.4.1.

For a typical 200-300 μm of thickness and velocities of around 50 μm/ns [61], the drift time, and therefore, the signal pulse duration from the detector becomes 4-6 ns, which is fairly short. Considering that the most probable energy loss by a MIP in a 300 μm thick silicon sensor is 84 keV and the energy to generate an electron-hole pair is 3.65 eV, the total induced charge is 3.7 fC.

The segmentation of the electrodes into strips and pixels allows us to accurately measure the position through which the particle passed in the detector. The position resolution depends on the electrode geometry and the type of readout used. When the sensor is read out with a binary readout (1=hit, 0=no hit), as for the current ATLAS ID and the future ITk, the position resolution is given by the electrode pitch p. For perpendicular incidence and single hit response, the variance of the true position perpendicular, here x, to the strip is [61]

$$\begin{aligned} \sigma_x^2 &= \frac{1}{p}\int_{-p/2}^{p/2} x^2 \mathrm{d}x = \frac{p^2}{12} \\ \sigma_x &= \frac{p}{\sqrt{12}}. \end{aligned} \tag{26}$$

It is important to note that strip detectors only have a good resolution in the coordinate perpendicular to the strips. The same mathematical arguments leading to Equation 26 can be applied to the coordinate along the strip length. However, typical strip lengths are in the centimeter range, making the resolution in this direction extremely poor to the point that it can be considered that there is no resolution in this direction. For example, an ATLAS ITk Short Strip sensor has a strip length of 2.41 cm, and the binary resolution is approximately 0.7 cm. The latter is considerably larger than the 22 µm resolution of the same sensor in the perpendicular direction to the strips, where the pitch is 75.5 µm.

The so-called stereo layers improve the resolution in the coordinate along the strips. The concept is to add a second detector layer, which is slightly rotated. In the ITk, these angles are 56 mrad in the barrel and 40 mrad in the endcaps; see Section 2.7.

When pseudo-analog readout is used, the charge induced on each electrode allows computing the entrance point by weighted averaging the signals generated on neighbor strips. Thus, the resolution perpendicular to the strips for analog readouts depends on the signal-to-noise ratio, pitch, and signal fraction induced on each strip.

Irrespective of the readout type, the readout chain, also known as front-end electronics, comprises components shown in Figure 19. Because the detector signals are relatively small, they are fed to the (pre)amplifier before further processing. As both noise and signal are amplified, the noise contributions before the amplifier need to be minimized. The amplified signals are passed to the pulse shaper, whose primary function is to improve the signal-to-noise ratio by filtering noise signals with high and low pass filters. After the pulse shaper, the signal is digitized. An analog-to-digital (ADC) converter translates the analog signal into a binary word saved for data analysis. In addition, some readout schemes include a discriminator stage after the pulse shaper, which allows one to compare the signal to a given threshold and decide if a particle or noise caused the signal.

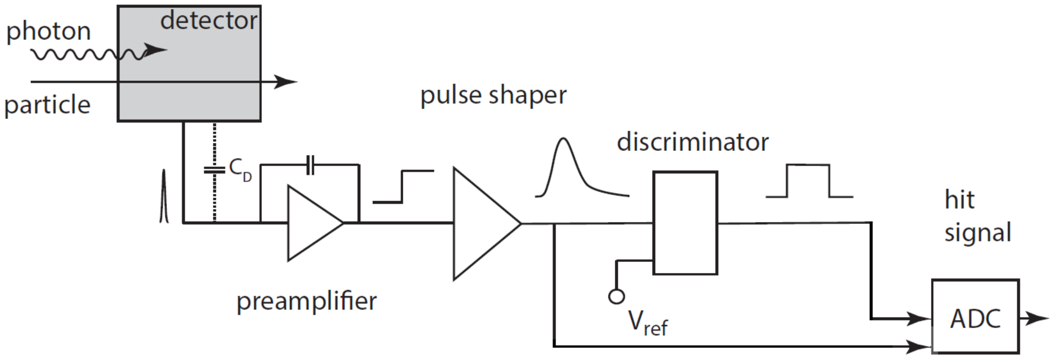

Figure 19.: Common components included in a front-end readout chain (adapted from [61].

3.6.2. Noise Sources and Detector Operation

Regardless of the type of measurement required, the primary goal of a detector system is to maximize the signal-to-noise ratio, which indicates, for a given event, the ratio between the signal (theoretically noise-free) and the root mean square noise. The noise is expressed in equivalent noise charge (ENC), representing the number of electrons contributing to the noise. The detector signal can only be increased by increasing the sensor thickness; therefore, the noise must be minimized.

The contribution of the different noise sources is system-dependent. However, they can be classified into three physical sources: thermal, shot, and $1/f$ noise [76]. Thermal noise originates from fluctuations in the velocity of the charge carriers. In contrast, shot noise is a statistical fluctuation in the number of charge carriers emitted through a potential barrier like the bandgap of silicon. The $1/f$ noise is not completely described by theory and is present in many other systems [61]. However, it identifies all noise contributions whose frequency spectrum follows the $1/f^{\alpha}$ law, with $\alpha = 0.5, ..., 2, 3$, and in electronics systems, it is attributed to the trapping and de-trapping of charge carriers.

In silicon detectors, the elements contributing to the noise are the total detector capacitance C_d, the sensor leakage current I_L, and the parallel and series resistances R_P, R_S. The total ENC noise at the input of the amplifier is given by [93]:

$$ENC = \sqrt{ENC^2_{C_d} + ENC^2_{I_L} + ENC^2_{R_P} + ENC^2_{R_S}}\ . \tag{27}$$

The noise from the total detector capacitance scales linearly and is the largest contribution to the total system noise. Because the total detector capacitance depends on the sensor geometry, shorter and thinner strips are desired. The latter is also why pixel detectors exhibit lower noise levels than strip detectors. The ENC_{C_d} is [93]:

$$ENC_{C_d} = a + b \cdot C_d, \tag{28}$$

with a and b being parameters dependent on the amplifier. The leakage current is a source of shot noise, and its contribution is quantified as [93]:

$$ENC_{I_L} = \frac{e}{2}\sqrt{\frac{I_L t_p}{q}}, \tag{29}$$

where e is the Euler constant, q is the unit charge and t_p the peaking time of the shaper. The leakage current increases after irradiation, see Section 3.5.1 and hence its contribution to the noise becomes larger, which emphasizes the argument of operating the detector at low temperatures.

The noise from the resistors constitutes a source of thermal noise. The resistances parallel to the amplifier are the inter-strip and the bias resistances. The noise is expressed as [93]:

$$ENC_{R_P} = \frac{e}{q}\sqrt{\frac{k_B T t_p}{2R_P}}. \tag{30}$$

Here, k_B is the Boltzmann constant, and T is the operating temperature. From Equation 30 is clear that the sensor design must ensure high inter-strip and bias resistance to minimize this source of noise. Finally, the series resistance contribution is obtained from [93]:

$$ENC_{R_S} = C_d \frac{e}{q}\sqrt{\frac{k_B T R_S}{6t_p}}. \tag{31}$$

The dependency with C_d reinforces the earlier statement that minimizing the total detector capacitance leads to low noise levels. In addition, the series resistance noise contribution is proportional to $\sqrt{R_S}$. Thus, it is important to minimize the series resistances.

Chapter 4

Beam Tests at the DESY-II Accelerator

Beam tests allow the evaluation of particle detector characteristics, such as tracking resolution and hit reconstruction efficiency, which are impossible to assess in laboratory tests. In addition, performing beam tests provides an opportunity to measure the performance of detector prototypes in actual experimental conditions. Operation and testing include synchronization with the accelerator and integration into other data acquisition (DAQ) systems. Thus, beam tests are crucial for every detector R&D effort.

As a part of the prototyping phase of the ITk Strip Detector for the Phase-II upgrade of the ATLAS Inner Tracker, eight beam test campaigns have taken place at the DESY-II Test Beam Facility since 2018. The main objectives of these campaigns were to assess the performance of different strip detector modules before and after irradiation, thereby demonstrating the ITk Strip's operability throughout the HL-LHC's lifetime. The results obtained in those campaigns and presented in this thesis were crucial for the ITk Strip collaboration to successfully pass several project reviews, such as the ITk Strip module Final Design Review, the ITk Strip ABCStar, and the barrel module Production Readiness Reviews.

4.1. The DESY-II Test Beam Facility

The DESY-II Test Beam Facility [94] provides electron/positron beams in the GeV range. The electron and positron beams for the beam test facility are produced via a double-conversion process from the DESY-II electron beam. First, bremsstrahlung photons are obtained by inserting a carbon fiber target into the accelerator orbit. Next, the generated photons travel along the extraction beam pipe and impact a secondary Cu or Al target. In the target, photons are converted via pair-production to electrons and positrons. A dipole magnet allows the selection of the particle type and its momentum by changing the polarity and strength of the field. With the described process, the achievable momentum of the particles ranges between 1-6 GeV/c [94].

The DESY-II accelerator's primary purpose is to serve as an injector for the PETRA-III storage ring. As a result, the beam from the accelerator has a complex time structure and operation, which dictates the availability of particles for the beam test facility. Beam test particles only reach the experimental halls when the energy of the DESY-II beam is higher than the selected momentum for the beam test. Therefore, the beam rate depends on the chosen particle momentum, as shown in Figure 20 for two experimental halls.

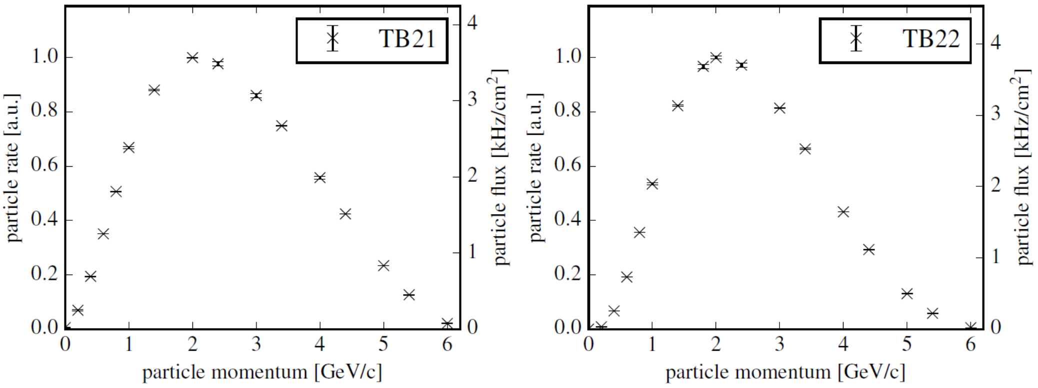

Figure 20.: Particle rate available for the test beam as a function of the selected momentum for beamlines 21 and 22 [94].

The plots show that the maximum particle flux, around 4 kHz/cm^{-2}, is obtained for a particle with a momentum of 2 GeV/c^2. High particle momentum is desired at beam tests to reduce the impact of multiple scattering on the tracking resolution. However, high rates allow for more efficient use of the beam time, reducing costs and providing room for a more comprehensive set of tests. Therefore, a compromise on the particle momentum is required during beam test operation to maintain a reasonable rate.

The three experimental areas have a beamline, environmental monitoring instrumentation, and various moving stages. A hut in the experimental area houses the remote control of user instrumentation installed. Each area includes one EUDET-type pixel Telescope [95], which provides tracking of the beam test particles. Figure 21 shows the interior of area 22. The beam telescope, beam collimation, and telescope alignment systems are highlighted.

4.2. Beam Telescopes

Beam test activities commonly measure the detector intrinsic resolution, tracking efficiency, and noise behavior. These measurements require an external and unbiased reference tracking system for comparison. A tracking system providing reference tracks at beam tests is commonly known as a beam telescope. Beam telescopes use

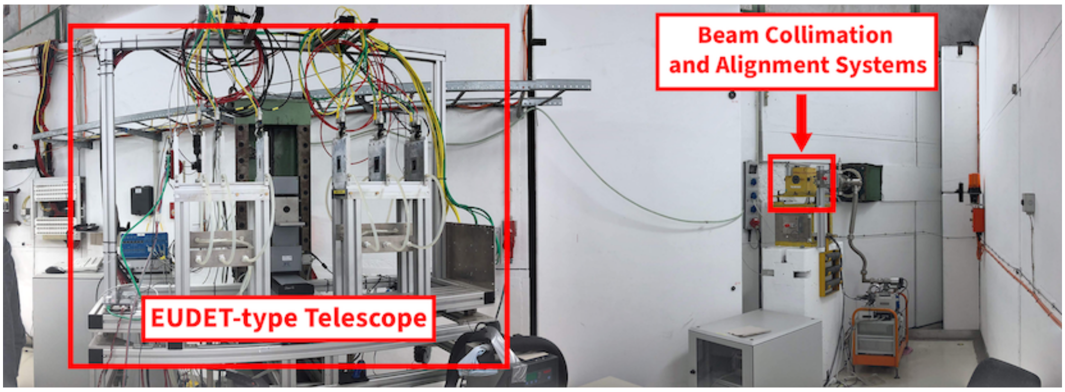

Figure 21.: Interior of the beam test area 22 at the DESY-II Test Beam Facility. The EUDET-type Telescope, the beam collimation, and the alignment systems are highlighted.

several pixel or strip detector planes with a spatial resolution of a few micrometers and well-known detection performance.

The beam telescope infrastructure includes the detector mechanical support, power, and cooling systems. It also comprises the trigger and data acquisition (TDAQ) systems. The telescope planes are usually divided into the upstream and downstream arms, depending on their placement with respect to the beam direction. Upstream refers to the planes mounted before the Device Under Test (DUT), while downstream refers to the ones mounted behind the DUT along the beam direction.

The most critical parameter of beam telescopes is the resolution of the reconstructed tracks at the position of the DUT. This resolution, also known as pointing resolution, directly affects the quality of the reconstructed tracks and hence, needs to be known precisely. The pointing resolution depends on the intrinsic resolution of the telescope detector planes, the amount of material the particles have to go through, the beam energy, and the number of measured points per track, which equals the number of telescope planes. Because the track positions are interpolated, the positioning of the telescope planes, i.e., its geometry, influences the track pointing resolution. It has been shown that to reduce the uncertainty due to the interpolation of the track position, the DUT needs to be placed as close as possible to its two adjacent telescope planes [95].

4.2.1. EUDET-type telescopes at DESY

At the DESY test beam facility, one EUDET-type beam telescope [96] is provided per experimental area. The EUDET telescope, shown in Figure 21, consists of six-pixel detector planes equipped with Mimosa26 (M26) Monolithic Active Pixel Sensors (MAPS), produced in a 350 nm CMOS process [97]. The sensors have an array of 1152 × 576 pixels with a pixel size of $18.4 \times 18.4\ \mu\text{m}^2$. This pixel arrangement covers an area of 21.1 × 10.6 mm^2. The sensors are thinned down to a thickness of 50 µm [95] to reduce the impact of multiple Coulomb scattering.

The detector readout uses a rolling-shutter mechanism with a total integration time of 115.2 µs [95]. The telescope planes are mounted in aluminum jigs with an opening for the beam, and the sensors are protected by 25 µm thick Kapton foil. The jigs are mounted on rails, which permit the movement of the individual planes. The sensor temperature is kept at 18 °C using a chiller with water as coolant.

Two sets of plastic scintillators provide triggering with light guides and Hamamatsu photomultiplier tubes. The scintillators are located before the first and behind the last M26 plane. Each set gives a total acceptance area of about 20×10 mm^2. Therefore, a fourfold coincidence of the scintillators' signal indicates that a particle traversed the entire telescope and is the most commonly used triggering scheme. When a coincidence is detected, a trigger logic unit (TLU) generates and distributes the trigger signal to the telescope planes and the rest of the detectors in the experiment.

The TLU also distributes the global clock and a global time reset. In addition, it generates and records the trigger identification number (trigger ID) and the trigger timestamp. The TLU can also handle different trigger veto conditions, like busy signals. A busy signal is generated when one of the detectors participating in the experiment is being read out. During the readout time, the detector issues a busy signal and does not accept any further triggers until the reading process is finished and the signal is pulled down. This process is known as *handshaking* and is controlled by the TLU. The EUDET-type telescope uses this simple scheme to veto triggers during the long integration time of the M26 detectors.

The telescope planes are read out by a data acquisition system based on National Instruments electronics [95]. Data corresponding to two shutter frames of the M26 readout are stored when the trigger signal is received. The associated trigger ID is recorded and stamped to the data for offline synchronization with other detectors involved in the tests. Only the trigger ID is recorded, meaning all signals detected in the M26 pixel plane during the 230.4 µs interval are associated with the same trigger. The integration time of an ATAS ITk module is 25 ns [17], which is about four orders of magnitude shorter than the corresponding telescope time. The latter creates hit identification ambiguities that are resolved using a time reference plane with the same integration time as the DUT.

The TLU and the DAQ systems are controlled by EUDAQ2 [98], providing global control and data streams to all detectors. EUDAQ2 is beam test specific and offers easy integration with user-specific DAQ systems, like the ATLAS ITk Strip prototyping DAQ, called ITSDAQ [51]. EUDAQ2 also provides online monitoring functionalities and generates binary files with the data streams collected from all the detectors involved in the test beam.

4.3. ATLAS ITk Strip Beam Test Setup

The ATLAS ITk Strip irradiation and test beam group has conducted eight different test beam campaigns at the DESY-II Test Beam Facility since 2018. The setup used through the campaigns differs only in the tested DUTs and in the EUDET telescope geometry. In addition, for testing irradiated detector modules, different cooling solutions have been utilized. Figure 22 shows the basic setup, which comprises the EUDET-type telescope, the time reference plane (timing plane), and the device under test. As mentioned, the DUT is placed between the two arms of the beam telescope, and the distance from its two adjacent planes is kept as short as possible. The timing plane, a pixel sensor read out by an FE-I4 ASIC [99] using the USBPix [100] test bench, is placed after the last M26 plane to minimize the impact on the telescope tracking resolution.

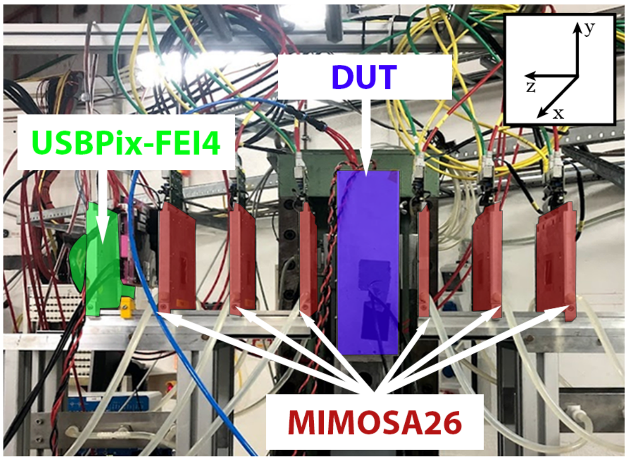

Figure 22.: ATLAS ITk Strip beam test setup. The EUDET telescope Mimosa26 planes are highlighted in red, whereas the DUT box is depicted in blue. For this setup, the FE-I4 pixel plane [99] with the USBPix [100] readout was employed as a timing plane.

4.4. Data-Taking

The data-taking period is usually set to two weeks, during which the work is distributed in shifts to maximize the beam time. Shifters supervise the experiment at all times, ensuring that all devices taking part in data taking are working as expected, that triggers are issued and recorded, and that the integrity and quality of the data are recorded.

Data quality is monitored using the Online Monitor from EUDAQ2. The Online Monitor visualizes data measured by each detector plane and the space and time correlations between data measured in different planes. Individual detector planes are monitored by checking their signal response, fired channels, the number of triggers received, and the trigger rate. The correlation plots allow for inspecting whether the data are synchronized in space and time, serving as the first measurement of the data integrity. Figure 23 shows a screenshot of the Online Monitor where the time correlation plot for the second Mimosa26 plane, the DUT, identified as ABC 35 from a beam test campaign in 2019 is observed. Similar plots are found for all the other planes, indicating that the triggers are correctly distributed through all the detectors in the setup.

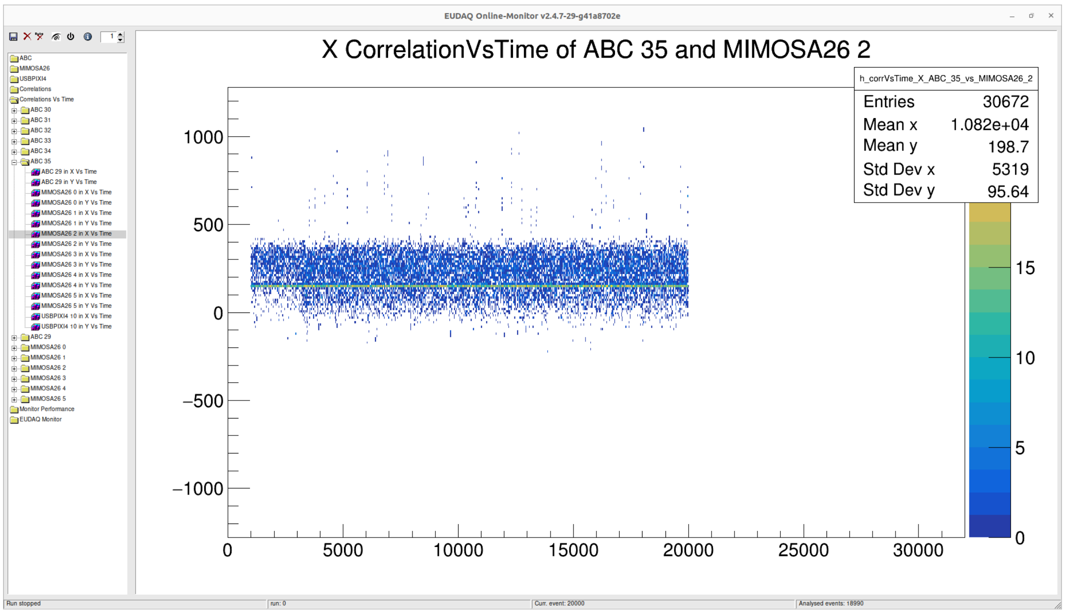

Figure 23.: Screenshot showing a time correlation between the second Mimosa26 plane and the DUT (ABC 35) in the Online Monitor from EUDAQ2. The visible straight line indicates good synchronization between the two planes.

Every change in the setup, i.e., geometry, currents, voltages, and temperatures, are logged during a shift. Furthermore, any incident that can compromise the data quality, like unstable beam conditions, faulty devices, or DAQ problems, is reported in the log. In addition, the data get flagged for further investigation.

The data are mostly taken as a part of different types of scans. For example, in the case of the ATLAS ITk Strip modules, most of the data are recorded during the so-called threshold scans at different positions of the modules. In addition, scans with different beam incidence angles, bias voltages, and a combination of them are also performed.

4.5. Beam Test Reconstruction and Analysis

Data analysis consists of two general steps. The first one is called data reconstruction and involves identifying detector hits from the raw data, the alignment of all the detector planes in the setup, and the fitting (reconstruction) of tracks. The identified hits and reconstructed tracks are used in the second step, which analyzes the detector performance.

4.5.1. Data Reconstruction with the Corryvreckan framework

The beam test data reconstruction is accomplished using the Corryvreckan [101] reconstruction software. Regardless of which software is employed, the reconstruction generally encompasses identifying noisy channels in the detector planes, cluster finding, the alignment of the detector planes, and the fitting of the telescope reference tracks. What follows describes the reconstruction chain in Corryvreckan.

Corryvreckan is highly modular and has been explicitly developed for beam tests. Therefore, it combines the reconstruction and analysis in a single software package. A typical reconstruction chain in Corryvreckan, employed for the reconstruction and analysis of the ATLAS ITk beam tests, is shown in Figure 24.

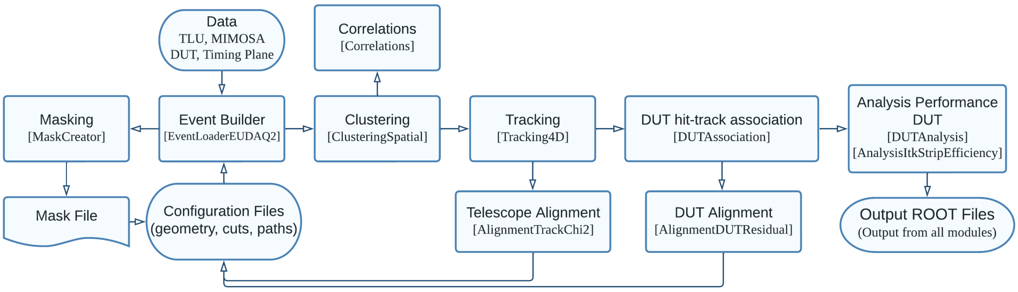

Figure 24.: Example of a reconstruction chain using the Corryvreckan framework. The main processes and the corresponding Corryvreckan modules are labeled. The modular approach of the framework allows high flexibility during reconstruction, including the possibility of reconstructing data from several different DUTs.

4.5.2. Event Definition

The first step of the data reconstruction process is the event definition, performed by the `EventLoaderEUDAQ2` module. When the coincidence between the scintillator signals is detected, the TLU distributes a trigger signal with a precise timestamp to all the detectors in the data taking. As mentioned earlier, the Mimosa26 sensors and the ATLAS ITk modules stamp the trigger ID to the data, but no timestamp is recorded. Consequently, an event is built by first matching all the data with the same trigger ID and centering the time of the event around the trigger timestamp. Therefore, the slowest device in the readout chain, the Mimosa26 pixel plane in the ITk setup, gives the time of one event.

The integration time of the Mimosas26 is considerable because of the rolling shutter readout. Hence, the time of an event covers the time in which the Mimosa26 hits could have been recorded. A hit can be registered in the triggered or the following readout cycle.

4.5.3. Clustering

The clustering algorithm only uses spatial information because the timestamps of individual pixel/strip hits are not recorded in the Mimosas26, the timing plane, and the ATLAS ITk modules. The Corryvreckan module employed is the `ClusteringSpatial`. This module combines direct neighbors to form a cluster and assigns a timestamp to the cluster, which is equal to the TLU trigger timestamp corresponding to the pixels/strips in the cluster. The Mimosa26, the Timing plane and the ATLAS ITk modules use a binary readout. Therefore, no deposited charge information is available. Hence, the cluster center's coordinates are calculated as the arithmetic mean of all the pixels/strips in the cluster. Figure 25 shows an example of the cluster size distribution and a cluster hitmap for one of the Mimosa26 detectors. A large average cluster size value is found for all the planes and originates in the considerable amount of charge collected via diffusion from the non-depleted volume in the sensors [102]. The distributions for the other Mimosa26 planes are comparable during all the beam test campaigns and agree with previous studies [102, 103].

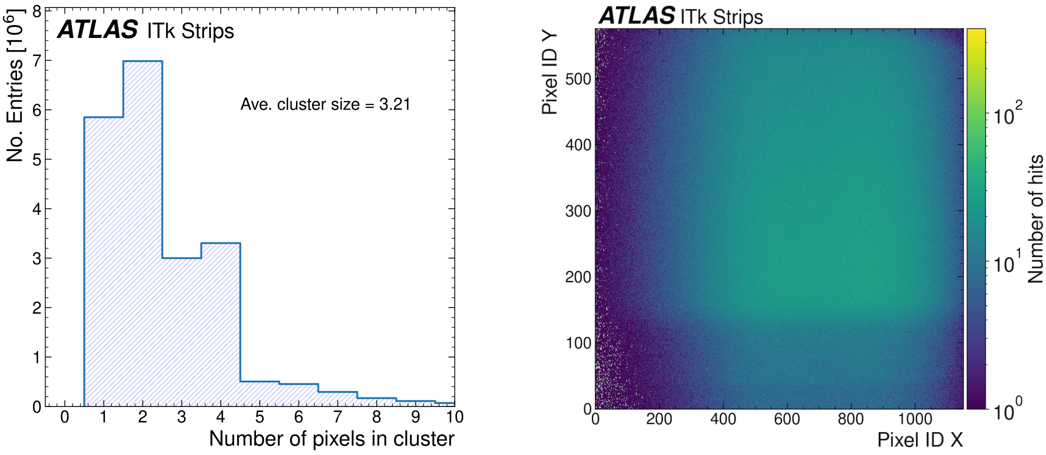

(a) **(b)**

Figure 25.: Cluster size (a) and cluster hitmap (b) of a Mimosa26 detector plane from the DURANTA EUDET telescope at the DESY beam test. From (a), it is clear that the average cluster size is larger than one. The regions in (b) where there are no cluster hits are due to not having a correct alignment of the beam and the telescope, i.e., part of the beam is not passing through the active pixel matrix.

4.5.4. Masking of Noisy Channels

To reduce the probability of reconstructing fake tracks, noisy/hot pixels are removed from the data by applying the so-called mask. The `MaskCreator` module in Corryvreckan stores the coordinates of noisy pixels and generates a mask. This mask contains a list of all the noisy pixels, and the other modules use it in the reconstruction chain to ignore the hot pixels. A simple frequency cut algorithm is utilized to define a pixel as noisy. If a pixel fires more than the average number of hits on the sensor times a defined frequency cut, the pixel is considered noisy and masked. In the analysis presented in Chapter 5, the chosen frequency cut is 100. The masking effect is visible in a correlation plot as shown in Figure 26. A correlation plot between two detector planes shows the difference in position or pixel/strip ID between the hits on a detector plane taken as a reference and any other plane. In a perfectly aligned setup, the correlation should follow a straight line with a slope equal to one and an intercept equal to zero because the tracks are parallel, considering no magnetic field and assuming negligible scattering. If the detector plane positions are displaced relative to each other, the intercept of the straight line corresponds to the physical offset in each direction.

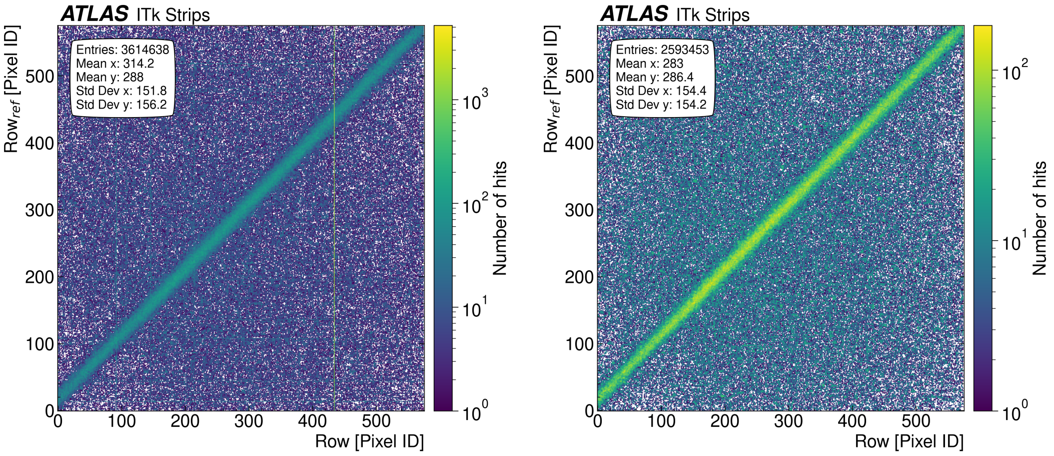

(a) **(b)**

Figure 26.: Row-Row correlation between the first (taken as reference) and the third Mimosa26 planes at the DESY beam test (a) before applying the noisy pixel mask and (b) after applying the noisy pixel mask.

Figure 26a shows the row correlation between the third and first (reference) Mimosa26 sensors before applying the hot pixel mask, while Figure 26b shows the correlation between the same planes after removing the noisy pixels. For example, in Figure 26a, it is straightforward to observe a very hot pixel in row 434 in the third Mimosa26 and row 518 of the reference plane and several others in both sensors. On the other hand, in Figure 26b, no hot pixels are visible, making the correlation between the two planes more pronounced. The latter is highly important for the prealignmet and alignment of the detectors involved in the beam test. In addition, it is evident that the total number of entries, see the color bar, has also decreased considerably, reducing the computing time during the reconstruction. The `Correlations` module is used in Corryvreckan to obtain the correlation plots.

In the case of the ATLAS ITk DUTs, the masking of noisy channels is usually done in extreme cases where noisy strips overshadow the correlations, making it difficult to align the detector. For example, noisy strips are masked when the DUTs are irradiated to extremely high fluences expected to be delivered during the HL-LHC lifetime. However, the procedure is the same as for the Mimosa26 sensors. It is important to emphasize that for the ITk modules, a noisy channel/strip can result from a faulty strip or a readout channel in the front-end electronics. Nonetheless, the observed effect is the same, and the terms noisy channel or noisy strip are used equivalently.

4.5.5. Tracking

A *track* is a mathematical object that describes the trajectory of a particle in space, and tracking is the procedure through which this trajectory is found in a given experimental setup. Tracks are reconstructed based on the detector hits. At the beam tests, track reconstruction only uses the reference telescope hits, which allows studying the properties of the DUT without biasing the analysis. Two procedures are included in the track reconstruction, finding and fitting. Both procedures are performed by the `Tracking4D` module of Corryvreckan.

Track finding, also known as pattern recognition, combines clusters from the telescope planes. A collection of clusters is called track candidates. The procedure, schematically shown in Figure 27, works by finding all the combinations of clusters in the first and second telescope planes and connecting them with a straight line. The lines are extrapolated to the next detector plane. Next, clusters found within the search window defined by the cuts, centered in the extrapolated line, and belonging to the same event, are added to the collection. The line is then fitted again. The process is repeated for the other telescope planes.

The track fitting step is performed by fitting a given track model to the cluster positions using a minimization of the track model χ^2. There are two main track models in Corryvreckan, the straight-line and the General Broken Lines (GBL) models [104, 105].

The straight-line model is simple and suitable when reconstructing tracks from high-energy heavy charged particles, like at the CERN Super Proton Synchrotron beam test facility. In contrast, the GBL is the appropriate track model when multiple Coulomb scattering is expected, like at the DESY test beam facility, where tracks

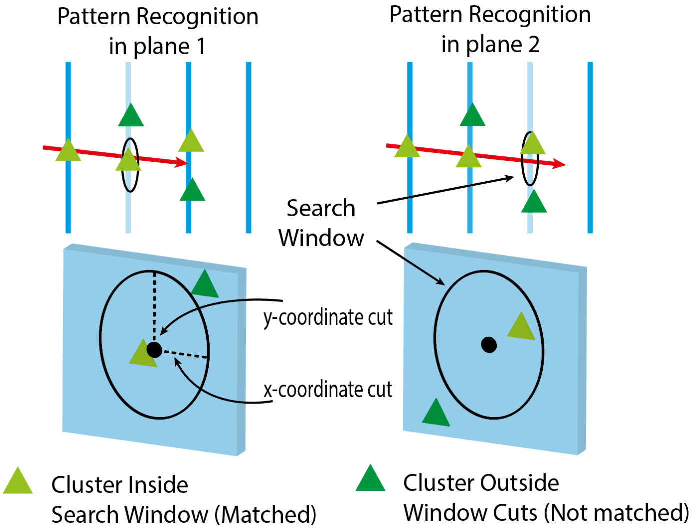

Figure 27.: Schematic of the pattern recognition algorithm implemented in Corryvreckan for selecting track candidates. The process is only depicted for two consecutive Mimosa26 sensors but is repeated for the rest of the telescope planes.

from light particles like electrons and positrons are reconstructed. The GBL model accounts for multiple Coulomb scattering by allowing a kink angle at each detector plane involved in the fitting or a passive material along the particle's trajectory. A linear extrapolation is done between two consecutive detector planes. The track reconstruction models are depicted in Figure 28.

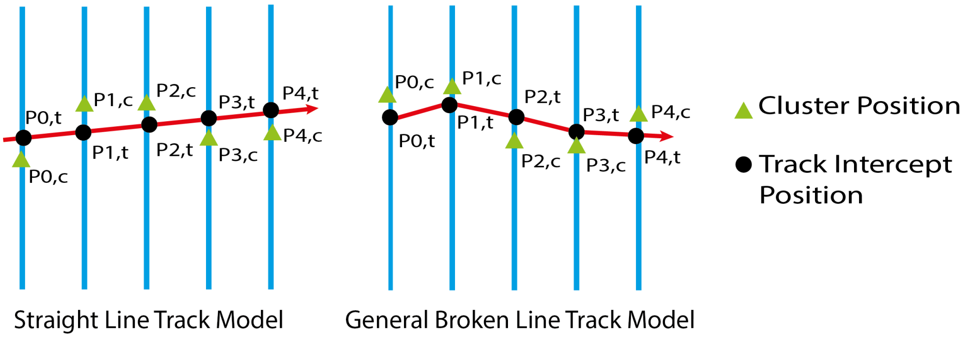

Figure 28.: Schematic representation of the straight line and general broken lines track models. The kinks produced by the particle scattering in the GBL sketch are exaggerated for visualization purposes.

At the beam tests at DESY, electrons and positrons with a maximum momentum of 6 GeV are used, and the impact of multiple Coulomb scattering can be considerable. In this scenario, the selection of the straight-line model would reduce the number of good-quality tracks, taking a toll on the overall track resolution at the DUT position and the precision of the performance analysis. Therefore, the GBL model is suitable for beam tests at DESY. Consequently, it has been used for all the analyses discussed in Chapter 5.

4.5.6. Track Selection and Track Quality

As indicated, a cluster is added to a track candidate if found within the event's given time and inside an ellipse defined by two spatial cuts. The spatial cuts are selected based on the intrinsic resolution of the telescope planes and the width of the correlation plots. Examples of correlation plots for the X and Y-coordinates are shown in Figure 29 for the second plane of the telescope.

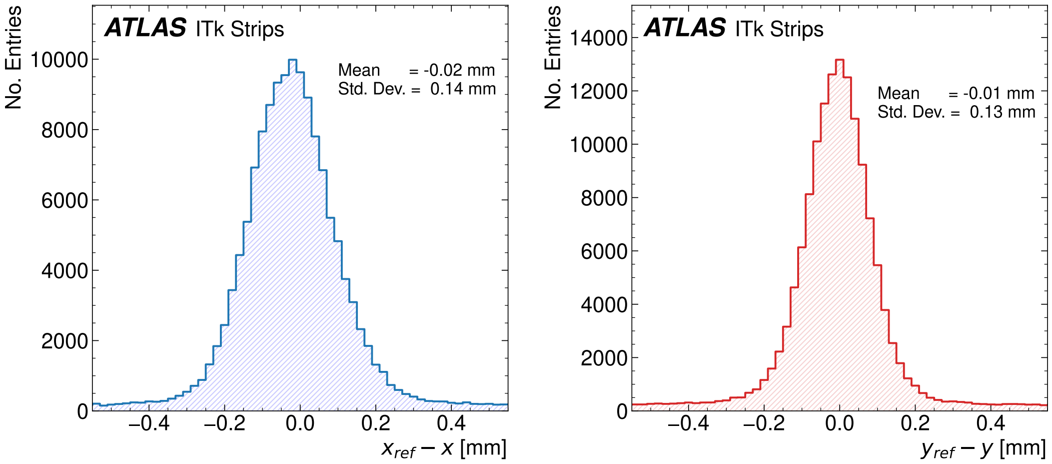

(a) **(b)**

Figure 29.: Correlation plot between the first (taken as reference) and first Mimosa26 sensors at the DESY beam test for (a) the x-coordinate and (b) the y-coordinate.

The Mimosa26 sensors have squared pixels, meaning the distributions should have the same width for ideally aligned detectors. The difference observed between the correlations in Figures 29a and 29b is associated with small misalignments in the angular position of the planes. A cut of ±300 µm in X and Y is set to add a cluster to the track candidate. It should be pointed out that the cuts mentioned are used after the alignment of the planes is completed. During the alignment procedure described in Sections 4.5.7 and 4.5.9, the cuts are relatively large, four times the intrinsic resolution of the planes in a given direction, and reduced to the values containing the entire width of the correlation distributions of the planes, as shown in Figure 29.

The quality of the fitted track can be verified by looking at the χ^2 distribution. Figure 30 shows the $\chi^2/ndof$ distribution of the reconstructed tracks for two different spatial cuts, with $ndof$ standing for the number of degrees of freedom of the fit. The distribution peaks around $\chi^2/ndof \approx 1.0$, indicating that most of the fits and their corresponding reconstructed tracks have good quality.

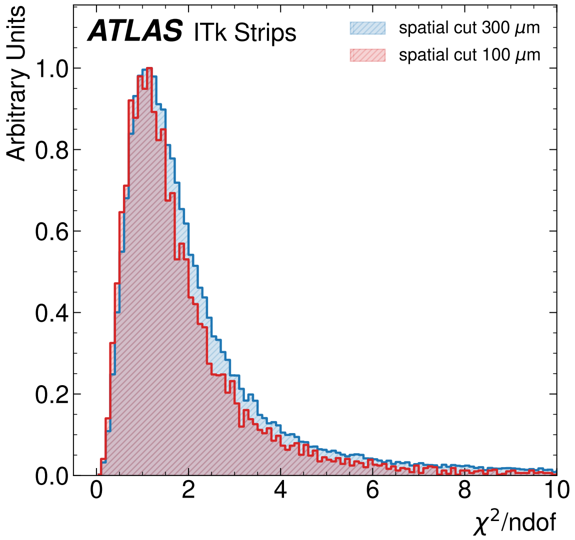

Figure 30.: Reduced χ^2 distribution of the reconstructed tracks in one EUDET-type telescope using two spatial selection cuts for track finding. The distributions are divided by the maximum number of entries for easier comparison and better visualization. The fitted tracks include hits from the Mimosa26 planes and the timing plane. The characteristic peak around 1.0 indicates that most of the reconstructed tracks have good quality.

For the rest of the reconstruction steps and during analysis, the maximum allowed $\chi^2/ndof$ is $\chi^2/ndof \leq 5.0$ to ensure good statistics while keeping only good quality tracks.

4.5.7. Telescope Track-Based Alignment

A correct assessment of the detector performance is not possible if the setup's geometry is not known with high precision because all the track properties strongly depend on the measurement setup's geometrical configuration. Even though the alignment of the detector layers can be performed utilizing laser systems, this approach is not precise enough for a large number of detector modules. In general, even for a few detector planes like in the beam tests, laser alignment is rather cumbersome because it involves physically moving the detector planes. The sensor positions are unknown precisely as they are either in protecting boxes or encapsulated in some holders. In contrast, a track-based alignment provides submicrometer precision. In addition, it does not require any displacement of the detector planes, saving time and reducing the risk of physical damage to the modules.

As previously hinted, the alignment problem appears because the setup geometry is not precisely known. Consequently, an assumption of the initial detector positions, rotations, and sensor bow has to be made, as shown in Figure 31, where the effect of misalignment in the position x-coordinate of one of the planes is depicted.

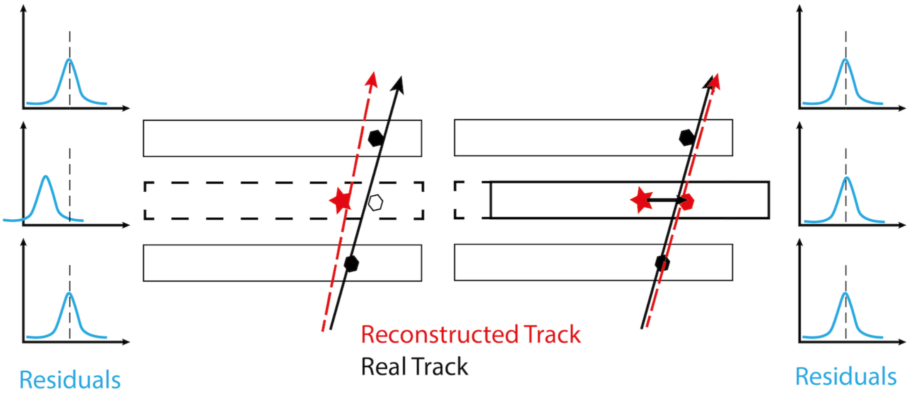

Figure 31.: Schematic representation of the effect of spatial misalignment on the track residual. On the left side, an ideal alignment has been assumed. Because the actual position of the middle plane is displaced with respect to the assumed position, the corresponding residual is not centered around zero. In contrast, when the alignment procedure corrects the position as shown on the right, the residual gets centered around zero.

For the telescope planes, the track-based alignment consists in iteratively varying the positions (X and Y) and rotations (around the x-, y- and z-axes) of all the planes with respect to a reference plane and refitting the tracks to minimize the sum of all track χ^2 values; a task performed using Minuit2 [106, 107]. The alignment process continues until it converges. At this point, no further improvements in the biased residuals[1] of the telescope planes are observed, and the $\chi^2/ndof$ shows a peak at 1.0. The residual is the difference between the track extrapolated intercept position in the detector plane and the associated measured hit position by the detector.

In Corryvreckan, two different modules are employed for the alignment procedure of the telescope planes. First, the X and Y positions of the telescope planes are shifted to be centered around zero. The offsets are taken with respect to the reference plane, whose positions are fixed and define the origin of the coordinate system. This first step, called prealignment, uses the `Prealignment` module in Corrryvreckan and feeds good initial values for the following processes. Figure 32 shows the effect of the prealignment on the correlation plots.

After prealignment, the `AlignmentTrackChi2` module minimizes the sum of the track $\chi 2$ by varying the positions and rotations, plane by plane. It also refits the track candidates. Next, the new optimized geometry is fed into the tracking algorithm to refine the track candidates, which are fed again into the alignment module. This iterative process is repeated until the biased residuals are centered around zero and the $\chi^2/ndof$ distribution peaks around one. Figure 33 shows the telescope residuals before and after the telescope alignment.

---

[1] Biased residual, in this context, refers to the residual obtained for a detector plane, whose hits were included in the track finding algorithm

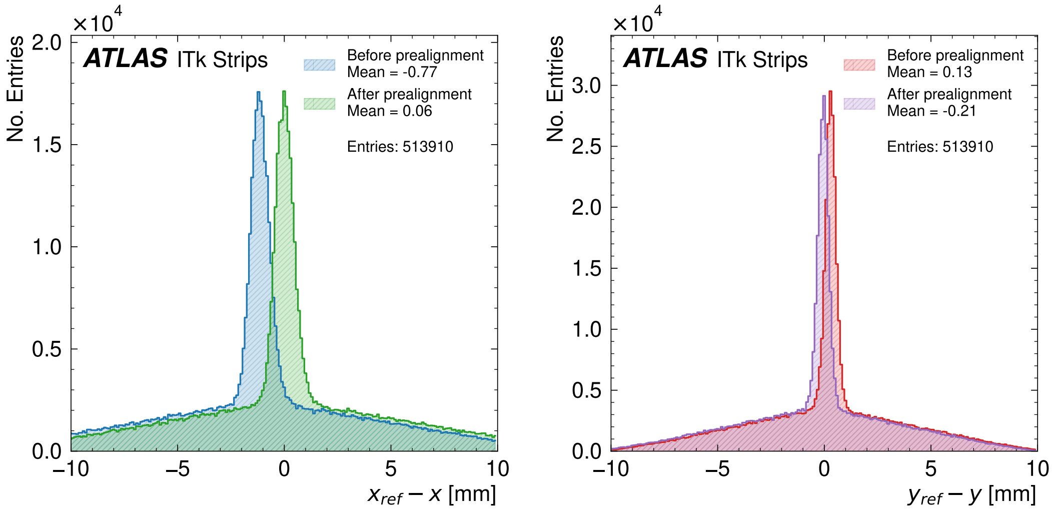

(a) **(b)**

Figure 32.: Mimosa26 correlation plots before and after the prealignment shifts are applied for (a) the x and (b) y coordinate. It is observed how the peaks of the correlations are centered around zero after prealignment. The long tails are associated with multiple particles passing in the same readout window.

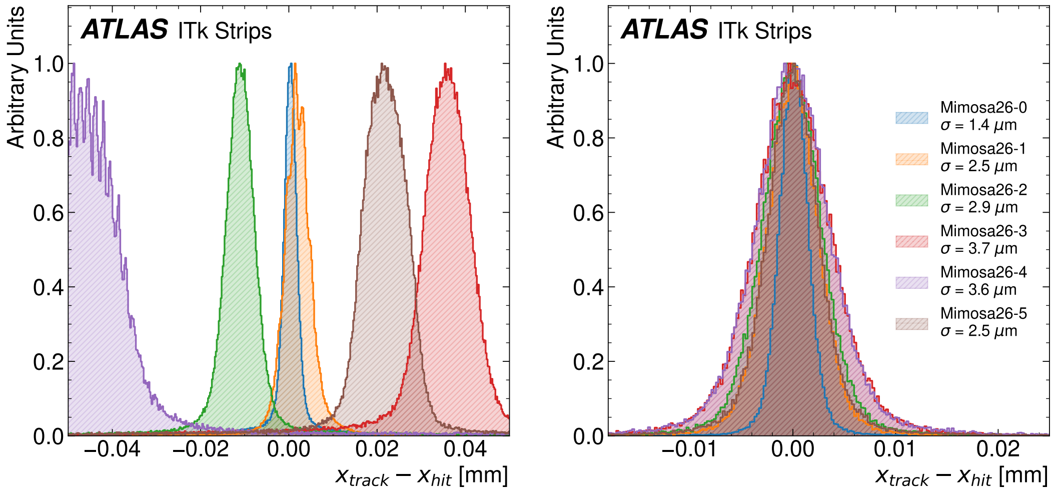

(a) **(b)**

Figure 33.: Residual distribution of the Mimosa26 telescope planes at the DESY beam test facility (a) before and (b) after the alignment procedure is completed. The distributions are divided by the maximum number of entries for easier comparison and better visualization.

Figure 33a shows that the residual distributions of the individual telescope planes are not centered around zero, apart from the first plane, which is used as a reference. This indicates that the assumed x position of the planes is displaced by several micrometers. A similar plot is found for the y position. Moreover, other features are noteworthy when comparing the residuals before and after alignment. The first one is that, in general, the residuals are broader before alignment as misalignment in the position of the planes causes that there are hits associated with the incorrect track, increasing. Additionally, broader residuals are evidence of slight misalignment due to rotation around the x and z-axis. The second effect is that significant misalignment caused by the rotations of the individual telescope planes leads to extra peaks in the distributions, as can be observed for the Mimosa26-4 plane in Figure 33a.

4.5.8. Association of DUT hits to Tracks

As explained earlier, the DUT clusters are not included in the track candidates to avoid biasing the analysis. Therefore, these clusters need to be associated with one of the reference tracks in a different step. The association procedure first calculates the track intercept with the DUT and then associates all clusters in the event within the defined spatial cuts. The decision of whether a cluster is within the cuts can be made by comparing the distance between the track intercept to either the cluster's center or the center of the strip closest to the track intercept within the cluster. The second method minimizes the effect of delta electrons, which can lead to large clusters whose centers are displaced away from the track interception point. Hence, this method is selected for the analysis. The effect of delta electrons is well-known and has been studied, for example, in [108].

Association cuts are determined following the same criteria as for the track finding. The principal difference is that for the ITk Strip modules, the resolution in the direction of the strip is extremely poor. Hence, only the direction perpendicular to the strips, always x in what follows, is considered for the association. The position along the strip length is exclusively examined to check if the track intercepts are within the DUT. The analysis presented in Chapter [**?**] used association cuts ranging from 100 to 150 μm.

4.5.9. Track-Based DUT Alignment

The alignment of the DUT follows a procedure analogous to the telescope. First, a prealignment is performed using the `Prealignment` module in Corryvreckan, which centers the DUT's x and y positions and serves as a good initial parameter for the alignment. The value of the translations is obtained from the spatial correlations between the DUT clusters and the reference tracks. Then, the alignment step, performed with the `AlignmentDUTResiduals` module, minimizes the root-mean-square (RMS) value of the spatial residual distribution of the DUT by varying the positions and rotations of the DUT [106, 107]. The position along the beam, which coincides with the z-axis (see Figure 22), is a weak mode for the alignment as translations along this axis have almost no effect on the residuals and the χ^2 of a track. Therefore,

z positions need to be measured precisely as they are used to calculate the track intercepts with the DUT and in the track fitting algorithm. Consequently, only the x and y translations are aligned for the DUT. In strip sensors, the rotations about the direction along and transversal to the strip in the sensor plane are also weak modes for the alignment. Thus, only the rotation about the z-axis is aligned. An example of a residual distribution for an ITk Strip LS module is shown in Figure 34 before and after alignment.

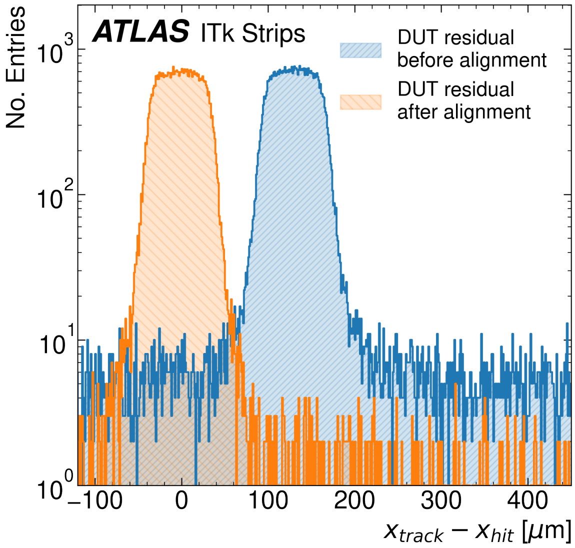

Figure 34.: Residual distribution for a non-irradiated ATLAS ITk Strip LS module before and after the alignment procedure is finished.

It can be observed that after alignment, the residual is centered around zero, and its tails are about one order of magnitude smaller because the alignment reduces the number of mismatched and noisy hits. The unbiased residual distributions allow us to estimate the position resolution of the DUT and are the first figure of merit to evaluate during a beam test analysis.

4.6. Spatial Resolution

The strip pitch and the inherent statistical fluctuations of the deposition and collection of the charge limit the precision of the reconstructed hit position. Hence, the reconstructed position on the DUT is, in most cases, displaced with respect to the track's position. The spatial resolution σ_x[2], can be defined as the integral over the probability $P(x_{hit}, x_{track})$ that the position x_{hit} is reconstructed for the track position x_{track} and given by [109].

---

[2] Here x does not refer uniquely to the x-coordinate. It rather denotes a given measurement direction.

$$\sigma_x^2(DUT) = \int P(x_{hit}, x_{track})(x_{hit} - x_{track})^2 \mathrm{d}x_{hit}. \tag{32}$$

The difference between the position of the track intercept and the center of the associated cluster, $x_{track} - x_{hit}$, is called the unbiased residual, and the RMS of its distribution is employed to estimate the DUT spatial resolution $\sigma_x(DUT)$. The residual is called unbiased because the DUT cluster has not been included in the track reconstruction; hence, the track fit is not biased by the position of the DUT cluster.

It is essential to notice that the total width of the unbiased residuals is a convolution of two factors; the resolution of the reference telescope and the intrinsic resolution of the DUT. Assuming a Gaussian residual distribution, the telescope's resolution can be subtracted in quadrature as in Equation 33.

$$\sigma_{DUT} = \sqrt{\sigma^2_{measured} - \sigma^2_{telescope}}. \tag{33}$$

When the resolution of the telescope is much smaller than the one of the DUT, $\sigma_{telescope} \ll \sigma_{DUT}$, the influence of the telescope can be neglected and

$$\sigma_{DUT} \approx \sigma_{measured}. \tag{34}$$

The definition given in Equation 32 is general and takes specific forms depending on the cluster types and, consequently, also on the type of readout employed. For binary readout, it is not difficult to demonstrate that the spatial resolution for cluster size one, i.e., a single strip fires, is given by Equation 26. Assuming that the reconstructed track has an infinitely small resolution and a uniform collected charge across the strip pitch, the expected shape of the unbiased residual would be a box distribution with a width equal to the strip pitch. However, the telescope resolution is finite; therefore, the DUT residual distribution shows smeared edges.

4.7. Hit Reconstruction Efficiency

The hit reconstruction efficiency for a given threshold is the most important parameter evaluated at a beam test. The efficiency is obtained as the ratio between the tracks detected in the DUT and the total number of reconstructed tracks that pass through the DUT detection area, which are known as reference tracks. Hence, the efficiency corresponds to the probability of detecting a particle passing through the detector

$$\epsilon = \frac{k}{N}, \tag{35}$$

with k being the number of tracks with an associated cluster in the DUT and N being the total number of reference tracks. The efficiency, defined by Equation 35, can be regarded as a set of Bernoulli trials and, therefore, described by binomial statistics. Moreover, the likelihood function of obtaining the actual efficiency values for the measured number of DUT hits and reference tracks follows a binomial distribution [60]

$$L(\epsilon|k, N) = \binom{N}{k}\epsilon^k(1-\epsilon)^{N-k}. \tag{36}$$

The uncertainty is then calculated using a Clopper-Pearson confidence interval of $\pm 1\sigma$, corresponding to the central 68.3% of the binomial distribution with upper and lower limits of 1 and 0, respectively. This method is recommended by the Particle Data Group [60]. Furthermore, it is the default method for error calculation of the `TEfficiency` class [110, 111] in the ROOT framework, which is used by the Corryvreckan modules carrying out the detector efficiency analysis.

4.8. Selection Cuts in the Efficiency Analysis

Section 4.2.1 indicated that, due to the significant difference between the integration times of the telescope and the ITk DUTs and the fact that the trigger timestamp is not recorded by any of the detectors involved in the data taking, hit ambiguities appear. Therefore, an extra detector plane is required to provide a timing tag of the tracks. Figure 35 illustrates the situation without and with a time reference plane. The TLU offers a precise trigger timing of about 2 ns. However, only one trigger ID is saved for Mimosa26 and the DUT readout frame.

When only one particle passes through in one Mimosa26 readout frame (see Figure 35a), there is no ambiguity in identifying which hit in the Mimosa26 triggered the readout. However, when there is more than one particle in one frame of the M26, it is impossible to identify which of the two or more tracks detected by the telescope planes should be compared with corresponding hit/no-hit information in DUT. This scenario is shown if Figure 35b. The ambiguity is resolved by adding another detector plane with the same integration time as the DUT and requiring that all reconstructed tracks have one hit on this plane.

Figure 35c shows the case when the DUT recorded the particle (high efficiency), while Figure 35d when the DUT missed the hit (low efficiency). The effect of not having a time reference plane can have a high impact on the measured efficiency of the DUT due to the track multiplicity at DESY. Figure 36 shows the measured track multiplicity within one readout frame of the M26 detector for positrons of 5.2 GeV in the DATURA telescope. The average track multiplicity is around 2.6 tracks per frame, making the scenario in Figure 35b the most probable.

Consequently, to measure the DUT efficiency, the tracks must fulfill the requirement of having an associated cluster in the timing plane. Hence, the efficiency from Equation 35 is modified to include only the reference tracks that match this criterion.

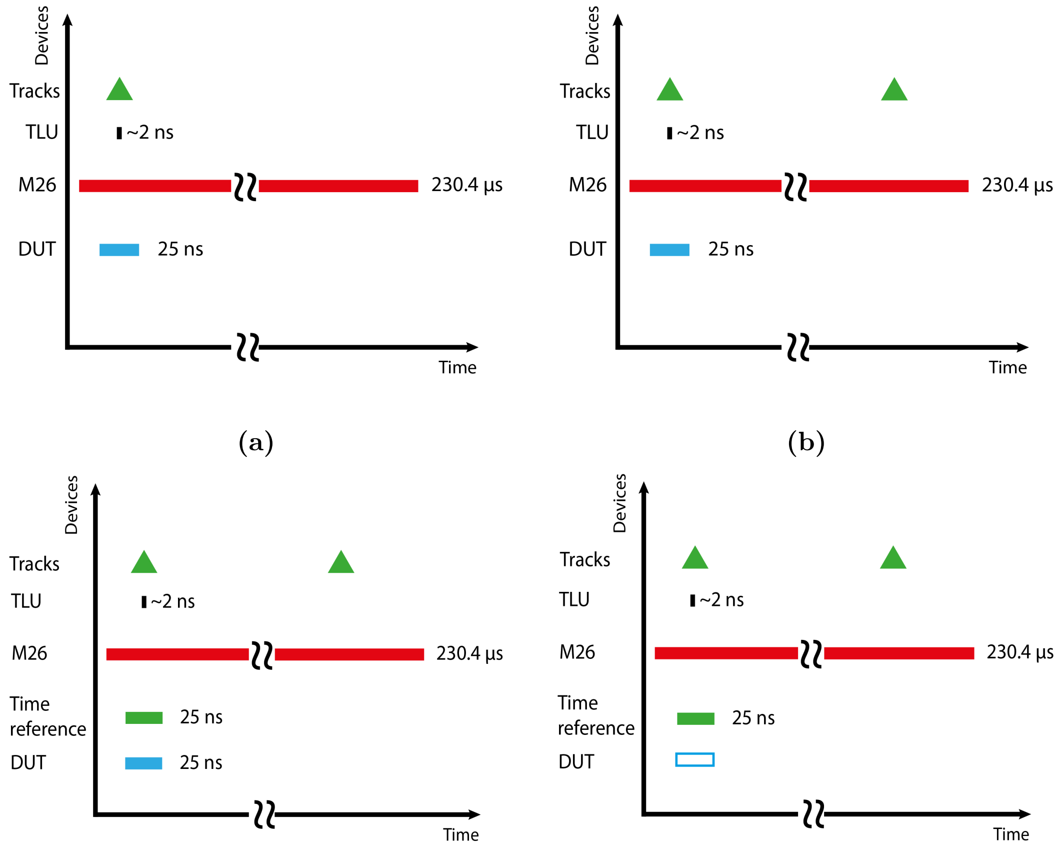

(a) (b)

(c) (d)

Figure 35.: Timing at the ATLAS ITk beam tests. The upper left schematic depicts the case where only one hit is recorded in one readout frame of the Mimosa26 plane, while the upper right depicts the case where two hits are recorded within a readout frame. It can be seen that using only the Mimosa26 information is impossible to know which track generated the hit on the DUT. The bottom schematics show the cases where the timing plane tags the track and allows determining if the DUT detected the track (left) or not (right).

$$\epsilon = \frac{tracks_{with\ DUT\ cluster}}{tracks_{telescope+timing\ plane}}\ . \tag{37}$$

As mentioned, the timing plane used is a pixel sensor with an array of 336×80 pixels with a pitch of 50 µm × 250 µm providing a total active area of 1.7×2 cm^2 [99] and is read out by the FE-I4 ASIC. This type of detector is used in the ATLAS Insertable B-Layer [44], and therefore, it has an integration time of 25 ns as the ATLAS ITk Strip modules.

It is also important to consider that during the beam tests, there is no external clock synchronizing the time of arrival of the tracks with the readout time of the DUT. As a consequence, the peaking time of the signal does not always match the

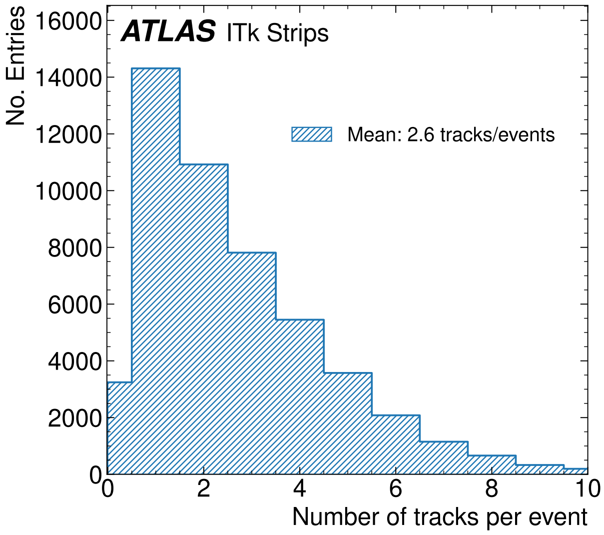

Figure 36.: Track multiplicity in the DATURA telescope. Many events have two or more reconstructed tracks, making the scenario of Figure 35b highly probable, reinforcing the necessity of having a time reference plane.

readout time of the DUT. The latter means that hits from tracks arriving too early or too late will not be recorded, and thus, this is counted as inefficiency. Accordingly, a time delay cut is applied where only events with the peaking time of the signal matching the DUT readout window are selected. Figure 37 shows the efficiency as a function of the arrival time of the tracks for various thresholds for an unirradiated LS module tested in April 2019. The 1.56 ns steps in the x-axis are given by the sampling frequency of the TLU trigger signal, which is 640 MHz [112].

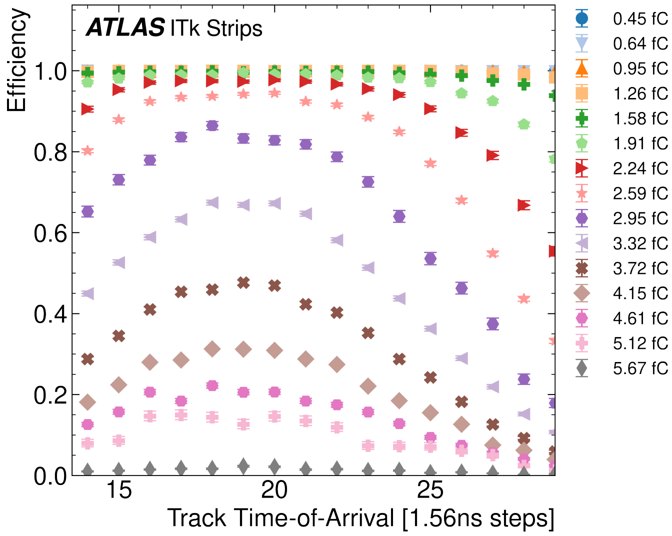

Figure 37.: Efficiency as a function of the arrival time of the tracks for various thresholds for a non-irradiated LS module tested in April 2019.

Two distinctive features are observed. For low and high thresholds, up to 1.26 fC and above 4.61 fC, the efficiency does not depend on the time of arrival of the tracks. However, as discussed in Chapter 5, these two sets of thresholds cannot be used for selecting the time cut. In the low range, the noise occupancy is too high, while for high thresholds, the signal generated by the particle is not large enough to be recorded as a hit.

The second feature is that for thresholds between 1.26 fC and 4.61 fC DAC, the efficiency curves can be regarded as the pulse shape of the signal. Thus, a time cut containing this pulse's peak is selected. The delay time depends on the connections and cabling used at each beam test, so the cuts must be applied for each DUT and test campaign independently.

The efficiency is studied during the beam tests as a function of the threshold set in the input channel discriminators. The latter is a common way of studying binary detection systems [113] and allows for measuring the integrated charge distribution. Scanning the discriminator threshold and obtaining the efficiency for each step leads to the so-called “s-curve” shown in Figure 38.

The threshold is expressed in charge units through a calibration process, discussed in Section 4.9. The efficiency s-curve obtained at the beam tests is fitted with an empirical skewed complementary error function [114]

$$\epsilon = \frac{\epsilon_{max}}{2} \cdot erfc\left\{ \frac{q_{thr} - \mu}{\sqrt{2}\sigma} \left[1 - 0.6 \cdot \tanh\left(\xi \frac{q_{thr} - q_M}{\sqrt{2}\sigma} \right) \right] \right\}, \qquad (38)$$

where $erfc$ is the complementary error function, q_{thr} is the applied threshold, and the hyperbolic term models the influence of the Landau in the Landau-Gauss convolution described in Section 3.1.1. The other fit parameters are

- ϵ_{max} is a scaling factor corresponding to the maximum efficiency such that $\epsilon_{max} \in [0, 1]$,
- q_M is the median charge that gives the threshold value at which the efficiency is 50%,
- σ is the width of the error function, which is related to the noise and the width of the Landau distribution,
- ξ is the skew parameter and accounts for the asymmetry of the Landau distribution.

The median charge, chosen instead of the most probable value of the Landau-Gauss distribution, is used to estimate the signal-to-noise ratio. When binary readout is employed, the clustering algorithm does not recover the charge shared with the neighbors if the collected charge in the neighbor is below the applied threshold. Hence,

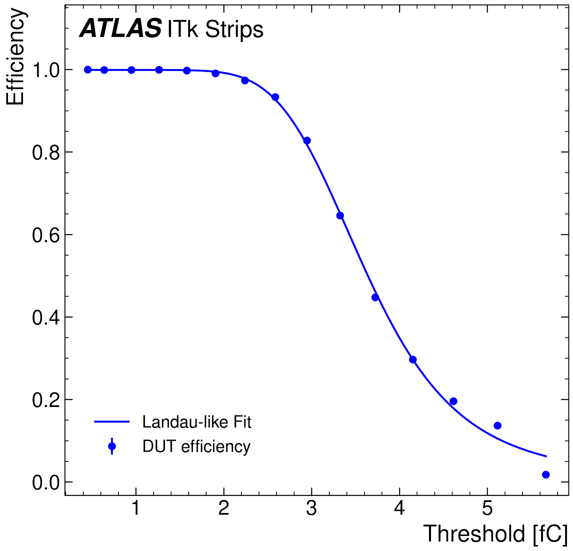

Figure 38.: Efficiency as a function of the applied threshold in the front-end discriminator of each channel for a non-irradiated LS module tested in April 2019.

the MPV of the Landau-Gauss convolution is not measured accurately. Studies have shown [108] that charge sharing due to cross-talk, diffusion, and $\delta-$electrons are the three main mechanisms contributing to the loss of charge in the binary readouts. The total effect has been estimated to result in a 10% difference between the MPV and median charge [108, 114].

4.9. Threshold Calibration

All tested modules are electrically characterized before and several times during the data taking. This characterization evaluates the performance of the readout electronics and provides the parameters necessary for the calibration of the thresholds applied at the channel discriminators. Each channel threshold is set through a Digital-to-Analog Converter (DAC), and its value is given in units called DAC. Even though these units are convenient for the detector operation, they do not offer information about how much charge must be collected to detect a hit. Therefore, a calibration that gives the relation between DAC and fC units is employed.

The calibration consists of two steps. The first is the conversion from DAC units to mV, which is the physical unit of the threshold set at the discriminators of the channels. The second one is to convert the threshold value from mV to fC. The relation between the DAC counts and the threshold in mV is not linear over the full range of thresholds [51]. Therefore, simulations of the response are employed to improve the accuracy of the conversion [51]. An example of the relation obtained in simulations is shown in Figure 39.

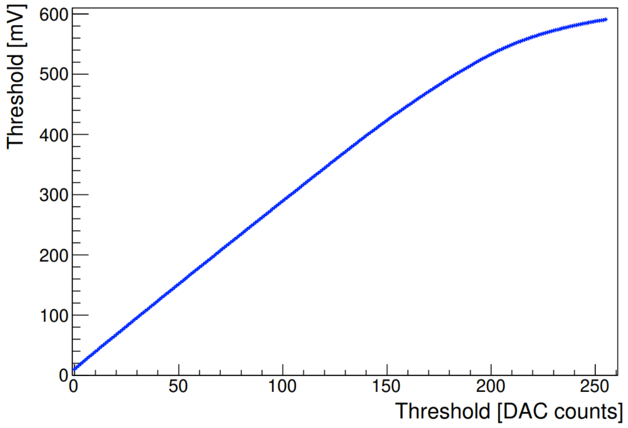

Figure 39.: Dependence between the threshold values specified in DAC units and the real physical thresholds set at the discriminators of the ABC130 front-end obtained from simulations [51].

The ABC front-end has an internal calibration circuit in all its versions. This circuit sends voltage pulses with the 40 MHz clock to a capacitor (60 fF ±10%) to generate a signal with a charge between 0 and -9 fC [51].

The so-called response curve gives the relation between the input charge and the output voltage. A threshold scan is performed in which well-known charges are injected into the readout channels to obtain the response curve. The result of this experiment for each injected charge should be a step function, but noise smears the response into an s-curve, as explained earlier.

The first derivative of the s-curve resembles the distribution of the collected charge, and its standard deviation gives the output noise. The median value of the distribution, known as Vt50, is the threshold value at which the channel fires 50% of the time [51] and corresponds to the median value of the injected charge. These Vt50 values are plotted as a function of the injected charge, resulting in a response curve like the one shown in Figure 40.

The response curve is fitted with an empirical function that allows extracting the gain of each channel. The fitting function has the form [115]

$$\mathrm{Vt50}(q_{inj}) = C_1 + \frac{C_0}{1 + \exp\left(-q_{inj}/C_2\right)}, \tag{39}$$

where $C_{0,1,2}$ are free parameters of the fit and q_{inj} is the injected charge. In addition to providing the threshold calibration, the Response Curve test is also used to determine the gain and noise of the device. The gain is derived from the gradient of the response curve, and the input noise is calculated by dividing the output noise by the gain [115]. The calibration is subject to fluctuations due to several factors, including manufacturing process variation, radiation damage, and temperature

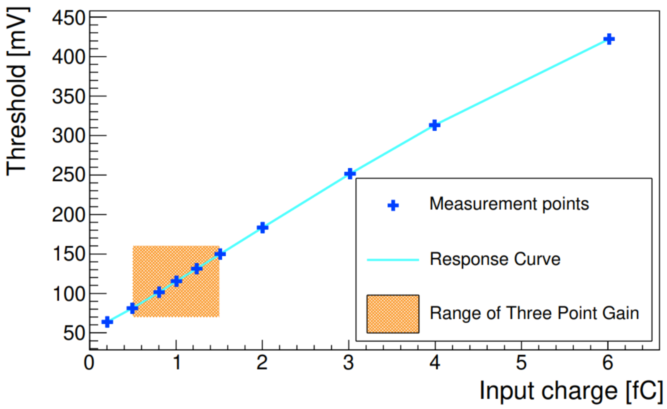

Figure 40.: Response curve averaged over all readout channels on an ABC130 readout chip. A linear relation between the input charge and the output voltage is observed for low thresholds, while a non-linear response is observed for high thresholds. The input charge range covered in a Three Point Gain scan, a rapid evaluation test, is highlighted in orange [51].

changes. Consequently, the calibration must be performed for each setup of the tested DUT in a given test beam campaign to guarantee that the values correspond to the actual data-taking conditions.

4.10. Noise Occupancy

The noise occupancy is evaluated by counting how many noise hits are recorded in each channel for a given threshold. The occupancy measurement can be performed using one of the ITSDAQ tests [51, 116], where different sets of thresholds and the number of triggers sent are configurable. The second method for evaluating noise occupancy, a pedestal run, uses the auto-trigger function of the TLU. In this case, the beam is turned off, and the threshold at the discriminator channel is set via EUDAQ2.

Independently of the method employed, it can be shown [76] that, in a binary detector system, the logarithm of the noise occupancy is inversely proportional to the applied threshold:

$$\log P_n = \log\left(\frac{\Delta t}{4\sqrt{3}\tau}\right) - \frac{1}{2}\left(\frac{Q_t}{Q_n}\right)^2, \tag{40}$$

where

- P_n is the noise occupancy,
- Δt is the sampling time interval,
- τ is the time constant of an RC low pass filter,

- Q_t and Q_n are the applied threshold and the equivalent noise charge, both given in fC.

The slope of the dependence of the logarithm of the noise occupancy on the squared threshold in units of fC^2 gives the system noise. Figure 41 shows a typical result for the ABCStar ASICs. The uncertainty is larger for higher thresholds due to the low occupancy values.

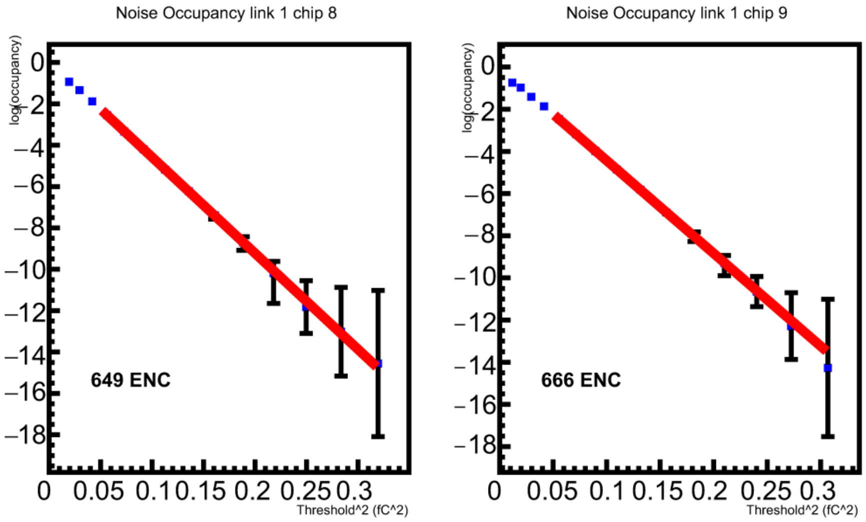

Figure 41.: Exemplary noise occupancy behavior as a function of the applied threshold for an ABCStar ASIC [117].

4.11. Module Electrical Characterization at the Beam Test

As was mentioned, the modules are characterized before the beam test starts. This electrical characterization aims to optimize the readout electronics for data taking. In addition, the characterization identifies noisy channels, faulty chips, and communication problems that otherwise would affect the data quality.

The characterization comprises the following tests:

- Capture HCC and ABC IDs: Checks communication with all the ASICs.
- Strobe delay: Adjusts the charge injection time of the internal calibration circuit in the front-end chip.
- Trim range: Ensures a uniform response of all module channels to which the same readout threshold is applied.
- Three-point gain: Similar to the earlier response curve, see Section 4.9, but only with three different charges injected.

More details on the electrical characterization of the ITk Strip modules can be found in [51], while a comprehensive set of electrical characterization results of the ITk Strip modules is discussed in [117].

Chapter 5

Beam Test Reconstruction and Analysis

5.1. ATLAS ITk Strip Modules Tested at DESY

Six types of ATLAS ITk Strip modules have been tested since 2018. This section offers a short description of the modules analyzed in the thesis. The tested prototypes comprised the two barrel module types, Long Strip (LS) and Short Strip (SS), and the R0 and R2 endcap modules. Different sensor design iterations and front-end electronics versions, the ABC130 and the ABCStar chipset, were used. As explained in Section 2.6, the sensors used by the ITk Strip modules have up to four strip rows. The strip segments covered by the hybrids are identified as “Under” while the uncovered are labeled as “Away”(Appendix C).

Double-Sided R0 Module 2018

Strip detectors have poor resolution along the strip length. To improve the resolution in this direction, stereo layers are used as described in Section 3.6.1. The double-sided R0 (DSR0), built in Freiburg, is the only ITk Strip prototype built with stereo layers. The DSR0 features two independent, fully equipped R0 modules (labeled R0-F0 and R0-F1) using ATLAS12EC sensors [52], glued back to back to a carbon fiber honeycomb structure. The honeycomb has titanium cooling pipes and specially designed bus tapes glued onto each side. The bus tapes carry the module control signals, data transmission, and powering. The structure emulates the final assembly of the ITk Strip petals on a smaller scale.

More details on the building process and the electrical characterization can be found in [118]. Each R0 module features two hybrids (R0H0 and R0H1), populated with the ABC130 [51] readout chips, HCC130, and a powerboard with a DC-DC converter. Figure 42 shows a picture of the DSR0 facing a mirror making the two sides visible. The module was not irradiated.

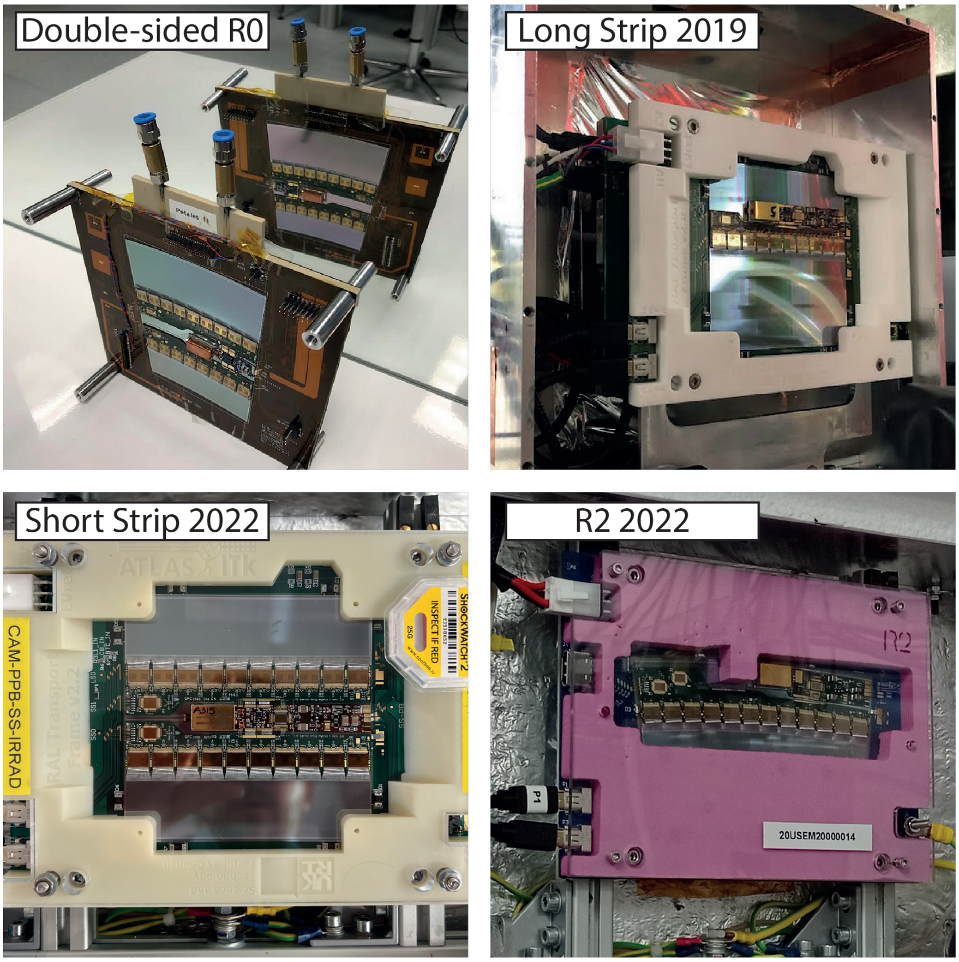

Figure 42.: Pictures of different ATLAS ITk Strip modules tested at the DESY beam test campaigns. Top left double-sided R0, top right LS 2019 modules, bottom left SS 2022, and bottom right R2 2022.

Long-Strip Star Module 2019

Long-Strip modules are located in the two outermost layers of the ATLAS ITk barrel and have a powerboard and only one hybrid. The LS 2019 was built using an ATLAS17LS sensor [119]. No irradiation was performed. The module is shown in Figure 42.

R0 Star Module 2019

The R0 module was built at Rutherford Appleton Laboratory (RAL) and tested in 2019. It features the same ATLAS12EC sensor type as the DSR0, while the readout electronics employed the Star chipset version ABCStarV0, HCCStarV0 for the first time. The module was not irradiated. The R0 and the LS modules tested in 2019 were the first to feature the Star chipset from the endcap and barrel, respectively.

Irradiated Short-Strip Module 2021

The SS module 2021 was built at RAL from irradiated components. It uses the ATLAS18SS and pre-production A[1] (PPA) components, which comprise ABCStarV1 and HCCStarV0, and the AMAC-V2a ASIC [120]. The sensor was neutron-irradiated at the Jozef Stefan Institute in Ljubljana [121, 122] to a fluence of 1.1×10^{15} $\mathrm{n}_{eq}/\mathrm{cm}^2$, while the PPA electronics received a total ionizing dose (TID) of 58 Mrad from X-ray at RAL. The fluence and dose values correspond to the maximum expected fluence and TID, including a safety factor of 1.5 and 1.8, respectively, for the SS modules at the end of the HL-LHC operation.

Irradiated Short-Strip Module 2022

The SS module 2022 was built at Cambridge University from an irradiated ATLAS18SS sensor. In contrast to the SS in 2021, the module uses the pre-production B (PPB) components: ABCStarV1 and HCCStarV1 and the AMACStar chip [123, 124]. The sensor was neutron-irradiated at the Jozef Stefan Institute in Ljubljana to a fluence of 1.1×10^{15} $\mathrm{n}_{\mathrm{eq}}/cm^2$, which as the for SS in 2021 equals the maximum expected fluence, including a safety factor of 1.5, at the of the module lifetime. The readout chipset was not irradiated. Figure 42 shows a picture of the module.

Irradiated R2 Module 2022

The R2 module 2022 was the first of its type tested at a beam test. It was built at TRIUMF/Simon Fraser University from a neutron and gamma-irradiated ATLAS18R2 pre-production sensor. The module uses PPB components. Neutron irradiation occurred at the Jozef Stefan Institute in Ljubljana to a fluence of 1.1×10^{15} $\mathrm{n}_{eq}/\mathrm{cm}^2$, while the gamma irradiation employed a ^{60}Co source for a dose of 66 Mrad at Charles University in Prague. As for the other irradiated modules, the fluence equals the maximum expected fluence at the end of the operation at the HL-LHC, including a safety factor of 1.5. The TID was three 3.1 times the expected dose at the end of the HL-LHC operation. The module is shown in Figure 42 during the beam test campaign.

Table 6 in Appendix C summarizes the studied modules, including the sensor and readout electronics versions used. In addition, the irradiation fluences and doses the modules received are compiled.

---

[1] Pre-production accounts for 5% of production. Pre-production A corresponds to the first 20% of the pre-production, while pre-production B is the remaining 80%.

5.2. Hit Detection Efficiency

The hit detection efficiency is defined as the probability of detecting a traversing ionizing particle as described in Section 4.7.

5.2.1. Threshold Dependence

Section 4.8 described how a threshold scan is employed for characterizing the performance of detection systems with binary readout and should lead to a relation between the efficiency and the applied threshold at the discriminator expressed by an s-curve. Figure 43 shows the hit detection efficiency for five ITk Strip modules as a function of the applied threshold in fC. The efficiency of all modules follows the expected s-curve shape, and considerable differences are observed between non-irradiated and irradiated modules.

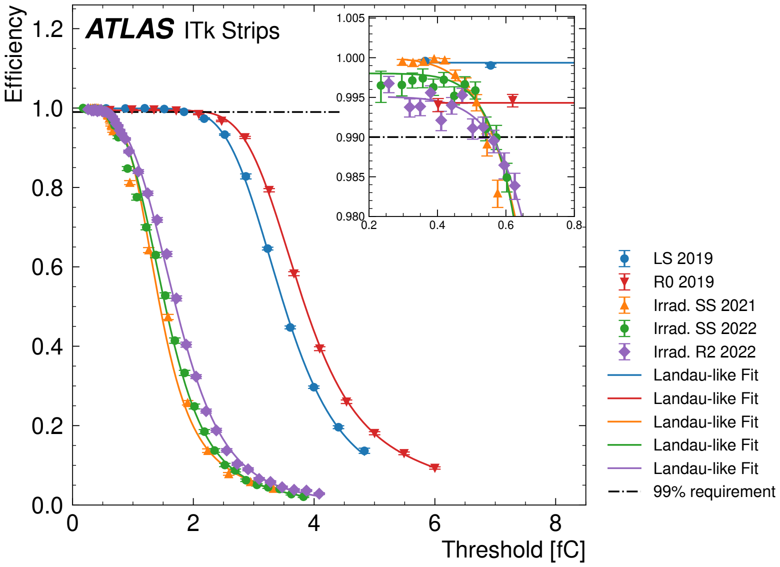

Figure 43.: Efficiency as a function of the applied threshold in the channel discriminators for four different modules (LS 2019, R0 2019, SS 2021, R2 2022, and SS 2022). The SS 2021 module was built using a $1.1 \cdot 10^{15}$ $\mathrm{n_{eq}/cm^2}$ neutron irradiated sensor and readout electronics irradiated with 58 Mrad X-rays. The SS and R2 2022 module sensors were irradiated to a fluence of $1.1 \cdot 10^{15}$ 1 MeV $\mathrm{n_{eq}/cm^2}$ with neutrons. The SS 20222 readout electronics were not irradiated, while the R2 readout electronics received a dose of 66 Mrad using gammas rays. The SS and R0 2019 modules were not irradiated.

Non-irradiated modules exhibit a wider range of thresholds, approximately up to 1.9 fC (11.9 ke$^-$), with efficiency above 99%. As expected, the efficiency decreases appreciably for larger thresholds. With the threshold increase, only events with large charge depositions can produce hits in the DUT. The efficiency decreases as the fraction of these events is small according to the Landau distribution, see Section 3.1.

The same trend is observed for irradiated modules. However, the threshold range for which the efficiency remains above 99% is significantly reduced compared to the non-irradiated modules. The range only reaches up to 0.6 fC (3.7 ke$^-$), as seen from the inset in Figure 43. This reduction corresponds to a 69% decrease in the performance of the modules, and it is a direct consequence of the damage produced by irradiation. The damage causes the loss of charge collection efficiency owed to charge carrier trapping in defect levels within the bandgap. The effect on the collected charge can be quantified by comparing the median charges of the modules (Section 4.8). The median charge is obtained as a fit parameter from a non-linear least square fit of the efficiency vs. threshold behavior using the function defined in Equation 38. The median change value obtained for the Long Strip module is 3.6 fC (22.5 ke$^-$). For the irradiated Short Strip modules, the values are 1.4 and 1.5 fC (9.4 ke$^-$) for the 2021 and 2022 beam test campaigns, respectively, representing a deterioration of about 59%. Table 2 compiles all the median charge values obtained for the modules in Figure 43. The errors are obtained as the square root of the diagonal elements of the estimated fit covariance matrix.

Table 2.: Module median charge values obtained from the fit of the s-curves. Two values are reported: μ_{center} is the estimated value resulting from using tracks passing within ± 15 μm from the strip center, while μ is the value derived using the whole strip pitch.

Module	μ_{center} [fC]	μ_{center} [ke$^-$]	μ [fC]	μ [ke$^-$]
LS 2019	3.65 ± 0.01	22.8 ± 0.06	3.55 ± 0.01	22.2 ± 0.06
R0 2019	3.91 ± 0.03	24.4 ± 0.19	3.86 ± 0.01	24.1 ± 0.06
Irrad. SS 2021	1.69 ± 0.01	10.5 ± 0.06	1.47 ± 0.01	9.18 ± 0.06
Irrad. SS 2022	1.78 ± 0.01	11.1 ± 0.06	1.54 ± 0.01	9.61 ± 0.06
Irrad. R2 2022	1.92 ± 0.02	12.0 ± 0.12	1.71 ± 0.03	10.7 ± 0.25

A better estimate of the median charge can be obtained by restricting the measured hit reconstruction efficiency to tracks passing within less than 15 μm distance from the strip center. Charge sharing is vastly reduced for those events, and the collection happens in a single strip. Thus, this track selection reduces the collected charge loss mechanism, improving the median charge measurement. The median values obtained using tracks passing within ±15 μm are summarized in Table 2. Figure 44 compares the efficiency measured over the entire strip to the efficiency when the tracks pass within 15 μm from the strip center for the irradiated SS 2022 module.

At thresholds below 0.6 fC, it is observed that there is no difference between the measured efficiency considering tracks passing anywhere and tracks passing close to the strip center, labeled as “center” in the plot. For higher thresholds, up to 3 fC, the efficiency measured using only the tracks passing close to the strip center is always higher. This is expected as the charge is not shared between more than one strip.

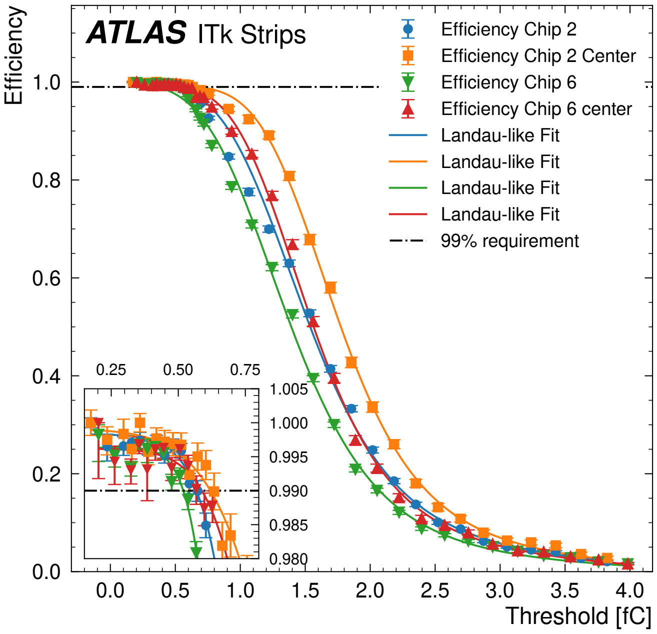

Figure 44.: Comparison of the measured hit detection efficiency as a function of the applied threshold in the channel discriminators for tracks passing through the entire strip and tracks passing within 15 µm from the strip center in the Irradiated SS 2022 module. Two different positions are shown.

For even higher thresholds, the center of strip efficiency is still higher, although the differences are minimal. In this case, the threshold is extremely high, and the effective pitch of the strip is reduced. Consequently, tracks not traversing the strip near its center have an extremely low probability of producing a hit. For non-irradiated modules, the differences between the median charges using the center of the strip and the full width are below 3%. The differences are more pronounced in the irradiated module and range between 12 and 16%.

It has been established that the key ingredient for obtaining high hit reconstruction efficiency is the amount of charge the sensor collects, which is why the sensors are operated at a higher or equal to the full depletion voltage. Therefore, evaluating the module efficiency at different operating voltages is relevant. Figure 45 shows the hit reconstruction efficiency for one of the R0[2] modules from the 2018 campaign. The module efficiency is higher than 99% at the full depletion voltage of 300 V and decreases at 200 and 100 V. At these lower voltages, the efficiency is no longer above 99%, even at lower thresholds. The reduction of the collected charge causes the observed efficiency loss.

---

[2] While the DSR0 module tested in 2018 is physically a single module, the two R0 sensors and electronics were read out independently. This allowed studying each of the R0 modules separately

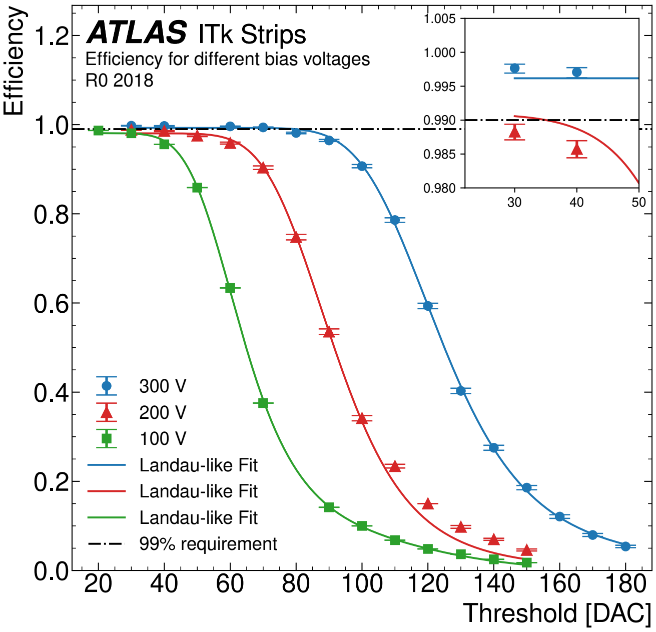

Figure 45.: Efficiency as a function of the applied threshold in the channel discriminators for three different bias voltages (100 V, 200 V, and 300 V) for the R0-F1 in 2018.

At voltages below full depletion, the charge deposited in the under-depleted volume is collected via diffusion as no electric field is present. Thus, charges move slower, decreasing their contribution to the induced charge in the electrodes within the total integration time of the detector. In addition, the slower movement also increases the recombination probability. Both mechanisms reduce the collected charge, where the median charge decreases with the bias voltage, as is observed in Figure 45.

5.2.2. Noise Occupancy

The logarithm of the noise occupancy is shown in Figure 46a as a function of the threshold and in Figure 46b as a function of the threshold square for five different modules. The occupancy behavior can be divided into two threshold ranges for all the modules. The first range extends to $\simeq$ 0.1-0.4 fC (0.6-2.5 ke^{-}), and the second reaches from 0.4 fC to 0.8 fC, see Figure 46a.

In the first interval, the occupancy decrease with the threshold is slower compared to the second interval, where a steeper decrease with the threshold is observed. The first interval is dominated by correlated noise, which can be originated from the discriminator output pulses feeding back into the pulse shaper and these being fed back into the discriminator input. The exact mechanisms leading to the generation of the correlated noise are specific to the ASIC design and not fully understood. However, these effects. However, these effects happen at very low thresholds where the occupancy does not meet the operation requirements. Thus, the interval has no significance for evaluating the noise behavior of the modules.

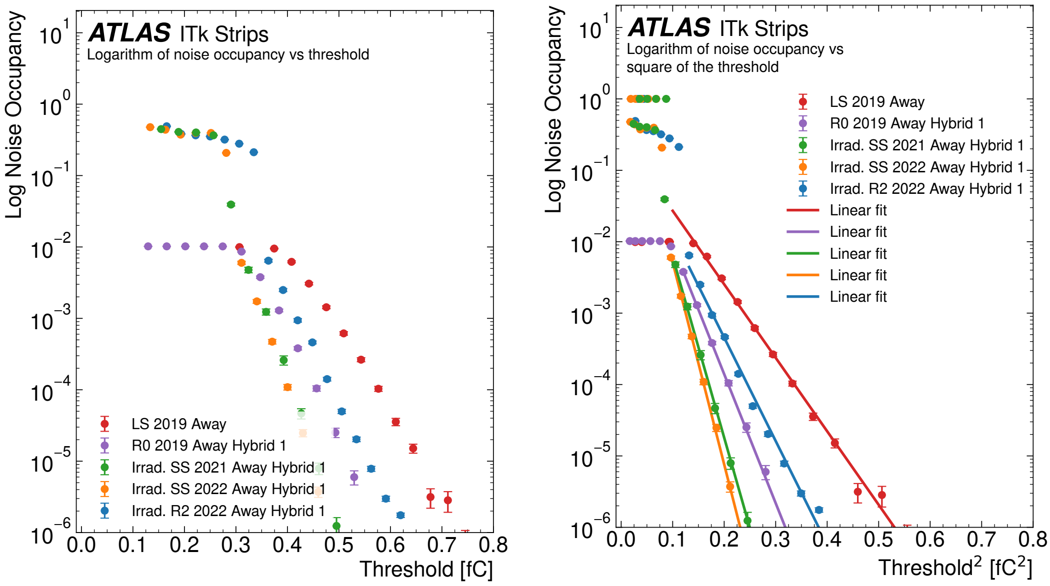

(a)

(b)

Figure 46.: Logarithm of noise occupancy as a function of (a) the applied threshold and (b) the square of applied threshold in the channel discriminators for four different ATLAS ITk modules investigated at the beam tests.

In addition, it is observed that the LS and R0 noise occupancy saturates at low thresholds around 10^{-2}. A software malfunction caused this behavior. The ABCStar uses an 8-bit counter; thus, the hit count cannot exceed 255. The noise occupancy test should start by sending fewer triggers, around 250, and only increasing the number of triggers sent when the occupancy goes down far enough that the expected hit count is still less than 255. For the LS and R0 modules, the software sent twenty-five thousand triggers at all threshold levels, consequently saturating the counter.

In the second interval, it is observed that the non-irradiated LS 2019 module presents the largest noise occupancy, reaching the 10^{-3} requirement at 0.46 fC, while the two irradiated SS modules showed the smallest values (10^{-3} at 0.36 fC and 0.35 fC for 2021 and 2022) with the R0 and R2 module occupancy, 10^{-3} at 0.42 fC and 0.44 fC respectively. The observed arrangement of the occupancy values follows the same order as the strip length. Therefore, the capacitance contribution to the noise due to the strip length primarily determines the noise occupancy of the modules. A small deviation of the scaling is seen for the R0 and R2 modules. The studied R0 segment has strips with a length of 32 mm, while the R2 strip length is 30.8 mm, contributing approximately 3.13 pF and 3.08 pF [125], respectively, to the total load capacitance. Hence, the noise should have followed the same scaling. However, the

R2 module has been irradiated; therefore, other noise sources, like the leakage current, increase [126], which could explain the higher noise occupancy of the R2 module compared to the R0 one.

In Figure 46b, the threshold is corrected for all modules, except for the 2019 LS and R0 as the occupancy saturated at 10^{-2}, such that at threshold zero, the noise occupancy is 50%. The correction is required to set a baseline for the calibration, which is otherwise impossible to obtain. Figure 46b shows the occupancy with the threshold correction applied, offering more insights into the occupancy behavior. The dependency of the logarithm of the noise occupancy with the threshold square is linear, and the system noise charge can be calculated as $q_n = \sqrt{-1/(2 \cdot m)}$, where m is the slope of the linear relationship. The calculated noise is summarized in Table 3. As for the median charge, the errors are obtained as the square root of the diagonal elements of the estimated fit covariance matrix.

Table 3.: Module electronic noise from a measurement of noise occupancy as a function of the threshold.

Module	Noise Charge [fC]	Noise ENC [e$^-$]
LS 2019	0.145 ± 0.002	918 ± 12.0
R0 2019	0.110 ± 0.003	687 ± 19.0
Irrad. SS 2021	0.093 ± 0.003	580 ± 19.0
Irrad. SS 2022	0.088 ± 0.001	549 ± 6.00
Irrad. R2 2022	0.122 ± 0.002	761 ± 12.0

The measured noise is slightly higher than the nominal observed values reported in [127]. However, this is expected as noise isolation is not optimal at the beam tests. Occupancy maps for all the investigated modules are shown in Appendix A.

5.2.3. Operational Windows

It has been mentioned that the ITk modules are required to operate at a threshold with an efficiency higher than 99% and a noise occupancy below 0.1% or equivalently with a signal-to-noise ratio larger than 10. Figure 47 presents the noise occupancy and efficiency as a function of the threshold for four modules analyzed in this thesis. The shaded area in the plots depicts the so-called operational window or operational threshold range, constituting the most important figure of merit for evaluating the ITk Strip detector module performance.

It is observed that regardless of the module type and irradiation status, a range of thresholds is found where the modules can be operated, satisfying the efficiency and noise occupancy requirements. For the non-irradiated modules, LS 2019 in Figure 47a and R0 2019 in Figure 47b, the threshold intervals are wider, with values of 1.42 fC

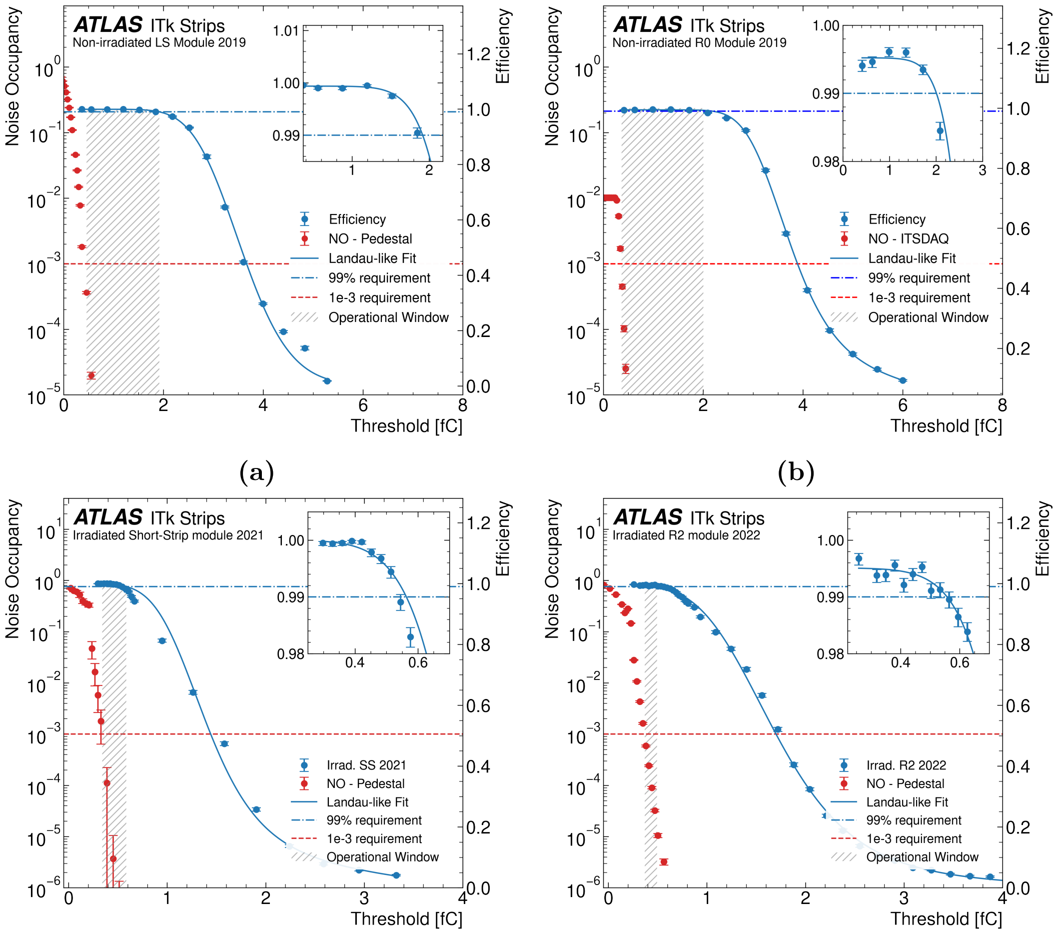

(a)

(b)

(c)

(d)

Figure 47.: Efficiency and noise occupancy as a function of the applied threshold in the channel discriminators for (a) Long Strip module 2019, (b) R0 module 2019, (c) irradiated Short Strip module 2022, and (d) irradiated R2 module 2022.

(0.46, 1.88) and 1.64 fC (0.36, 2.00) respectively. These ranges ensure the comfortable operation of the detector modules.

With the LS 2019 module serving as an example, the obtained operational window permits a value of 0.46 fC as a threshold where the module operates with an efficiency higher than 99% and a noise occupancy below 10^{-7}. These results agree with previous beam test measurements of non-irradiated modules presented in [128], where the operational threshold ranges are around 1.4 fC. Process variation during sensor production, calibration uncertainties, and baseline fluctuations because of insufficient noise isolation during the beam test measurements can cause variations in the obtained ranges for the different investigated modules. More efficiency and noise occupancy as a function of the applied threshold plots for the different analyzed positions in the modules can be found in Appendix B.

Regarding the irradiated modules, Figures 47c and 47d show the results obtained for the SS 2021 and the R2 endcap module tested in 2022. An operational threshold range is also found for the irradiated modules. In this case, the measured intervals go from 0.34 fC to 0.55 fC (0.21 fC) for the SS 2022 module and from 0.37 fC to 0.56 fC (0.19 fC) for the R2 module. These intervals are significantly smaller than the ones found for the non-irradiated modules and are of the same order as the ones found in [128] for the LS and R0 irradiated modules. For example, in [128], the MPV for an irradiated LS module built with the Star chipset and the ATLAS17LS sensor was reported to be 1.63 ± 0.05 fC (10.2 ± 0.31 ke$^-$), which is 20% larger than the MPV measured for the SS module. The SS measurement of this thesis nonetheless agrees with the projected end-of-life performance [129] when one considers that the sensor employed in the module received a neutron fluence around two times higher. Although the operating threshold range is small, the signal-to-noise ratios measured for the SS and R2 2022 modules were 18 and 15, respectively, comfortably above the required value of ten [17]. Table 4 shows the signal-to-noise ratio for the studied modules. The values are obtained by dividing the signal from Table 2 by the noise from Table 3 for each module.

Table 4.: Module signal-to-noise ratio for non-irradiated LS and R0 2019 and irradiated SS 2021, SS 2022 and R2 2022 modules. The signal-to-noise center is the value calculated using tracks traversing within 15 μm from the strip center.

Module	Signal-to-noise [fC]	Signal-to-noise Center [e$^-$]
LS 2019	24	25
R0 2019	35	36
Irrad. SS 2021	16	18
Irrad. SS 2022	18	20
Irrad. R2 2022	14	16

These results have great significance as it was shown for the first time that SS and R2 modules meet the operating specifications of the ITk Strip.

5.2.4. Efficiency uniformity

The correct ITk Strip operation needs to have uniform module performance across the entire sensor because the threshold setting is applied globally[3] to all the channels. An inhomogeneous response will lead to areas of lower hit detection efficiency, affecting the global track reconstruction capabilities of the ITk detector.

Because of the small area of the Mimosa sensors from the EUDET telescopes and to ensure high-quality beams, the effective area on the ITk Strip sensors that can be

---

[3] The trim rage procedure mentioned in Section 4.11 ensures a channel-by-channel uniform applied threshold

evaluated in a single threshold scan is relatively small. Hence, the beam is moved across different positions in the sensor. Figure 48a and 48b show efficiency maps for the non-irradiated LS and R0 2019 modules.

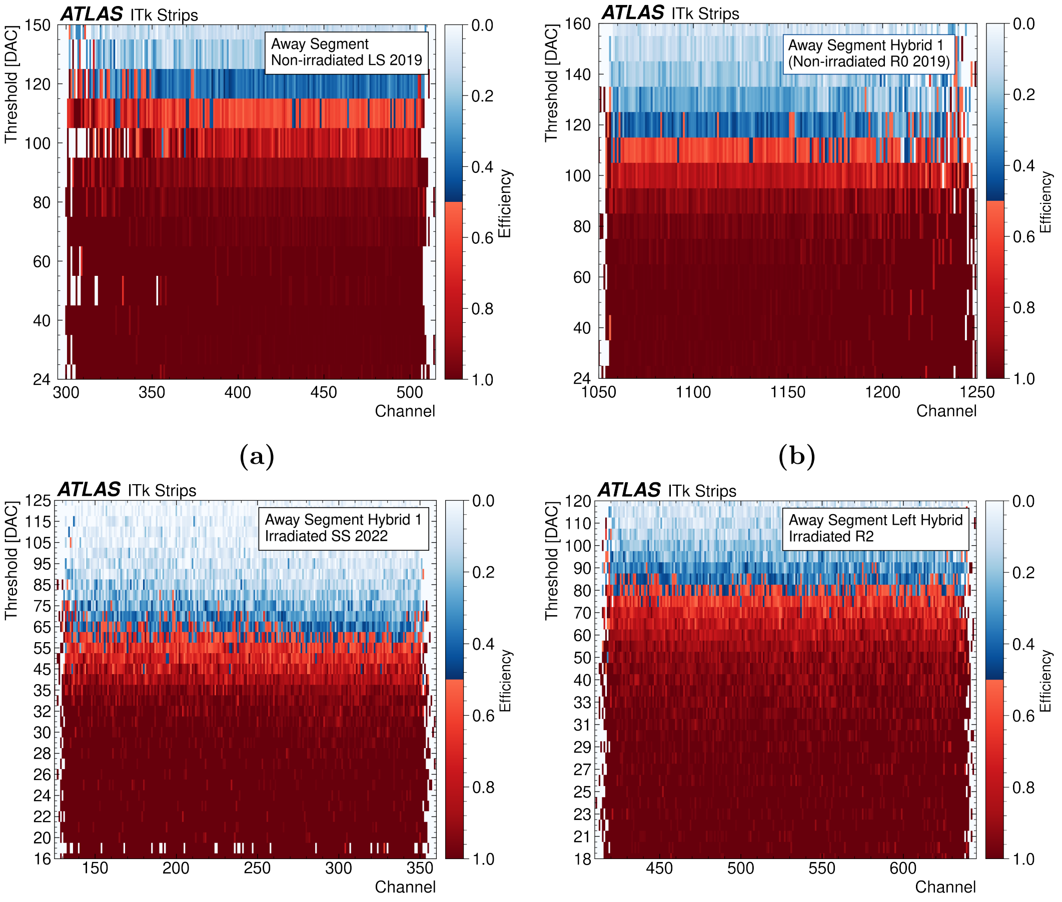

(a) **(b)**

(c) **(d)**

Figure 48.: Efficiency as a function of the applied threshold in the channel discriminators and strip number for away segments in (a) the LS 2019, (b) hybrid-1 of the R0 2019, (c) hybrid-1 in the irradiated SS 2022 and (d) the left hybrid in the irradiated R2 module.

The threshold setting in the plot is given in DAC units instead of fC because of the different calibration parameters of the two ABCStar chips mapped. It can be seen that the response across all the channels shows good uniformity over the entire threshold range for the positions investigated.

The same type of study was performed for the irradiated modules. Figures 48c and 48d show the efficiency map obtained for two positions on the SS and R2 2022 irradiated modules, respectively. One can observe that the efficiency drops with the threshold homogeneously across all the investigated channels for both modules. Towards the end of the strip intervals, some non-uniformities are visible, related to statistical fluctuations, because fewer events are recorded at the edge of the beam. The noise occupancy response for all the channels of the studied modules is shown in Appendix A and offers further evidence of the good uniformity observed in the response of the detector modules.

The in-strip efficiency for different thresholds is shown in Figure 49 for four different modules. The values in the x-axis are given in units of strip pitch and extend over two strip centers for the barrel and three for the endcap. The strip centers are located at 0.5 and 1.5 for the LS and SS modules, while for the endcap modules, the centers are located at 0, 1.0, and 2.0. The efficiency remains above 99% for low thresholds, and no spatial dependency within the strip in the non-irradiated and irradiated cases is observed. In the case of larger thresholds, the efficiency is the highest within the strip center and decreases towards the edge of the strip pitch.

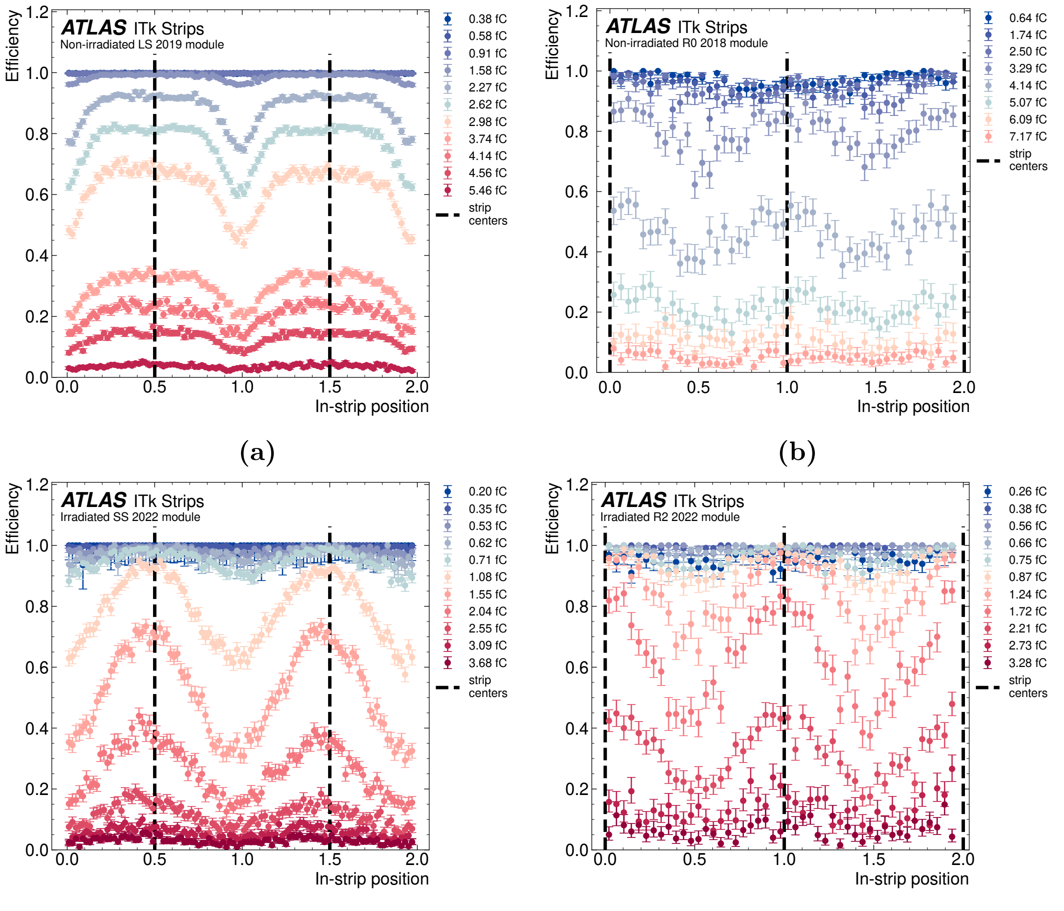

(a)

(b)

(c)

(d)

Figure 49.: Efficiency as a function of the position within the strip for (a) non-irradiated LS 2019, (b) non-irradiated R0 2019, (c) irradiated SS 2022, and (d) irradiated R2 2022 modules. The x-axis is given in units of the strip pitch such that 0.5 and 1.5 represent the strip center for the LS and SS modules. For the R0 and R2, the centers of the strips are located at 0, 1, and 2.

This behavior is expected because more charge sharing occurs close to the edges of the strip pitch. Consequently, the induced charge in one strip shrinks, likely remaining below the threshold and leading to efficiency loss. There are two main differences between non-irradiated and irradiated modules. The first one, already observed in the efficiency versus threshold plots in Figure 47, is that the efficiency drop begins at lower thresholds for irradiated modules. The second difference is that in the irradiated modules, the fraction of the strip pitch that remains with high efficiency is reduced for a given threshold level, evidencing an enhancement of charge division mechanisms after irradiation.

The ITk Strip sensors have several rows of strips separated by a small gap with no strip implants. This area is known as the inter-segment region. Figure 50 shows a study of the efficiency in the inter-segment region for the LS module as a function of the track position.

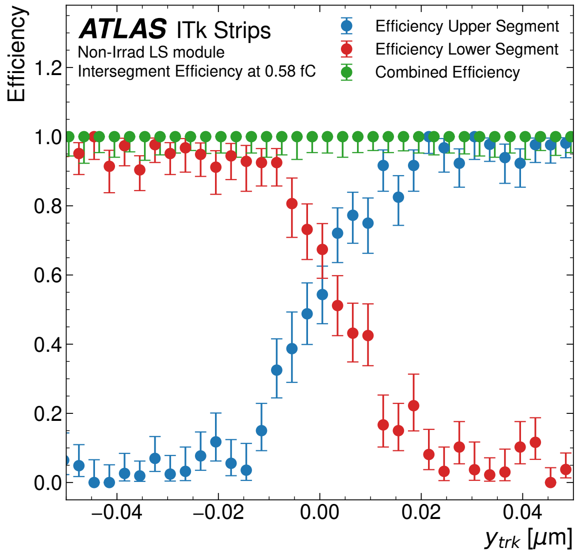

Figure 50.: Inter-segment efficiency (green) for the non-irradiated Long Strip module for a 0.58 fC threshold as a function of the track position. The efficiency for each of the individual strip rows (red and blue) decreases towards the edge of the strips. Combining the hits of both segments leads to recovering the efficiency loss, and, in the inter-segment region, the efficiency conforms with the 99% requirement.

The track position is taken from the reconstructed telescope tracks, and no DUT hit information is included. The latter removes any possible DUT bias in determining the track intercept. It is observed that the efficiencies of the upper (blue) and lower (red) segments drop considerably toward the edge of the strips, but they are not immediately zero. The gradual efficiency drop demonstrates that the sensor collects charge beyond the strip termination.

The inter-segment efficiency is then obtained by combining hits from both segments on an event-by-event basis using a logical OR. For example, when a particle goes close to one of the segments, only that segment records a hit and is counted in the combination. Similarly, a particle going through the middle of the inter-segment region will likely be counted in both segments, which will also be counted for the combined efficiency. The most important result is that the combined efficiency of the two segments is higher than 99%. This analysis shows that the hit reconstruction efficiency requirement is also satisfied in the inter-segment region.

5.3. Position Resolution and Cluster Size

5.3.1. Resolution

As discussed in Section 4.6, the spatial resolution is estimated as the RMS value of the unbiased residual distributions. The shape of these distributions, and hence, the position resolution, depends on several factors, including the sensor characteristics, such as the pitch and the readout employed, and experimental conditions, like the particle incidence angle and the operating threshold.

As stated, the ITk Strip modules use a binary readout and are tested at a bias voltage between 300 and 500 V. The sensors are designed to have a strip pitch as close as possible to 75.5 µm to simplify the bonding to the ABCStar ASICs [54]. The latter led to a constant pitch of 75.5 µm for the ITk Strip barrel sensors and a variable between 70 to 80 µm for the endcap ones. In the case of the endcap sensors, the angular pitch is kept constant for each sensor ring, and their values are approximately between 85 and 194 µrad. Hence, the expected resolutions given by Equation 26 are between 21 and 23 µm. The studies presented kept the incidence angle perpendicular to the sensor plane. Under these conditions, for a given module, the resolution should only depend on the applied threshold and the irradiation fluence received by the module. However, as a consequence of using binary readout, the residual distributions also depend on the incidence point in the sensor and, hence, on the cluster size.

The unbiased spatial residual distributions of the modules are shown in Figure 51 for thresholds between 0.8 and 3.8 fC. A box-shaped distribution dominates the residuals in non-irradiated modules, Figures 51a and 51b. It is observed that the plateau width is approximately equal to the strip pitch. The plateau of the distributions does not reach the entire pitch because tracks passing close to the strip edge will likely generate a hit with cluster size two, which has a smaller residual. The contribution of hits with cluster size two is observed as a small peak superimposed on the plateau. The corresponding resolutions, given by the σ values in the plots, match within 1% the expected resolutions for the non-irradiate modules and within 5% for the irradiated ones.

The distributions for irradiated modules exhibit a more Gaussian-like shape as cross-talk increases with irradiation [130], and consequently, the probability of multiple strip

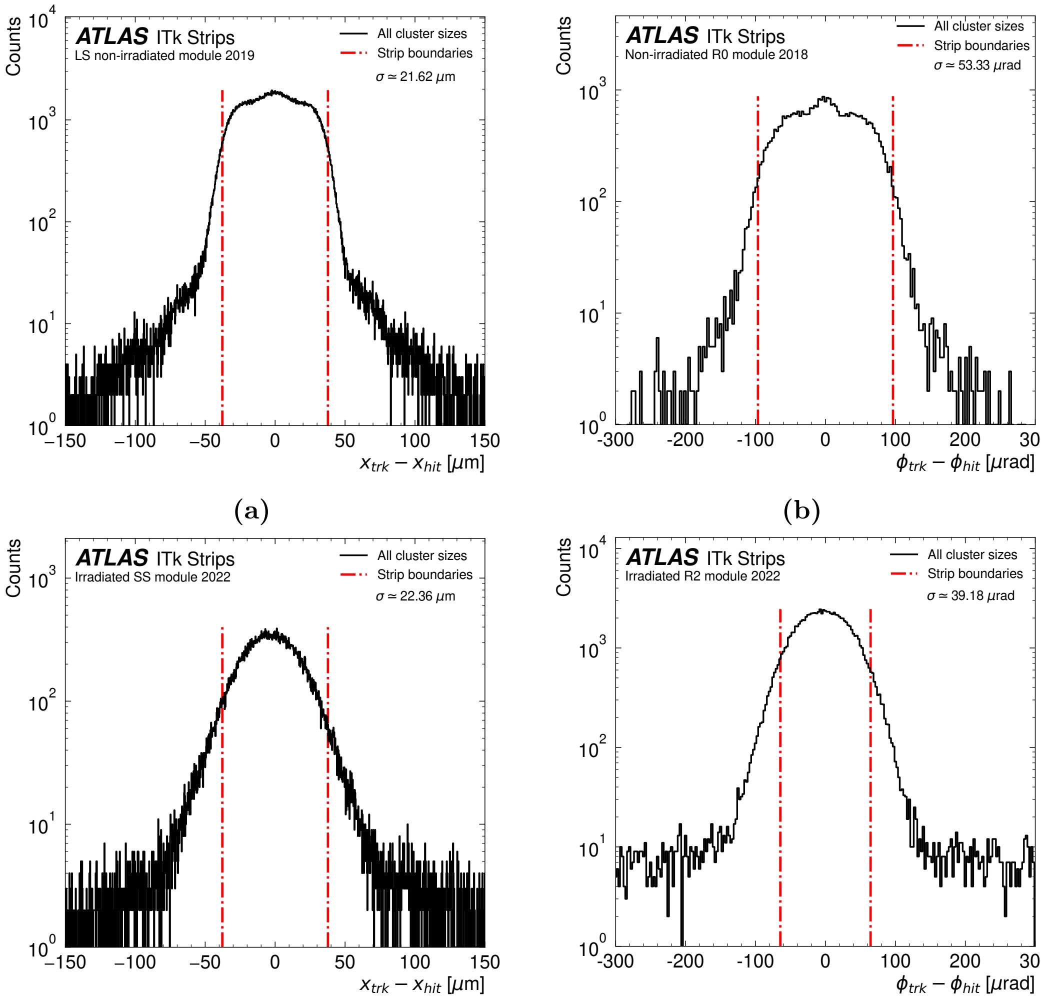

(a) (b)

(c) (d)

Figure 51.: Unbiased spatial residual distributions for thresholds between 0.8 and 3.8 fC for (a) non-irradiated LS 2019, (b) non-irradiated R0 2018, (c) irradiated SS 2022 and (d) irradiated R2 2022 modules.

clusters also increases. It is also observed that long tails expand to the distribution core's left and right. Events with a large difference between the extrapolated track incident point and the associated cluster give the tails. As expected, there are more events with large residuals in the irradiated modules than in the non-irradiated due to the higher noise and cluster sizes.

5.3.2. Contribution from Different Cluster Sizes

Residual Distributions

The behavior observed in Figure 51 can be explained when the different cluster size contributions are investigated. Figure 52 displays the spatial residuals for different cluster sizes and three threshold levels for the non-irradiated LS module 2019. The distributions are scaled to the maximum number of entries of the *All Cluster Sizes*, shown in red in the figures. This scaling permits easy comparison of the shapes of the distributions and the fraction of events that each cluster size contributes to the total counts.

It is observed that the single-strip clusters are responsible for the box-like shape seen in the plots of Figure 51 and dominate the shape of the residual distribution for all threshold levels. As explained in Section 3.6.1, this shape corresponds to the expectation for the digital readout as the true position of the track intercept point is limited by the pixel pitch, and 1-strip hits comprise the largest fraction of events for all thresholds.

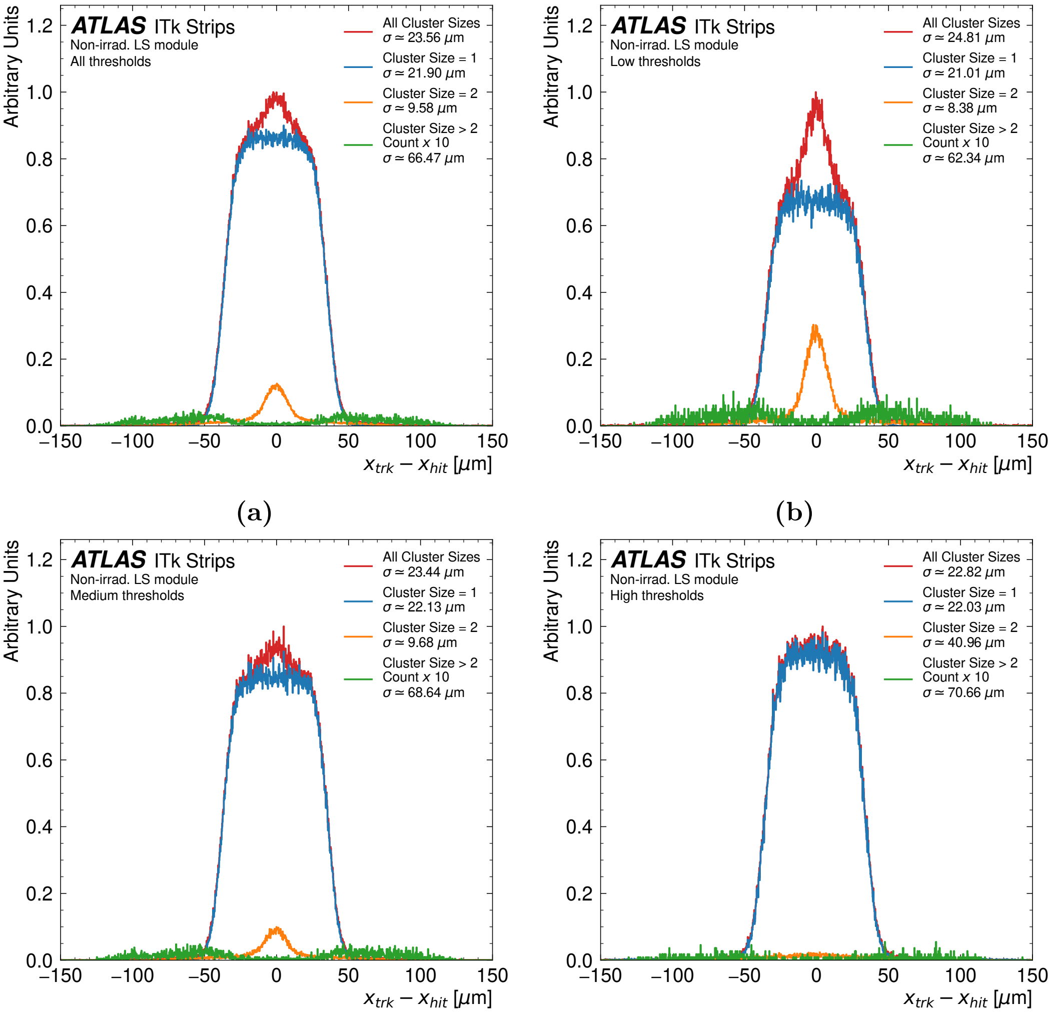

(a) **(b)** **(c)** **(d)**

Figure 52.: Unbiased spatial residual distributions for different cluster sizes at (a) all threshold, (b) low thresholds, (c) medium thresholds, and (d) high thresholds for a non-irradiated LS.

With binary readout and perpendicular incidence, hits with cluster size two are mostly produced by tracks passing close to the strip edges. When a particle traverses the inter-strip region, the charge is shared between the two strips, and if the collected charge is larger than the set threshold, a hit with cluster size two is registered. The position of those hits, given by the geometrical center of the cluster, is located exactly in between the two strips. The error of the measurement position, i.e., the residual, is much smaller than half the strip pitch because the hit position reported by the sensor is, on average, closer to the true track incident point. Therefore, the residual distribution for 2-strip clusters presents a pronounced peak centered around zero.

The distribution width has a complex dependence on the distribution of the charge carrier cloud, the charge-sharing mechanisms within the sensor, and the amount of cross-talk. As the occurrence of hits with cluster size two depends on having two strips above the threshold, the number of clusters with size two strongly depends on the threshold setting. Hence, at low thresholds, Figure 52b the number of 2-strip clusters represents a larger fraction of the total events. As expected, the fraction decreases appreciably at high thresholds, Figure 52c, while at very high thresholds, there are practically no hits with cluster size two, as seen in Figure 52d.

Furthermore, 2-strip clusters partially contribute to the tails, as seen in Figure 53. Such events can be produced by delta electrons, cross-talk, or noise, predominantly at low thresholds.

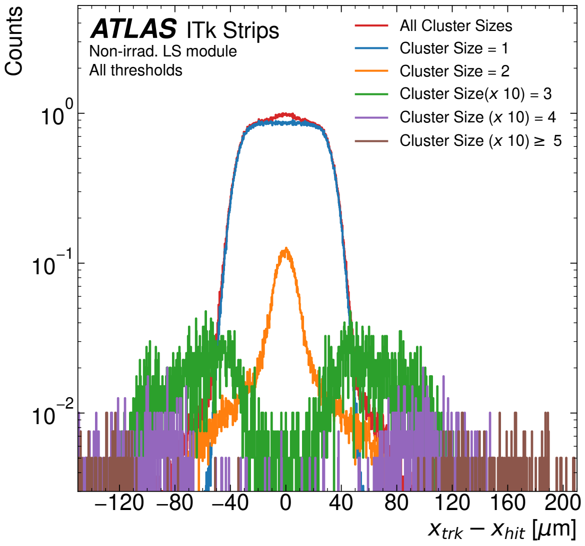

Figure 53.: Residual distribution for different cluster sizes for the non-irradiated LS 2019 module. The influence of large cluster sizes on creating the tails of the distribution is noticeable.

Larger clusters contribute primarily to the tails. In practice, 3-strips clusters are responsible for the tails, with a smaller contribution for larger clusters as seen in

Figure 53, and almost no larger clusters occur. Delta electrons and cross-talk are the primary sources of hits with 3-strips clusters. From geometrical considerations, the difference between the cluster center and the track incidence point will be approximately the strip pitch in the case of delta electrons. In the case of cross-talk, the cluster center should lie within the cluster central strip; hence, the residual is lower than the pitch.

Hits with cluster sizes of four and more than five strips should almost exclusively arise from delta electrons, and their residual distributions are offset by 1.5 and 2 times the strip pitch. In addition, common mode noise, especially in the beam test conditions, where noise isolation is hard to achieve, can lead to hits with large cluster sizes. Figure 53 suggests that delta electrons are, for the most part, responsible for the outliers observed in the residual distributions of Figure 51. Finally, a small probability exists that a track is reconstructed incorrectly but still passes the selection cuts. This can also lead to an outlier in the residuals.

After irradiation, there is a general decrease in the charge collection efficiency [52, 131]. Irradiation generates trapping centers, during which the created electrons and holes can be trapped in their drift toward the strips. If the charge carriers are not de-trapped within the readout integration time, part of the deposited charge is not collected, leading to an overall decrease in efficiency as shown in Figures 47c and 47d.

In addition, there is an increase in charge sharing, which is responsible for two distinctive differences observed in the residual distributions of Figure 54 compared to the non-irradiate case.

The distribution for 1-strip hits no longer presents a plateau as the strip loses efficiency toward the edges. After irradiation, charge coupling between neighbor strips, i.e., cross-talk, increases due to several factors, including the decrease of the inter-strip resistance and the increase of the inter-strip capacitance owing to the introduction of interface charges in the Si-SiO_2 [130, 132, 133]. Therefore, when a track passes close to the strip edge in an irradiated sensor, a larger fraction of the collected charge is shared with the neighbor strip. However, these tracks have a lower probability of producing a hit because the overall collected charge is smaller, and thus, it is less likely to be above the threshold. Therefore, the residual distribution for hits with cluster size one becomes more Gaussian-like because the DUT resolution is of the same order as the telescope resolution for smaller pitches.

The second feature is observed in the distribution for hits with cluster size two, Figures 54a and 54b. It can be seen the cluster size two distribution is considerably wider concerning the non-irradiated case. The cause of the wider residual is also linked to the increase in charge sharing. However, in this case, the charge sharing causes the inter-strip region to widen with the consequent increase of the RMS of the distribution. As for the non-irradiated case, for medium (Figure 54c) and high

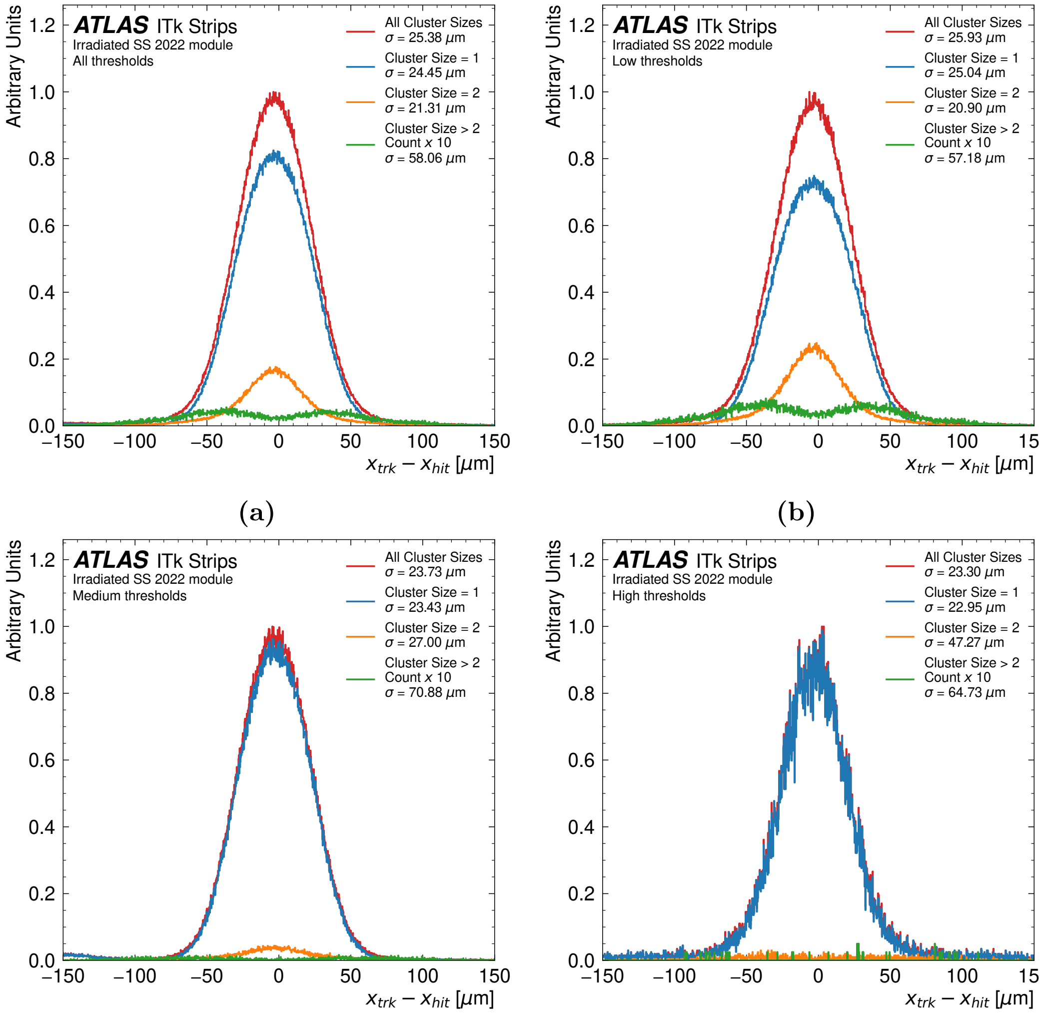

(a) (b) (c) (d)

Figure 54.: Unbiased spatial residual distributions for different cluster sizes at (a) all threshold, (b) low thresholds, (c) medium thresholds, and (d) high thresholds for an irradiated SS module.

(Figure 54d) thresholds, the number of hits with cluster sizes larger than one decreases substantially.

Resolution dependence on threshold

The unbiased residual distribution, including all cluster sizes, is utilized to estimate the position resolution of the modules. The resolution is obtained as the RMS of the distributions in the range between -65 to 65 µm, and the telescope resolution is then subtracted in quadrature to obtain the DUT resolution. Figure 55 shows the calculated resolution as a function of the applied threshold and different cluster size contributions. Using a GBL Track Resolution Calculator [134], the telescope resolution is estimated based on the distance between the telescope planes and their radiation length. For the setups used in 2019 and 2022, the telescope pointing resolution at the DUT position yielded 6 and 9 µm.

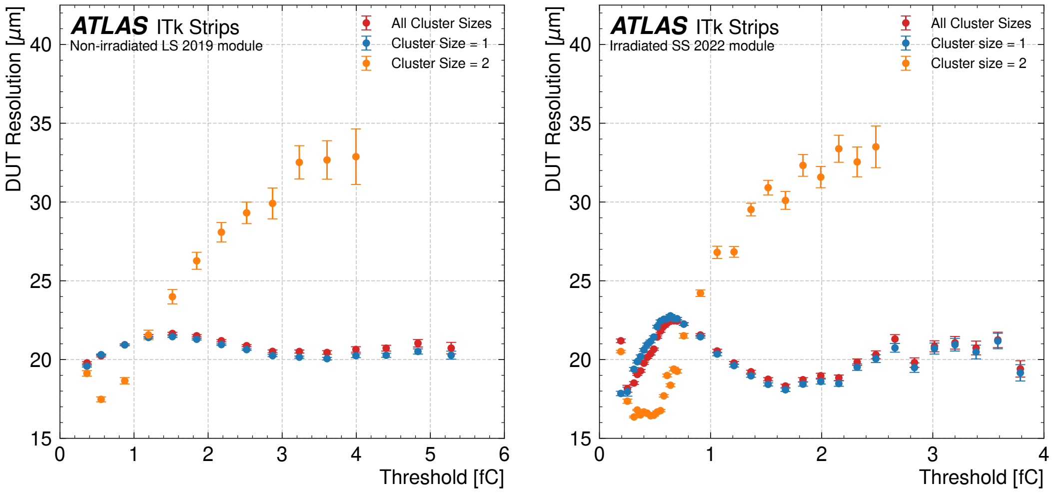

(a)

(b)

Figure 55.: Unbiased residual RMS as a function of the applied threshold and different cluster sizes for (a) non-irradiated LS 2019 module and (b) irradiated SS 2022 module.

Figure 55 can be considered a summary of the behavior described earlier for the change of the residual distributions for different cluster sizes and thresholds; see Figure 52.

The overall RMS, given by *All Cluster Sizes* in the plots, is predominantly determined by the behavior of the RMS obtained from the cluster size one residual for irradiated and non-irradiated modules. An exception is only visible for the irradiated modules at a very low threshold, where the noise occupancy is exceptionally high. At this threshold, below 0.15 fC for the studied module, noise increases the probability of having associated hits with cluster sizes larger than one. Consequently, the hit position is pulled away from the true entrance point, and the RMS becomes larger. The effect is not visible for the RMS of the distribution of single cluster hits because, in this threshold range, these hits are only produced when the particle traverses the strip at a small distance from the strip center.

The RMS of the 1-strip hits increases for higher thresholds, up to 1.19 fC (50 DAC) for the non-irradiated and up to 0.75 fC for the irradiated one. This decrease in resolution is expected, and it is due to the effective increase of the strip pitch up to roughly its geometrical width.

For even higher thresholds, the RMS resolution improves again. This increase in resolution is also expected because, for larger thresholds, only tracks passing at a short distance from the strip center generate a hit. In this case, the charge shared with the neighbor strip when the particle passes closer to the strip edge is not large enough to produce a hit. Again, the effect is equivalent to reducing the strip pitch and creates a bias of the detected hits towards the strip center, which remains efficient at higher thresholds.

Yet, the resolution does not increase much more at even higher thresholds. While the effective pitch gets smaller with the threshold increase, the lower efficiency biases the residuals towards large energy depositions from the long tail of the Landau, mainly by delta electrons, which leads to larger clusters and worse resolutions. The overall observed dependency agrees with the studies shown in [135].

The 2-cluster RMS presents a minimum at approximately 0.56 fC (30 DAC), and the values are smaller, up to 1.19 fC (50 DAC), than the corresponding one for the distribution with cluster size one. As discussed above, the RMS increases at even lower thresholds, below 0.4 fC, due to higher noise occupancy.

For higher thresholds, the RMS of the cluster size two distribution worsens because the probability of having hits with cluster size two decreases, rendering flat distributions with extremely low statistics. The latter point is evident in the large error bars at high thresholds.

Hits with cluster sizes larger than two only contribute to the tails of the overall residual, and because of its double peak structure, the RMS values are not meaningful. In addition, the error bars of the reported RMS values are exceptionally large because of the low number of hits with cluster sizes larger than two. Therefore, reporting the RMS values of the residual distribution for hits with cluster sizes larger than two is omitted.

5.3.3. Mean Cluster Size

Figure 56a shows the average cluster size as a function of the threshold for non-irradiated and irradiated ITk Strip modules investigated during the different beam test campaigns. For thresholds larger than 2 fC (12.5 ke^-), all modules show approximately the same average cluster size value. For lower thresholds, in the range between 0.5 fC (3.12 ke^-) and 2 fC, non-irradiated modules present larger clusters than the irradiated ones, directly related to the modulation of the strip width described in the previous section.

At even lower thresholds, the curves show some evidence that the average cluster size increases more rapidly for the irradiated modules than for the non-irradiated ones. However, the non-irradiated module was not investigated at the same lower threshold values as the irradiated ones. Therefore, these results must be interpreted cautiously, and more studies are required to understand the behavior of the average cluster size at low thresholds in irradiated and non-irradiated modules.

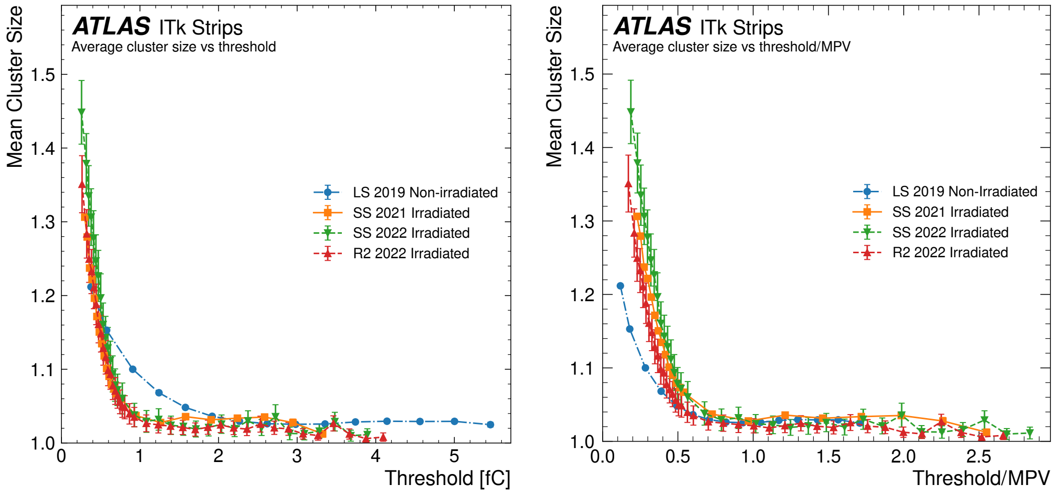

(a) **(b)**

Figure 56.: Average cluster size as a function of (a) the threshold in fC and (b) as a function of the threshold scale by the MPV for different ATLAS ITk modules.

Figure 56b offers a more insightful glance at the average cluster size dependence with the threshold. The plots show the mean cluster size as a function of the threshold divided by the MPV of each module. In this way, the x-axis gives the fraction of the charge shared. It is observed that for a threshold/MPV below 0.5 fC, the irradiated modules display larger cluster sizes than the non-irradiated ones. The latter, again, suggests an enhancement of charge sharing in irradiated modules. It is worth mentioning that charge sharing refers to any mechanism causing a charge to be induced in the neighbor strips, including cross-talk.

The average cluster size as a function of the track intercept within the strip also offers evidence of the increase in charge sharing for the irradiated modules. Figure 57 displays the mean cluster size as a function of the position within the strip for the non-irradiated LS 2019 and the irradiated SS 2022 modules.

For both modules, one can observe that the average cluster size increases when the particles traverse the strip close to its edges. However, this behavior depends on the threshold, which modulates at which distance from the strip center the charge shared is enough to generate hits with cluster sizes larger than one. In the non-irradiated case, Figure 57a, at the lowest threshold of 0.38 fC, particles with incidence point beyond ± 20 μm from the strip center are likely to generate larger cluster sizes. At higher thresholds, this distance increases and only tracks a few microns away from the strip edge can produce hits with larger cluster sizes.

The same behavior is observed for irradiated modules, Figure 57b. Yet, a few differences are noticeable. At lower thresholds, it can be seen that the charge is shared even for tracks going nearly through the center of the strip. In contrast to the

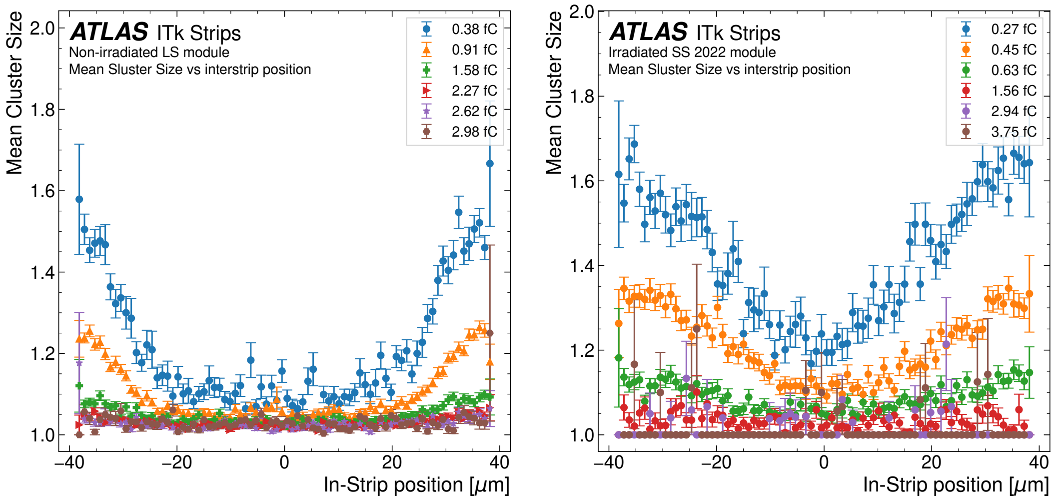

(a) **(b)**

Figure 57.: In-strip mean cluster size for (a) non-irradiated LS 2019 and (b) irradiated SS 2022 modules. In the x-axis, zero corresponds to the center of the strip while the strip edges are located at ± 37.75 µm.

non-irradiated modules, tracks passing further away from the strip edge can create hits with larger cluster sizes at higher thresholds. The mean cluster size behavior within the strip supports the conclusions about the charge-sharing enhancement after irradiation in the ITk Strip modules.

5.3.4. Space Points

Strip detectors have the major disadvantage of providing only 1-dimensional hit position information. This negative characteristic is circumvented using stereo layers, as briefly mentioned in Section 3.6.1. A stereo layer consists of a second module, rotated by a small angle to reduce the probability of the so-called "ghost hits" [61]. Ghost hits arise when two layers of strips are employed at high hit densities. Since each hit generates an x- and a y-coordinate, n tracks will generate n^2 combinations from which $n^2 - n$ are fake ("ghosts") as shown in Figure 58. The tracking algorithm can eliminate most ghost hits at low track densities by rejecting the ones incompatible with track candidates. However, at high track densities, the task becomes challenging, and therefore, a small angle between layers reduces the total area where the ghost hits can be generated, simplifying the task for the pattern recognition algorithm.

Given a single stereo layer with pitch p, the so-called space points are reconstructed by employing hit information from each layer. If two strips are hit, the true position can be located anywhere inside a rhomboid area created by the overlap of the two strips, as depicted in Figure 59.

The shape is described by a triangular probability function extending ± $p \cdot \sec \frac{\varphi_s}{2}$

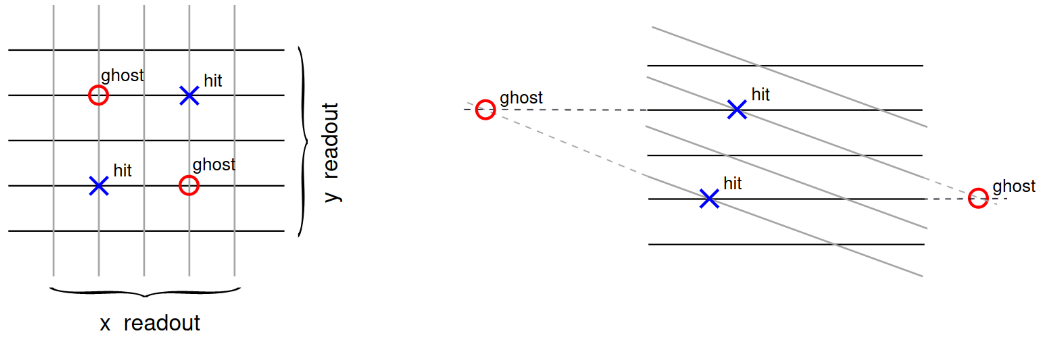

Figure 58.: Schematic showing the appearance of false hits or "ghosts" (left) when two strip layers crossed at 90° and the reduction of fake hits when a small stereo angle (right) is employed [61].

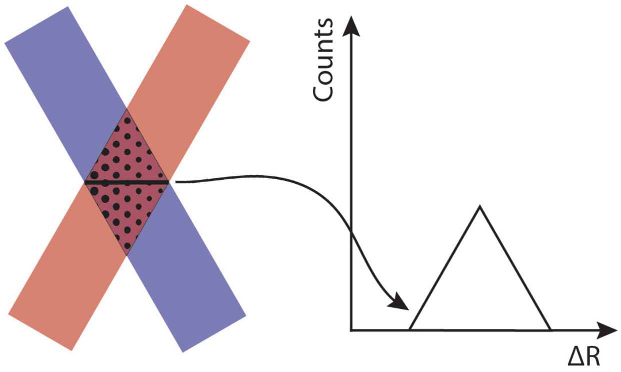

Figure 59.: Schematic depicting the rhomboid area formed by overlapping two strips. The true position of the hit can lie at any point within the patterned area, leading to a triangular residual distribution whose width corresponds to the length of the highlighted rhombus diagonal.

where p is the pitch of the sensor layers, and φ_s is the stereo angle. Thus, the expected resolution along the strips, also known as the R-resolution, is given by the squared root of the distribution variance

$$\frac{p}{\sqrt{24} \cdot \sin \frac{\varphi_s}{2}}. \tag{41}$$

A more detailed discussion on the measurements with stereo layers can be found in [136].

As part of the ITk module prototyping phase, a double-sided R0 module was built to resemble the structure of an entire petal on a smaller scale. The module was studied at the DESY beam test facility, and the space point reconstruction using the two R0 layers was carried out. The space points reconstruction was investigated for the outermost strip segment of the R0 module, where the strip pitch is 78.5 µm. For this pitch and the nominal stereo angle at this position of 36 mrad used by the ITk

Strip layer, the expected R-resolution is given by Equation 41 and an expected value of $\simeq 890$ µm.

Because the module was assembled manually, the physical value of the stereo angle can differ from the target value if the relative alignment of the sensors is imperfect during the building process. To determine the exact stereo angle, the two modules were allowed to rotate independently during the alignment step during the reconstruction of the beam test data. The angle between the two line segments defined by the space point and the origin of coordinates of the strips on each module was calculated and used to estimate the stereo angle.

Figure 60a shows the distribution of stereo angles determined by the described method. The radial geometry of the sensors is responsible for having a distribution of angles rather than a single value. The mean value of approximately 31 mrad indicates that the manual building process introduced an unintentional relative rotation of the sensors.

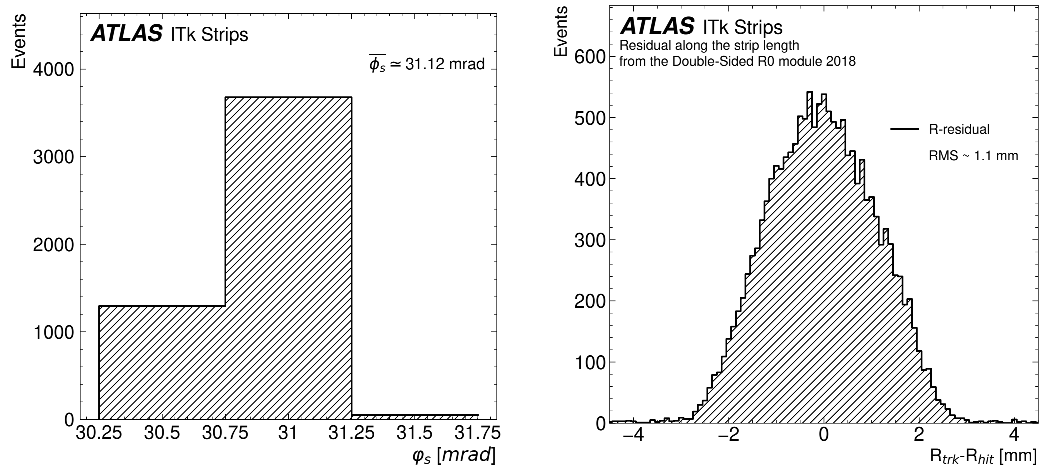

(a) **(b)**

Figure 60.: Stereo angle distribution (a) and unbiased spatial residual distribution along the strip length (b) obtained from the reconstruction of the space points from the DSR0 module.

The residual distribution along the strip length obtained from the space points reconstruction is shown in Figure 60b. The RMS of the residual in Figure 60b is 24% larger than the predicted value for the outermost segment of the module when the modules are perfectly aligned. Using Equation 41 and the physical stereo angle of 31 mrad implemented in the module, the expected value for the R-resolution becomes 1.03 mm. The obtained RMS of 1.10 mm is in good agreement with the expectation within 7%. Small DUT misalignment and uncertainties in the track position can easily account for the 7% discrepancy. Therefore, the reconstruction and analysis of the space point from the DSR0 module prove that the stereo geometry of the ITk

Strip endcap sensors delivers the expected resolution given by Equation 41. The results also give confidence that modules used in the experiment, which are assembled using highly accurate automatic processes and tools, will deliver the required position resolution along the strip length.

Chapter 6

Passive CMOS Strip Sensors

The 2020 Update European Strategy for Particle Physics has established as a high priority the ambition to operate a proton-proton collider at a center of mass energy of 100 TeV with an electron-positron collider as the first stage [137]. Independently of which accelerator is built, the increase in energy and luminosity will consequently increase the silicon area of the tracking systems installed in the detectors by a factor between 1.6 to 2 [138]. A bigger detector implies more readout channels, electronic components, power consumption, and cooling. Therefore, future detector technologies must satisfy stringent requirements and, in the case of hadron-hadron colliders, they must be extremely radiation hard.

The Complementary Metal Oxide Semiconductor (CMOS) technology has been employed successfully in Integrated Circuits (IC) and image sensors. The CMOS technology offers low power consumption and high integration of the sensing volume and the readout electronics, potentialities that in particle physics applications can be further exploited. In addition, CMOS processes are standard for large foundries, meaning that large detectors with many individual sensors can be more cost-effective fabricated by utilizing these commercial production lines. These features make the CMOS technology a prominent candidate to populate the tracking systems of future experiments.

6.1. Overview of CMOS Technology in Particle Detectors

CMOS uses two complementary MOS transitions, a PMOS (p-substrate) and an NMOS (n-substrate) transition. A MOS transition is the interface between metal, oxide, and semiconductor. The MOS structure is the fundamental building block of the most common type of field-effect transistor, the MOSFET. The combination of millions of MOSFETs in the same substrate allows the construction of highly complex circuits based on the complementary logic of PMOS and NMOS.

CMOS circuits use less power than bipolar junction and field-effect transistors because the MOS transistors draw high currents only during switching, while at the steady state, the power consumption is mainly due to the leakage current. Another essential feature is that CMOS standard processes use only a few micrometers of the silicon wafer, opening the door to thinner sensors as the readout can be implemented within the sensing volume.

In particle physics, the technology has been used uniquely for pixel detectors, either hybrid pixel sensors or monolithic active pixel sensors (MAPS). In hybrid pixel sensors, shown in Figure 61, the sensing volume and the readout electronics are independent and connected via bump-bonding. This technology is widely used in the ATLAS and CMS trackers and allows the readout electronics and sensing volume to be developed separately. However, bump-boding is an expensive and complicated process, which reduces the yield of the assembly process. Additionally, having more material layers could affect the tracking system's precision.

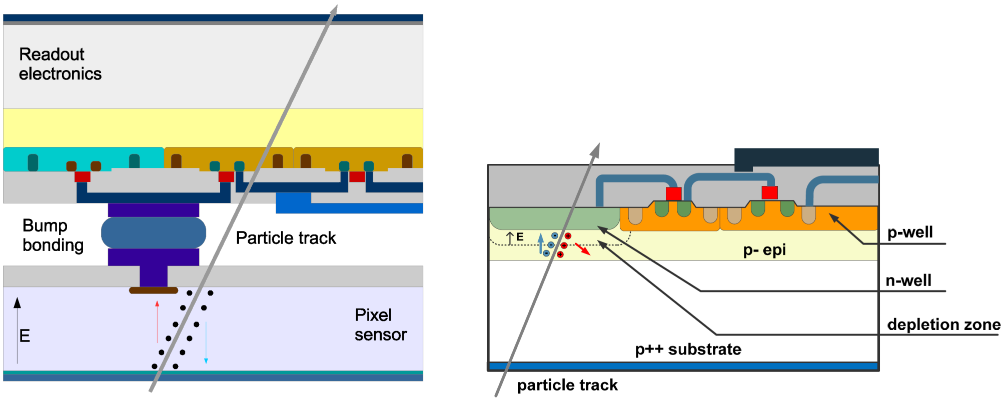

(a) (b)

Figure 61.: Cross-section of CMOS pixel detector concepts employed at the LHC experiments [139]. (a) Typical hybrid pixel detector using a fully depleted silicon planar sensor and (b) classical Monolithic-Active Pixel Sensor (MAPS) with epitaxial layer as sensing volume and n-well as the charge collecting electrode.

On the other hand, MAPS integrates the readout electronics and the sensing volume in a single layer, as shown in Figure 61. MAPS brings less material in the tracker, faster production, and a large cost reduction by using commercially available CMOS processes.

Even though CMOS sensors have been employed in particle detectors, particularly in the LHC experiments, the technology still faces a few challenges. Detector development needs to optimize the sensing volume, achieve faster time resolutions and higher radiation tolerance, and obtain larger sensor areas while using CMOS standard recipes to fully profit from the technology advantages.

6.2. CMOS Reticle Size

As mentioned in the previous section, one of the challenges of the CMOS technology for particle detectors is obtaining large-area sensors.

The problem with large sensor areas resides in the masks or reticles employed in the standard lithography process in CMOS foundries. Chip production does not require wafer-size reticles, but it does require high-resolution masks. CMOS reticles have features scaled up by 4x, 5x, and even 10x, as there are limitations in how small features can be transferred to the masks. Consequently, the maximum reticle size in a standard CMOS process is limited to approximately 5 cm^2 [140].

To obtain larger areas, a process called stitching [141] must be employed. The process works by dividing the sensor structure into smaller blocks of the size of the available reticle dimensions, as seen in Figure 62. Then, in the lithography step, the entire structure is created by exposing the different blocks. The same reticle can be exposed several times, obtaining areas larger than the reticle.

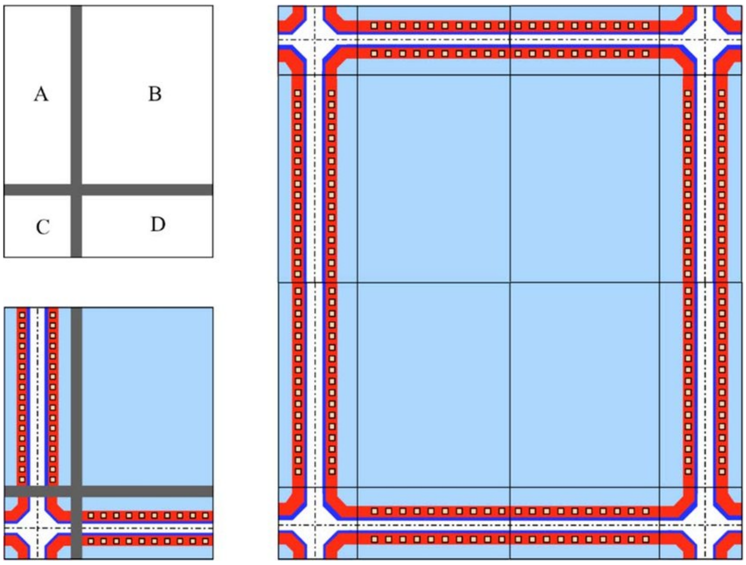

Figure 62.: Example of a CMOS image sensor reticle subdivided into different areas (A) left and right edge, (B) sensor, (C) corners, (D) top and bottom edges [142].

The work presented in this thesis investigates the feasibility of CMOS strip sensors with up to five reticles stitched together for particle tracking applications.

6.3. LFoundry CMOS Strip Sensors

The sensors investigated were produced by LFoundry in the 150 nm CMOS process [143] on an 8-inch float zone p-type silicon wafer with a resistivity of 3-5 kΩcm. The final target thickness is (150 ± 5) µm. There are two sensor sizes, 1×2.2 cm^2, referred to as the short sensor, and 1×4.2 cm^2, referred to as the long sensor. Both sizes exceed the reticle size of approximately 1×1 cm^2 and have been processed by stepping the different reticles over the wafer along the strip length. As a result, the strip lengths are 2.1 and 4.1 cm for the short and long sensors, respectively. Different reticles are used for generating edges and corners. In the short sensor, three stitches are used, and the long sensor uses five stitches in total.

Two different sensor designs were investigated. The first design is similar to the ATLAS ITk endcap design [54] and is called *Regular*. The second design has a low-dose n-well below the strip with two different sizes, 30 µm and 55 µm and are named *Low-dose 30* (LD30) and *Low-dose 55* (LD55), respectively. Moreover, the designs differ in the width of the strip implant and n-well, as observed in Figure 63.

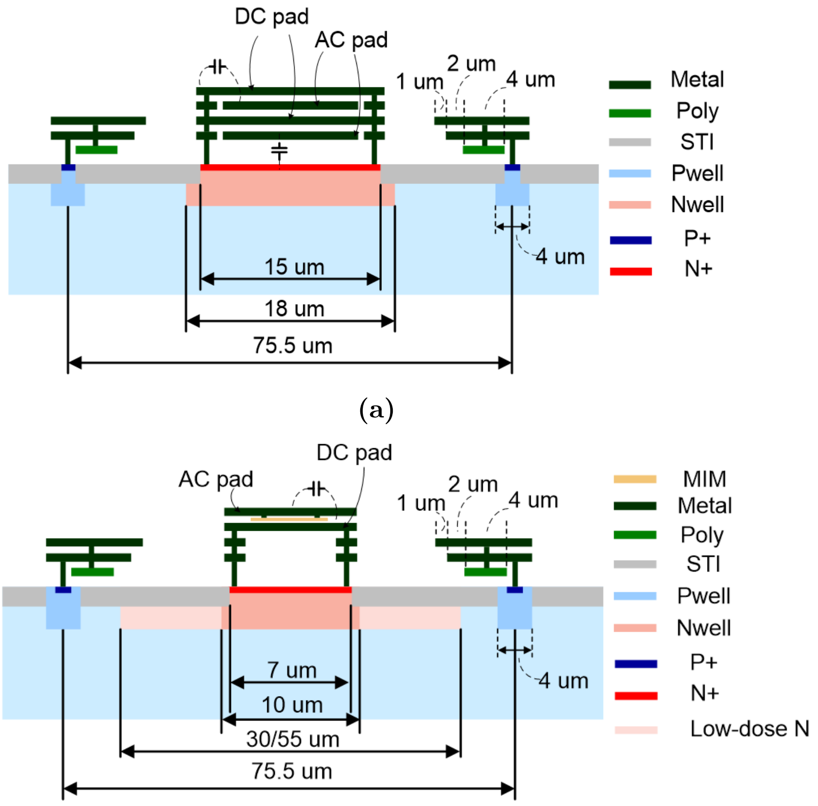

(a)

(b)

Figure 63.: Schematics of the CMOS strip designs under study (a) Regular design and (b) low dose design [144].

The strips are biased using polysilicon resistors connected to a bias ring. Five guard rings and a laser annealed p$^+$ implant in the backside provide high voltage stability and guarantee good contact with the backside metallization. Two sensor batches were studied. The first batch did not have backside metallization, and the p$^+$ implant dose was one order lower than for the second batch.

Both designs have an AC and a DC pad on the strip implant, with minor geometrical differences. In the Regular design, four metal layers are used, and the AC pads are coupled with a capacitor. The Low-dose designs use a metal-insulator-metal (MIM) capacitor, which separates the AC and DC pad metal layers, and therefore, the AC signal is coupled using a CMOS capacitor instead of the standard SiO_2 layer employed in silicon sensors. The implemented p-well structure, which includes a metallization, is the same for all designs. It is important to note that the LD30 and LD55 implementations cannot be biased independently, which impacts the electrical characterization.

The two designs are implemented in the same sensor, as shown in Figure 64, where the position of each design and the stitched lines are depicted. Each sensor is divided into two sets of 40 strips, with a pitch of 75.5 µm. The Regular design has 40 strips, and the Low-dose ones have 20 strips each. The Low-dose designs cannot be biased independently as they share the same bias ring. As a consequence, the electrical characterization does not distinguish between LD30 and LD55. The regular design has its own bias ring and therefore, it can be biased independently.

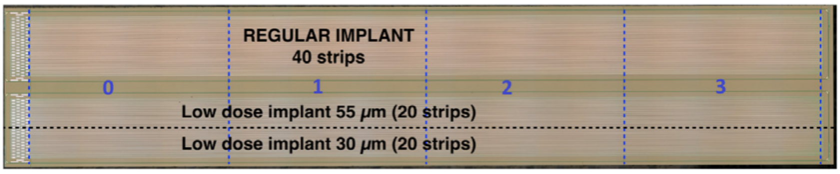

Figure 64.: A “long” CMOS sensor image. The blue dashed lines show the stitching positions. The stitched areas investigated are labeled 0–3 [144].

In addition, it can be seen that the sensors do not use the CMOS capability to incorporate the readout electronics into the same substrate. Hence, the strip sensors under study here are passive and must be read out using external electronics, as for the strips and hybrid pixel detectors.

As indicated earlier, radiation hardness is a critical feature to asses for devices fabricated using the CMOS technology. Consequently, a set of sensors were irradiated at the TRIGA research reactor in Ljubljana [121, 122] with neutron irradiation to fluences ranging from 1×10^{14} to 1×10^{15} n_{eq}/cm^2.

6.4. Electrical Characterization

All sensors were characterized at room temperature in a Karl Suess probe station [145]. For IV measurements, a needle was placed on the bias ring while the high voltage was applied to the backplane. In the case of sensors from the first batch, without backplane metallization, the high voltage is applied via a seal ring connected to the sensor backplane. For the sensors in the second batch, the high voltage is applied directly to the metallization at the backplane. A Keithley 237 [146] is employed as a power supply. The CV measurements are performed with a Keysight High Precision 4284A LCR meter [147]. All measurements are performed in a cleanroom at 23°C and humidity below 35%. Figure 65 shows the IV characteristic of the sensors for the first and second batches.

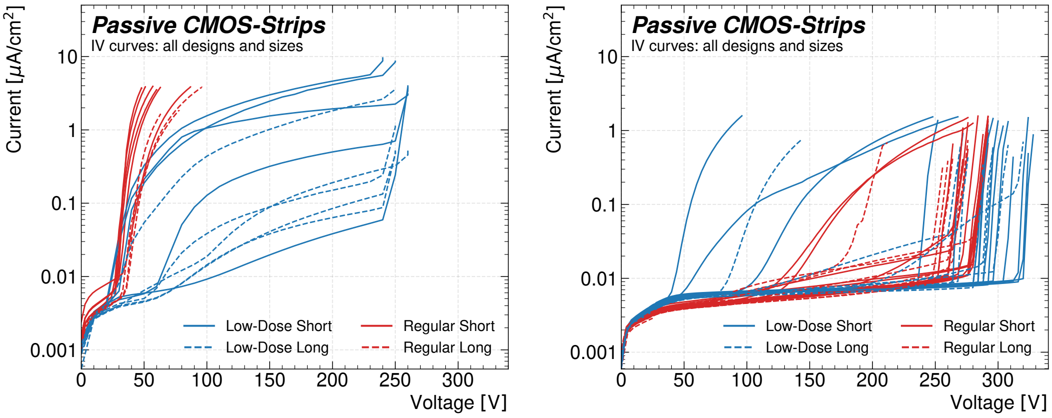

(a) (b)

Figure 65.: Current-voltage characteristic of the passive CMOS strip sensors from (a) the first and (b) second batch for all the designs. There is no distinction between the Low-dose 30 and Low-dose 55 designs, as it is not possible to bias them independently. The total leakage current is normalized to the sensor area.

Sensors from the first batch showed an early breakdown, before 250 V, and a high leakage current. In addition, the IV curves displayed a broad spread in the measured current and breakdown voltage, pointing out a high sensitivity to handling and external factors such as humidity. A group of sensors exhibited even earlier breakdown, before 40 V, the bias voltage for which full depletion is expected. This early breakdown indicated a termination problem when the electric field lines reached the sensor backplane. The problem is attributed to a lower doping concentration in the p^+ implant in the backside than the required to shield the electric field and the lack of a metallization layer [144].

The second batch of sensors showed a much better uniformity in the IV curves and a much lower leakage current than the first batch. Most sensors break down beyond 250 V, and only a few exhibit breakdowns at lower voltages, which can be associated with the expected variations in the manufacturing process. The better stability, lower leakage current, and larger breakdown voltage can be directly related to the increase by one order of magnitude in the p^+ backside implant dose and the deposition of a metal layer.

The sensor's CV characteristics, measured at 1kHz, are shown in Figure 66 for the first and second batch. The full depletion voltage ranges between 30 and 35 V. The Low-dose design shows a slightly higher full depletion voltage than the Regular one.

The higher full depletion voltage in the Low-dose design agrees with the expectation coming from Equation 13, considering that the Low-dose design's effective doping concentration is slightly higher than in the Regular design because of the extra n-well.

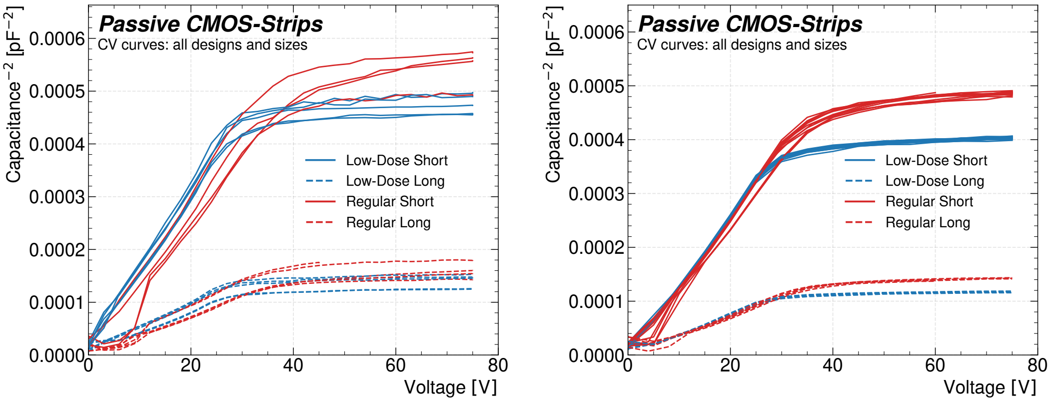

(a) **(b)**

Figure 66.: Capacitance-voltage characteristic of the passive CMOS strip sensors from (a) the first and (b) second batch for all the designs. There is no distinction between the Low-dose 30 and Low-dose 55 designs because it is not possible to bias them independently.

The short sensor bulk capacitance is approximately 50 pF, while the measured value for the long sensors is roughly 100 pF. The factor of two agrees with the area factor between the two sensor sizes. The Low-dose design bulk capacitance is slightly higher, which is also related to the extra n-well. Finally, the CV curves of the first batch show the non-uniform behavior observed in the IV curves. In contrast, as for the IV curves, the second batch sensors present a more stable behavior than the first batch.

To measure the inter-strip capacitance of the sensors, three strips were connected, one signal strip and its two neighbors. The inter-strip capacitance is a critical parameter to evaluate the collected charge in the beta source and test beam analysis. The measured values are listed in Table 5 [148].

Table 5.: Measured inter-strip capacitance values for the different CMOS strip sensor designs and sizes [148].

Design	Inter-strip capacitance [pF]
Low dose 30 (Short)	1.218 ± 0.001
Low dose 55 (Short)	2.87 ± 0.02
Regular (Short)	0.7272 ± 0.0003
Low dose 30 (Long)	2.550 ± 0.009
Low dose 55 (Long)	5.94 ± 0.02
Regular (Long)	1.522 ± 0.004

In general, it was found that the sensors are sensitive to handling, and processes like gluing onto the test boards or wire bonding can render them inoperable. In addition, the sensor showed a considerable humidity sensitivity. Thus it was necessary to store them in a dry atmosphere. Additionally, small scratches in the backplane lead to early breakdown voltages indicating that further improvements in the backplane passivation and metallization are needed in future generations.

6.5. Beta Source Measurements

Charge collection measurements are a key tool for evaluating new sensor technologies. The so-called beta setup is employed to measure the collected charge of the sensors. A schematic of the setup is shown in Figure 67, and an extensive description can be found in [149] and [150]. The sensor under investigation is placed between a ^{90}Sr source and two plastic scintillators coupled to photomultipliers operated in coincidence mode. The two scintillators have a thickness of 4 mm. The first has an area of 4 × 4 mm^2, and the second has an area of 45 × 45 mm^2.

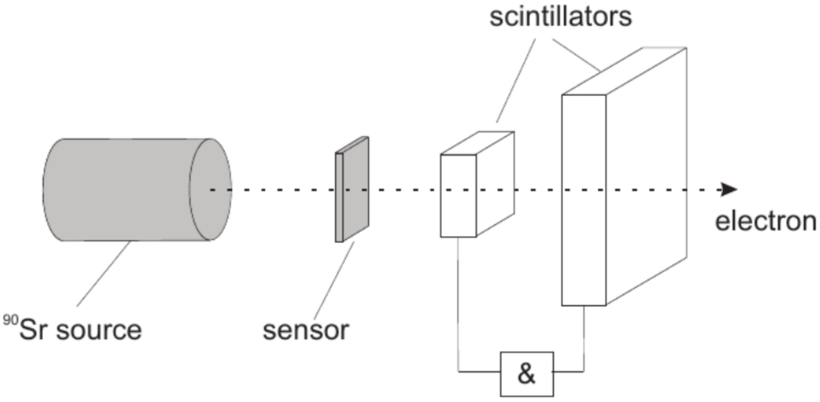

Figure 67.: Schematic of the beta source measurements [150].

The ^{90}Sr source decays via beta minus (β^-) into ^{90}Y, which then decays into ^{90}Zr also via beta minus. The energy spectrum of the first emitted electron has a maximum energy of 546.5 keV [151]. The second decay, from ^{90}Y into ^{90}Zr, has a maximum energy of 2280.7 keV [151]. The electrons from the first decay have a maximum range of roughly 2 mm [150] and get absorbed in the first scintillator. As the scintillators operate in coincidence, only electrons from the ^{90}Y decay, with a range of 10mm [150], can generate a coincidence and trigger the readout of the event. Electrons with an energy of 2 MeV, as the ones from the second decay, can be considered MIPs, see Section 3.1 and therefore, their energy deposition is approximately the same as the energy deposition of a high-energy particle, making them suitable for the test.

When an electron goes through the sensor and generates a coincidence in the scintillators, a trigger is issued and sent to the motherboard of the ALIBAVA readout system [152], which distributes the trigger signal to the daughterboard and ASICs, initiating the readout of the sensor. The motherboard is controlled by a field programmable gate array (FPGA). The entire setup is inside a commercial freezer and flushed with nitrogen to keep the relative humidity below 10%. Non-irradiated sample measurements are performed at a temperature between 13°C and 17°C. In the case of irradiated sensors, the measurements are taken at around -40°C using liquid nitrogen. A PT100 temperature sensor logs the temperature inside the freezer. The PT100 is connected to a raspberry pi microcontroller board and glued directly on the board next to the sensors.

The sensors, glued to a custom-built PCB, are connected via wire bonds to the 128-channel Beetle ASICs [153], which are glued onto the ALIBAVA daughterboard, as shown in Figure 68. The analog signals from the ASICs are sent to the motherboard outside the freezer. The motherboard controls the entire system and is connected to a computer using a USB connection. The data are stored either in a proprietary binary file or in HDF5 format [154].

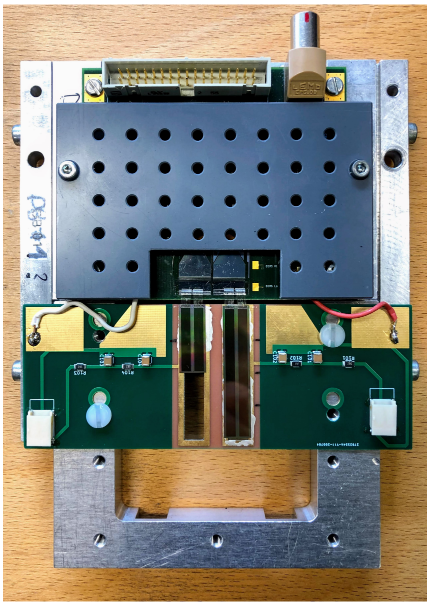

Figure 68.: ALIBAVA daughterboard with the custom PCB and short and long CMOS sensors glued and connected with wire bonds to the Beetle ASICs.

The detector response is sampled at a frequency of 40 MHz, and the output is stored in an analog pipeline. When the trigger is received, the data is sent from the Beetle to the motherboard, where they are converted to digital counts using a 10-bits analog-to-digital converter (ADC). The gain of the ASIC is temperature dependent; therefore, a calibration is required to obtain the collected charge in units with physical meaning, femtocoulombs. The calibration is obtained using a 300 μm n-in-p strip sensor at a voltage larger than the full depletion voltage. The expected total collected charge for such a sensor is 23 ke^-. A relation between the ADC counts and the collected charge can be established by measuring the ADC counts for different temperatures from which the system gain can be calculated [155].

6.5.1. Charge Collection Analysis

Before starting the charge measurements, the correct latency time must be selected to retrieve the data from the correct time bin. The triggers are randomly distributed concerning the sampling rate. Therefore, a time-to-digital converter (TDC) measures the phase of the trigger signals using a 10 MHz clock for reference. The latter allows studying the signals from the detector as a function of time, measured by the TDC.

Two types of measurements are performed for the analysis: an initial pedestal run and the data run. In the pedestal run, the motherboard generates random triggers, and the ADC counts of each channel are recorded. From this measurement, the pedestal of each value is calculated as the mean value of the signal recorded, while the root mean squared or the standard deviation of a Gaussian fit to the distribution gives the output noise of the channel. In addition, a common mode noise correction is also applied. The correction is calculated as the mean value of the ADC counts over the range of channels selected for the analysis. Channels exhibiting extraordinarily high noise are excluded from the analysis. The pedestal and common noise correction are subtracted from the data runs on a channel-by-channel basis.

Using the TDC values, a reconstruction of the signal pulse shape can be obtained indirectly in a 100 ns wide time window. A profile histogram [156] is filled with the highest signal per event for each time bin to obtain the pulse shape. The result, shown in Figure 69, resembles the output signal pulse shape after the amplification and shaping.

In the analysis, only events within a 10 ns window around the maximum of the pulse are selected. This selection impacts the total collected charge and leads to an underestimation of the signal of less than 5%. The analog readout allows knowing the deposited charge in each strip, and a clustering algorithm is employed to obtain the total collected charge. The algorithm first finds the strip with the highest signal in each event. If the signal-to-noise ratio of this strip is larger than a given threshold, the strip is selected as the seed for the following steps. A signal-to-noise ratio cut of 3.5 was used as it gave the best trade-off between collected charge and noise. The algorithm then looks for neighbor strips with a signal-to-noise ratio larger than 1.8. The distribution of the cluster's total ADC counts should follow the convolution of the Landau and Gaussian distributions; see Section 3.4. The MPV, rather than the mean value of the Landau-Gaussian distribution, is taken as the collected charge of the sensor. This choice is made because the mean of the distribution is affected by

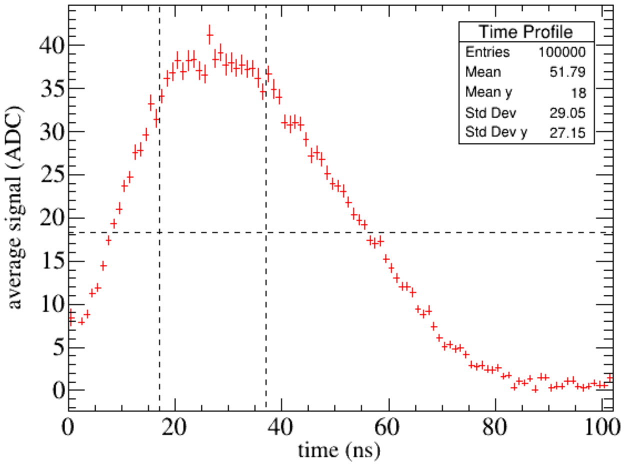

Figure 69.: Example time profile plot for the LD55 design of a non-irradiated, short sensor after full depletion. The red data points show the average signal value for every one ns wide time bin, which is populated with the signal value from the channel with the highest S/N ratio of each event. The error bars displayed are the standard deviation of the mean for each data point individually.

events with considerably higher energy depositions when, for example, delta electrons are produced.

6.6. Results for Non-irradiated Sensors

The main goal of the charge collection measurements is to evaluate the sensor performance regarding the collected charge, particularly regarding the possible effect of the stitching process. During the measurement campaign, the source is pointed at all the designs and each stitched area in turns. The stitched segments are numbered starting from zero, as displayed in Figure 64. One short and one long sensor from the first batch were tested.

For the measurements, one million triggers were taken for the runs with the radioactive source, while ten thousand triggers were recorded during the pedestal runs. The study was performed for different bias voltages, and it is expected that after full depletion, a 150 µm thick sensor should collect 11.3 ke^- for a MIP-like particle. The signal spectrum for four different voltages measured in the Regular design of a long sensor is shown in Figure 70. It is observed that the distribution shifts toward higher values with the increase of the voltage, a behavior expected because of the increase of the depleted volume in the sensor.

The distribution for 10 V is cutoff and differs the most from the rest because the depleted volume at this bias voltage is small, yielding considerably lower signals, which fall below the applied signal-to-noise ratio cut.

The collected charge as a function of the bias voltage for a short and a long sensor

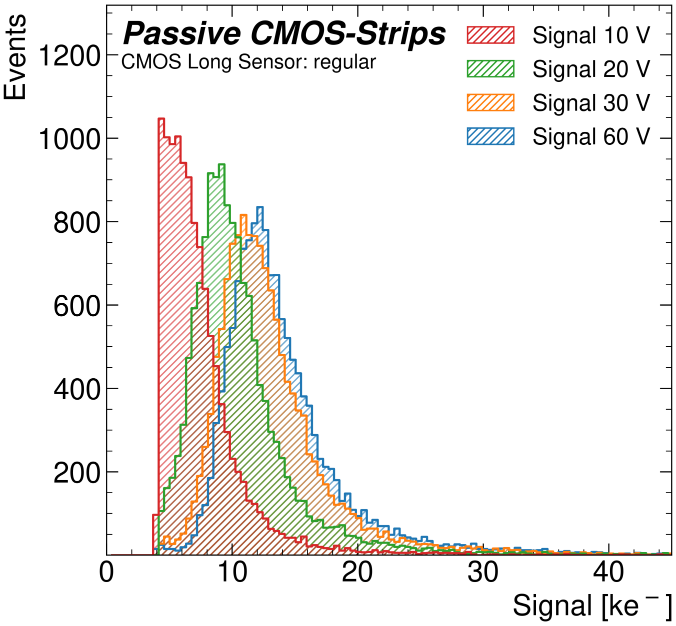

Figure 70.: Collected charge distribution for different bias voltages measured for a long sensor in the Regular design.

for the different designs and stitched areas is shown in Figure 71. The dashed black line marks the predicted collected charge. This prediction should only be taken as a reference and not as a critical parameter to assess the performance of the sensors. Fluctuation in the active thickness and systematic errors in the calibration of the readout board affect the collected charge value.

The sensors reach full depletion around 30 to 35 V, as seen from the CV measurements. After full depletion, no substantial increase in the collected charge is found. It is observed that the sensors from the second batch, shown in Figures 71c and 71d, can sustain higher bias voltages and their response is more uniform across the entire voltage range investigated. Except for the LD55 design in the short sensor from the first batch, shown in Figure 71a, there is no significant difference in the collected charge among the stitched regions. The latter is unequivocal evidence that the stitching process was successful.

Differences between the designs are observed regarding the values of the collected charge. In particular, the LD55 design consistently collects less charge than the prediction for all the sensors investigated. In addition, in the case of the short sensor from the second batch, the Regular and the LD30 designs collect slightly less charge than the prediction, which can be accounted for by small process variations such as junction depths and resistivity variation within the processed wafer. All the other designs reach the predicted collected charge within the uncertainties of the measurements.

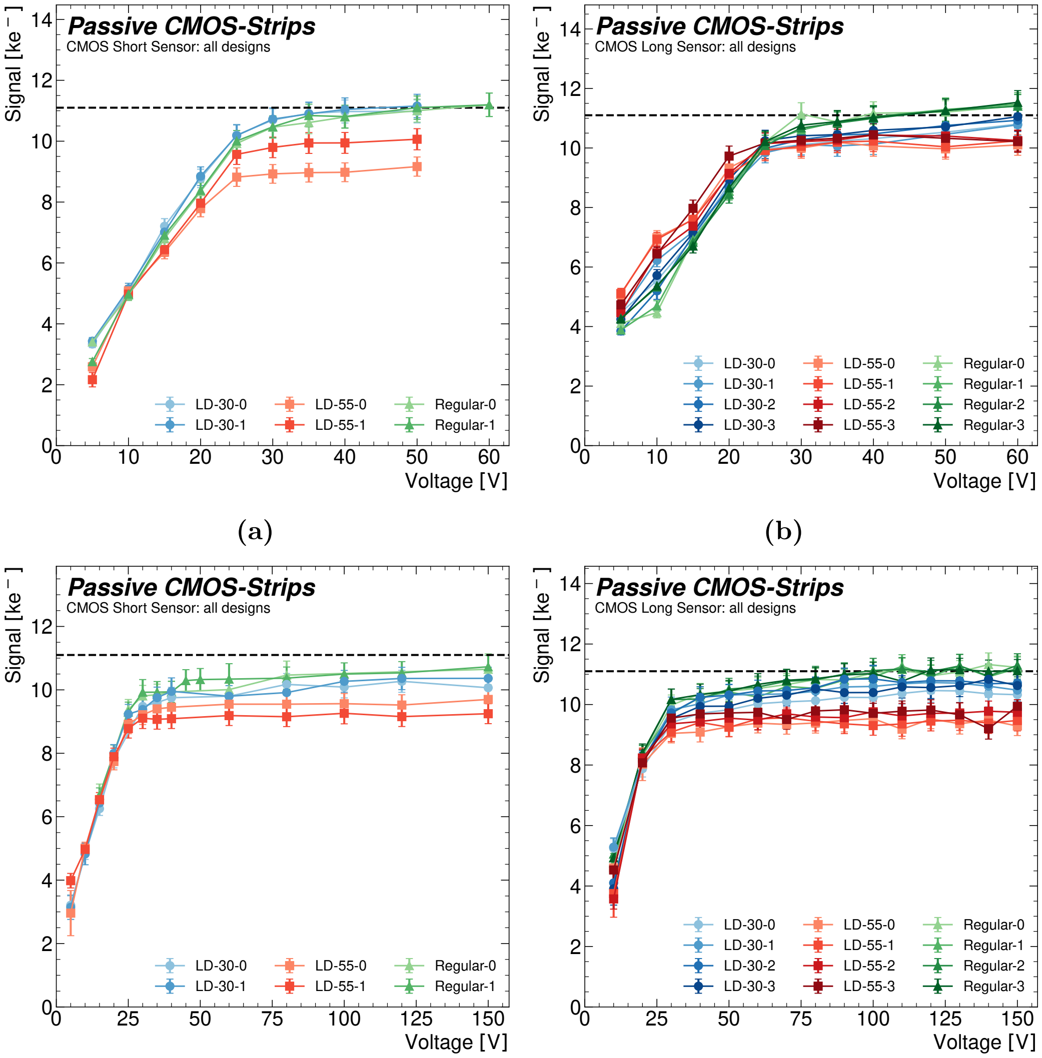

(a) (b)

(c) (d)

Figure 71.: Collected charge as a function of the bias voltage for a short (a) and (b) a long sensor from the first batch and a short (c) and a long sensor (d) from the second batch for the different designs and stitched areas. The dashed line corresponds to the expected collected charge, while LD30 and LD55 refer to the Low-dose designs. The accompanying number identifies the stitch region measured, and the lines between the data points are only a visual aid.

It is not understood why the LD55 collects less charge than the prediction. Further investigations were carried out to explain the systematic lower charge. Because of the large capacitance of this design, the influence of the shaping parameters of the Beetle chip on the collected charge was evaluated. The higher total capacitance of the LD55 design could overload the chip amplifiers, creating a ballistic deficit that could offset the ADC counts. The investigations focused on changing the Beetle chip parameters to speed up the amplifier response by delaying the peaking time of the shaping stage. The changes increased the ADC counts marginally for all the designs; hence, the low charge cannot be related to the non-optimal parameters of the Beetle chip. Another possible reason, analyzed in detail in [157, 158] using the top transient current technique [159], is the loss of charge to other strips through the n-well ring. The measurements in [157] provided strong evidence of this effect, but further research is needed for confirmation.

The output noise of the measured sensors from the first batch is displayed in Figure 72. The noise behaves as expected, decreasing with the increase of the bias voltage for all the designs. The long sensor shows higher noise values than the short sensor for all the designs, corresponding to the higher bulk capacitance value due to the longer strip length.

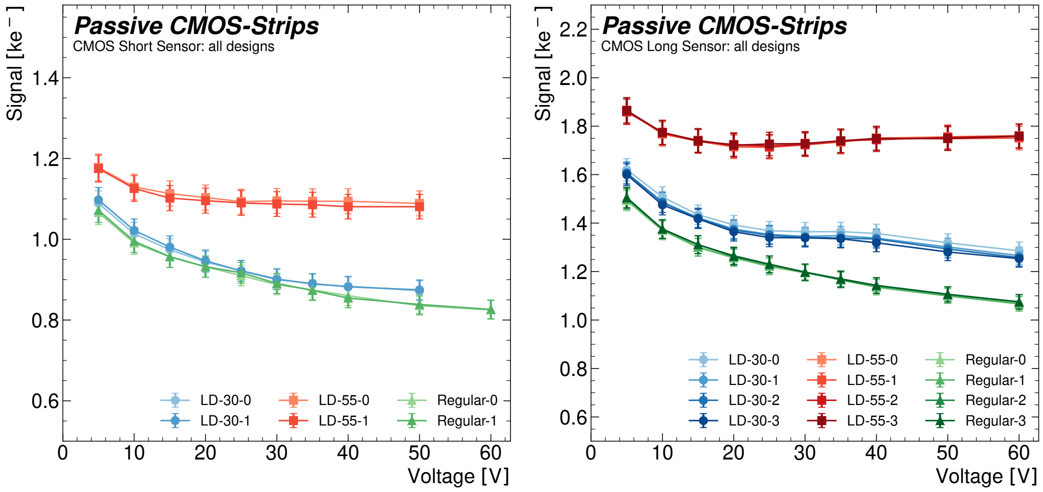

(a) (b)

Figure 72.: Output noise as a function of the bias voltage for (a) a short and (b) a long sensor from the first batch for the different designs and stitched areas. LD30 and LD55 refer to the Low-dose design. The accompanying number identifies the stitch area measured, and the lines between the data points are only a visual aid.

Moreover, the noise is higher for the Low-dose designs than the Regular ones, with the LD55 showing the highest values. These results are directly related to the design features of the sensors. The extra n-well in the low designs increases their inter-strip capacitance and hence, the total capacitance at the input of the channels front-end. Consequently, the input noise is higher. Likewise, the n-well in the LD55 is wider, making the total capacitance of this design particularly large compared to the others, and hence, the measured output noise is the highest.

6.7. Results for Irradiated Sensors

Figure 73 shows the collected charge for a short and a long sensor irradiated with reactor neutrons to a fluence of $1{\times}10^{14}$ 1 MeV $\mathrm{n_{eq}/cm^2}$ and without any annealing treatment. Both sensors exhibit an increased full depletion voltage for irradiated sensors, which is in the range of 60-90 V, and the plateau region is less stable than for the non-irradiated sensors. The increase in the full depletion voltage is expected due to increased effective doping concentration after irradiation, as explained in Section 3.5.

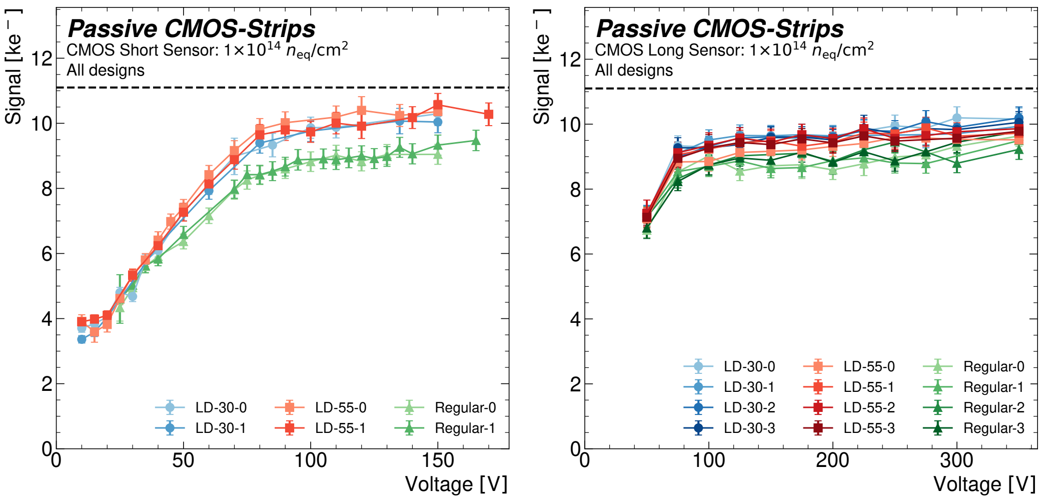

(a) **(b)**

Figure 73.: Collected charge as a function of the bias voltage for 1×10^{14} $\mathrm{n_{eq}/cm^2}$ neutron irradiated (a) short and (b) long sensors for the different designs and stitched areas. No annealing treatment was performed. The dashed line corresponds to the expected collected charge, while LD30 and LD55 refer to the Low-dose designs. The accompanying number identifies the stitch area measured, and the lines between the data points are only a visual aid.

The most interesting feature observed is that the Regular design suffers the highest decrease in performance after irradiation, collecting approximately 9.5 ke$^-$, representing a loss of 14% in charge collection compared to the non-irradiated sensors. In contrast, the collected charge of the Low-dose designs does not degrade considerably. Figure 74 shows the electric field distributions at a bias voltage of 100 V across the strip center as a function of the depth for the three non-irradiated designs obtained from Technology Computer-Aided Design (TCAD) simulations [144].

The simulations showed that the Regular design has the highest electric field near the strip implant of the three designs. However, the regular design's electric field is the lowest in the sensor bulk, making this design more susceptible to trapping after irradiation. These electric field distributions could explain the more substan-

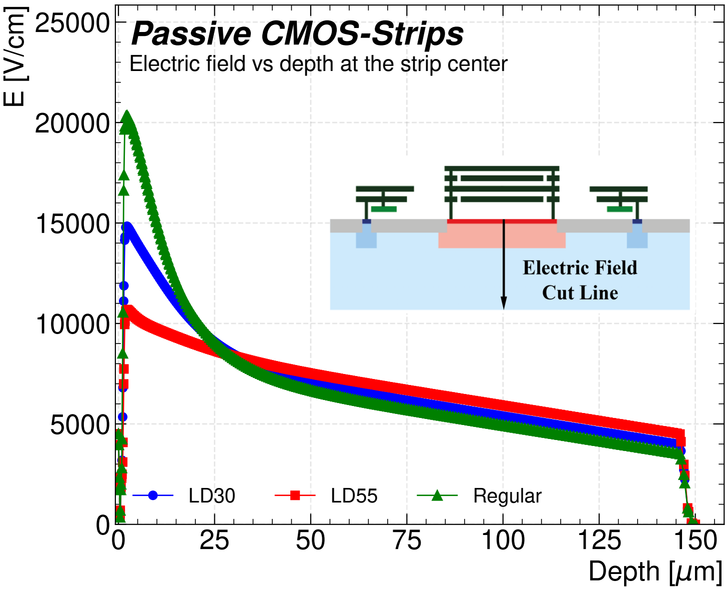

Figure 74.: Electric field cut at the center of the strip for 100 V of bias voltage for the three different geometries using TCAD simulations. The top of the sensors corresponds to the origin of the *x axis*, as the inset indicates.

tial decrease in charge collection observed for the Regular design after irradiation. Nonetheless, more detailed irradiation studies and simulations in the irradiated case would be needed.

In preparation for beam test measurements, a short and a long sensor irradiated to 1×10^{14} $\mathrm{n_{eq}/cm^2}$ were annealed at 60°C for 80 minutes, and exploratory charge collection measurements were performed. Due to time constraints, only one stitched region for each design was investigated. Figure 75 compares the collected charge for the third stitched area before and after annealing. The full depletion voltage decreases by roughly 25 V for both sensors and all the designs. This behavior is expected as this standard short-term annealing has a beneficial impact on the sensor performance. In addition, no significant decrease in charge collection or stitching deterioration after the standard treatment was found.

A more detailed study in [155] shows that annealing at 60°C for times scaled up to two years does not influence the charge collection. Sensor availability, setup issues, and time constraints did not allow measuring the charge collection before and after annealing for higher irradiation fluences in all the stitched regions. In some cases, only one measurement is available before or after annealing. However, as described and shown in [155], only the full depletion voltage changes with annealing.

Figure 76 shows a short and a long sensor irradiated to a fluence of $3{\times}10^{14}$ $\mathrm{n_{eq}/cm^2}$. The long sensor was annealed for 80 minutes at 60°C, while the short sensor did not receive any annealing treatment before the measurements. The missing stitched

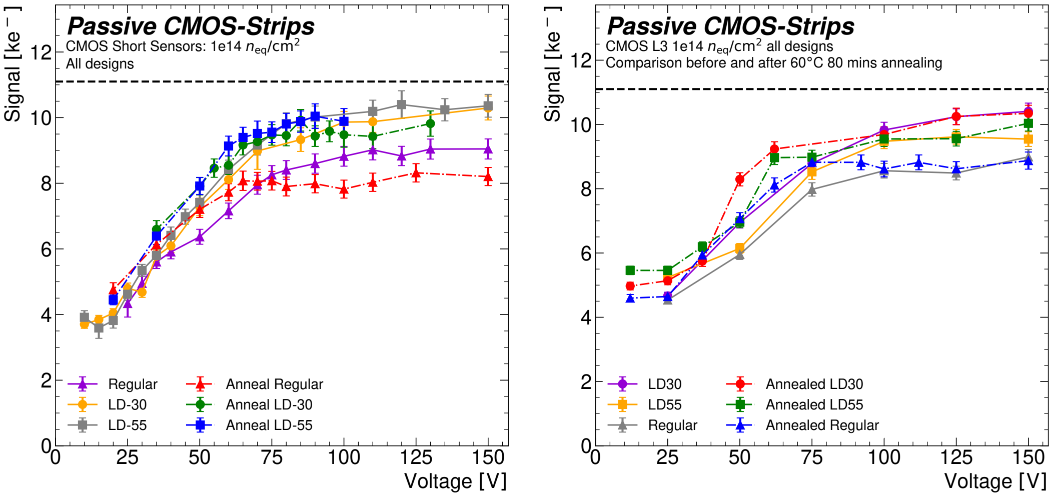

(a) **(b)**

Figure 75.: Collected charge as a function of the bias voltage for the sensors irradiated to 1×10^{14} n_{eq}/cm^2. (a) Short and (b) long sensors before and after annealing at 60°C for 80 minutes. The dashed line corresponds to the expected collected charge, while LD30 and LD55 refer to the Low-dose designs. The accompanying number identifies the stitch area measured, and the lines between the data points are only a visual aid.

region in the LD30 design of the long sensor is a consequence of a software malfunction that led to the wrong initialization of the Beetle chip configuration. The problem was only spotted during the analysis, but a remeasure of the positions was impossible because the sensor was removed from the ALIBAVA daughterboard and placed on a different setup to be used for different types of measurements. Due to the sensor's sensitivity to handling, it was not placed back on the ALIBAVA boards. As shown in Figure 76b, this risk was not worthwhile because the designs show a uniform response of all the other stitched regions.

It is observed that the full depletion voltage increased again for both sensors and all the designs, in agreement with the scaling law as a function of the irradiation fluence. The short sensor now fully depletes at approximately 250 V. The long sensor's full depletion voltage is lower due to the effect of the beneficial annealing with a value of roughly 170 V.

The charge collection across the different stitched areas for each design is uniform within the uncertainties of the measurements, as also seen for the $1{\times}10^{14}$ n_{eq}/cm^2 irradiation fluence. At $3{\times}10^{14}$ n_{eq}/cm^2, the Regular design still has a lower collected charge before full depletion compared to the other designs, which indicates that it depletes at higher voltages than the other designs. After full depletion, the differences among all the designs are marginal, except in the case of the LD30 of the short sensor, where the difference is larger for some voltages. However, the previous statements

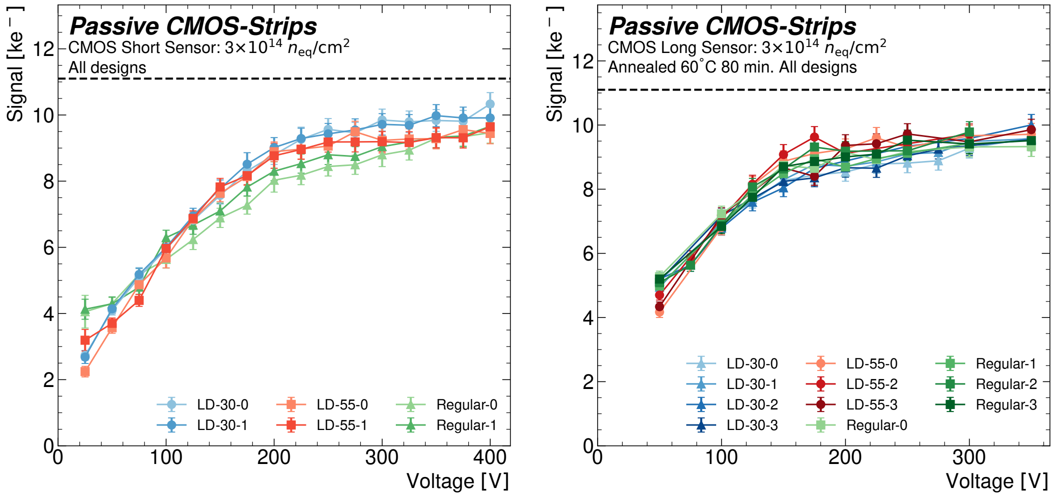

(a)

(b)

Figure 76.: Collected charge as a function of the bias voltage for the sensors irradiated to 3×10^{14} $\mathrm{n_{eq}/cm^2}$. (a) Short and (b) long sensors for the different designs and stitched areas. The long sensor was annealed at 60°C for 80 minutes. The dashed line corresponds to the expected collected charge, while LD30 and LD55 refer to the Low-dose designs. The accompanying number identifies the stitch area measured, and the lines between the data points are only a visual aid.

should not be taken as a definitive conclusion of the behavior of the designs because only two sensors were measured due to the low availability. Hence, the limited amount of data available prevents any conclusive statements.

Regarding the collected charge, in the short sensor, the Regular and LD30 designs collect approximately the same amount of charge as the sensor irradiated to 1×10^{14} $\mathrm{n_{eq}/cm^2}$. In contrast, the LD55 collects approximately 1 $\mathrm{ke^-}$ less. All the designs collect the same charge within the measurement uncertainties for the long sensor. The observed loss of scaling in the amount of collected charge in the 3×10^{14} $\mathrm{n_{eq}/cm^2}$ long sensor could be related to the effect of annealing, as the long, not annealed long sensor irradiated to 1×10^{14} $\mathrm{n_{eq}/cm^2}$, see Figure 73b, showed that the Regular design slightly underperformed.

Figure 77 shows the collected charge for a short and long sensor irradiated with neutrons to a fluence of 5 $\times10^{14}$ $\mathrm{n_{eq}/cm^2}$ and 1×10^{15} $\mathrm{n_{eq}/cm^2}$, respectively. The short sensor was not annealed, and the long one received the standard annealing treatment. No long sensor irradiated to a fluence of 5 $\times10^{14}$ $\mathrm{n_{eq}/cm^2}$ and no short sensor irradiated to a fluence of 1×10^{15} $\mathrm{n_{eq}/cm^2}$ were available. In the short sensor, shown in Figure 77a, the most obvious observation is the increase of depletion voltage to approximately 300 V, 17% more than for the 3×10^{14} $\mathrm{n_{eq}/cm^2}$ short sensor. For the long sensor, at this high irradiation fluence, the traditional[1] full depletion concept

---

[1] Traditional full depletion is understood as given by Equation 13

starts to lose meaning due to different effects. Trapping of bulk-generated carriers can modify the effective space charge, altering the linear dependence of the electric field with the depth and forming the so-called double junction configuration [160]. Nevertheless, the collected charge starts to saturate after 360-400 V, around 60 V higher than the $5{\times}10^{14}$ $\mathrm{n_{eq}/cm^2}$ short sensor.

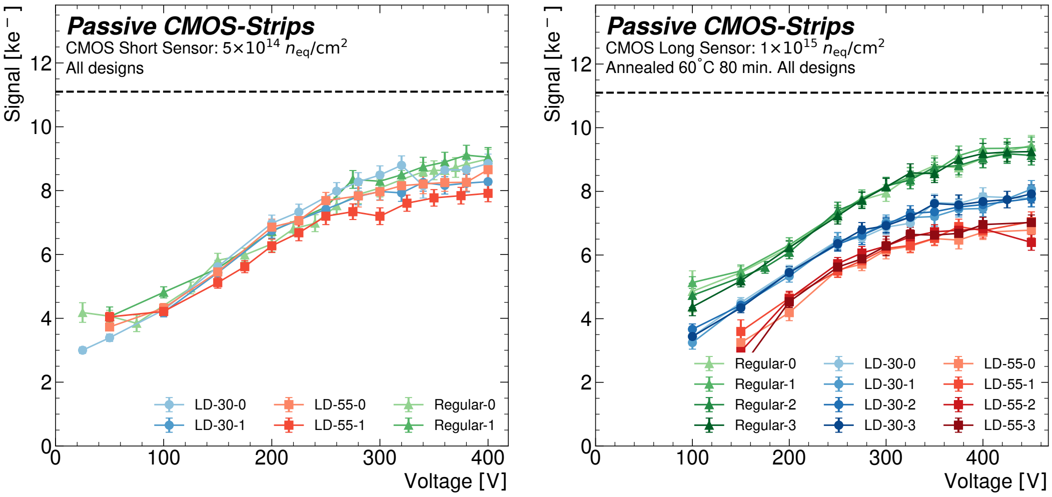

(a) (b)

Figure 77.: Collected charge as a function of the bias voltage for neutron-irradiated (a) $5{\times}10^{14}$ $\mathrm{n_{eq}/cm^2}$ short and (b) $1{\times}10^{15}$ $\mathrm{n_{eq}/cm^2}$ long sensors for the different designs and stitched areas. The dashed line corresponds to the expected collected charge, and the dashed-dotted one indicates the requirement for the collected charge in the ATLAS ITk Strip sensors after irradiation to a fluence of 1.6×10^{15} $\mathrm{n_{eq}/cm^2}$, including a safety factor of 1.5 and considering the readout electronics performance [131]. LD30 and LD55 refer to the Low-dose designs. The accompanying number identifies the stitch area measured, and the lines between the data points are only a visual aid.

The differences in the amount of collected charge among the designs are minor. However, the Regular design marginally collected more charge than the Low-dose ones. Although the differences are not significant, the observed scaling, i.e., the Regular design collecting less charge than the Low-dose one, is no longer observed after irradiation to a fluence of 5×10^{14} $\mathrm{n_{eq}/cm^2}$. Further evidence of the inversion is observed for the long sensor irradiated to a fluence of 1×10^{15} $\mathrm{n_{eq}/cm^2}$

Between the two Low-dose designs of the short sensor, there are also small differences between the two stitched areas, which could have indicated a decrease in performance in the second stitched region. Still, a degradation of the stitches of the Low-dose designs alone is unlikely as the three designs are transferred to the wafer using the same reticle and hence, lithography steps. It is reasonable to associate the differences with fluctuations in the collected charge, which is supported by the results obtained for the long sensor irradiated to 1×10^{15} $\mathrm{n_{eq}/cm^2}$.

For the long sensor, see Figure 77b, irradiated to the highest fluence investigated, it is observed that the response across all the stitched areas is uniform for all the designs. The performance of the long sensor in terms of the amount of collected charge was evaluated using as a benchmark the requirement for the ATLAS ITk Strip sensors. The ITk Strip sensors must collect 6.35 ke^{-} at a bias voltage of 500 V after irradiated to a fluence of 1.6×10^{15} $\mathrm{n_{eq}/cm^2}$, including a safety factor of 1.5 and considering the readout electronics performance [131]. Even though the most important figures of merit for tracking detectors are the hit detection efficiency and the signal-to-noise ratio, comparing the collected charge offers insights into the sensor's performance as it is directly related to the radiation tolerance of the sensor's design. It can be observed (see the dash-dotted line in Figure 77b) the CMOS sensors meet this requirement for bias voltages approximately above 300 V. Although the maximum fluence investigated was about 63% of the maximum fluence in the ITk Strip, the results are highly encouraging and allow further design optimizations.

Finally, Figure 78 summarizes the mean collected charge for sensor design and length at each fluence. The mean values are obtained by averaging the MPV of all the stitches in the sensor, while the errors are obtained using Gaussian propagation. The uncertainty in the collected charge is again calculated using Gaussian error propagation, while the fluence is known with 10% precision [161].

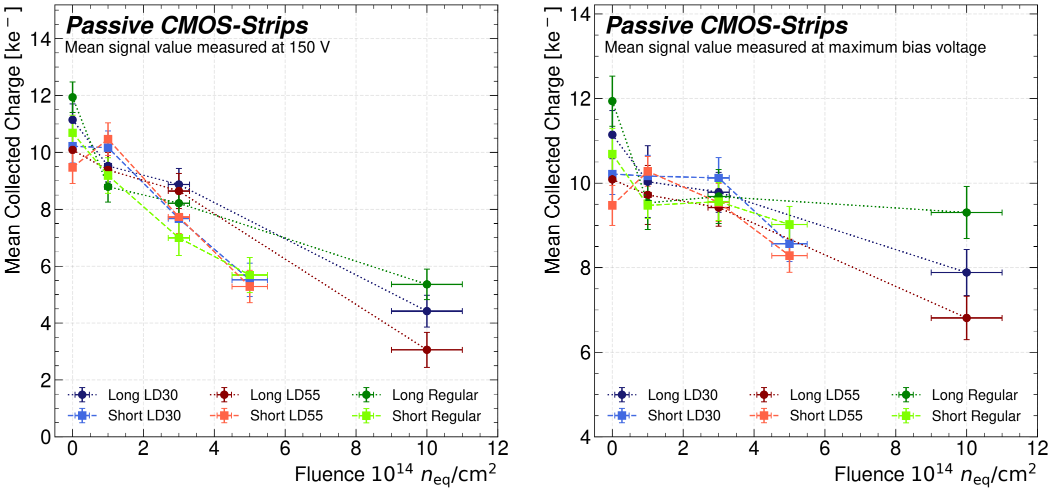

(a) **(b)**

Figure 78.: Mean collected charge as a function of the irradiation fluence for long and short sensors at (a) 150 V and (b) for the maximum bias voltage achieved. LD30 and LD55 refer to the Low-dose design. Lines between the data points are only a visual aid.

The aforementioned decrease of the charge collection with the increase of the fluence is evident from the plots. However, the strong performance degradation in Figure 78a is given by the increase in full depletion voltage, making the irradiated sensor operate under depleted. Even though annealed and not annealed sensors are included, the effect of annealing at 60°C for 80 minutes does not impact the collected charge, as seen from Figure 75. The picture changes when the study uses the mean MPV obtained from measurements at the maximum bias voltage, i.e., after full depletion for all the studied sensors. In this case, the performance decrease is less pronounced. The collected charge for the long sensors decreases between the nonirradiated and the highest fluence by roughly 30%, 33%, and 22% for the LD30, LD55, and Regular designs, respectively. In the short sensors, irradiated to lower highest fluence, the numbers are 16%, 13%, and 16%, respectively.

In addition, the recovery of the Regular design compared to the Low-dose design for the highest fluence is also clearly seen in both plots for the short and long sensors. There is currently no understanding of what mechanisms could be behind this finding. A plausible explanation could be attributed to local electric field peaks in the Regular design, causing charge multiplication. Charge multiplication has been observed in ATLAS ITk sensors of similar doping concentration at 1×10^{15} $\mathrm{n_{eq}/cm^2}$ [162, 163, 164]. The fact that the difference between the Regular and the Low-dose designs at 150 V and a fluence of 1×10^{15} $\mathrm{n_{eq}/cm^2}$ increases for the measurement at maximum bias offers some support to the charge multiplication hypothesis. It is clear that more studies, including TCT measurements and simulations, are necessary to validate this interpretation or find a different one.

The charge collection studies before irradiation showed that the stitching process does not impact the collected charge, as the sensors collected the same amount of charge in all the stitched areas. While the irradiated samples presented the expected degradation due to radiation damage, the collected charge across the stitched regions was also uniform, indicating that the stitching process has no impact on the sensor's performance after irradiation. Therefore, the studies demonstrated that strip sensors can be successfully produced in a commercial foundry using the standard CMOS technology and that the reticle stitching process can successfully produce large-area sensors suitable for applications in particle detectors.

Chapter 7

Conclusions

The High-Luminosity LHC should start operations at the beginning of 2029, delivering proton-proton collisions at unprecedented luminosities [47]. The envisioned physics objectives and operational conditions present demanding requirements for the performance of the detector subsystems, particularly the tracking detector. Unseen radiation damage [17] and pile-up [47] levels are predicted, making the current tracking system unsuitable for delivering the track and vertex reconstruction and radiation hardness requirements. Therefore, the ATLAS experiment will replace its current tracking detector with an all-silicon tracking system, the Inner Tracker, composed of silicon pixel and strip modules. An extensive characterization, including final-experimental-like conditions as beam tests, has accompanied the development of the new radiation-hard detector modules.

In the framework of this thesis, ITk Strip modules were studied before and after irradiation during beam test campaigns at DESY, and their performance was evaluated in terms of hit detection efficiency, noise levels, and tracking resolution. The sensors in the investigated modules were irradiated to a fluence of $1.1{\times}10^{15}$ $n_{\mathrm{eq}}/\mathrm{cm}^2$ which is equivalent to the expected fluence at the end-of-lifetime.

Regarding hit reconstruction efficiency, the strip modules must operate at a threshold where they provide 99% detection efficiency while keeping a noise occupancy below 0.1%. The beam test analysis showed that the modules meet the requirements even at the maximum irradiation fluence and dose received. In the case of non-irradiated modules, operational conditions are satisfied for thresholds between 0.5 fC (3.1 ke^-) and 2.2 fC (13.7 ke^-). This range allows for a comfortable operation before irradiation.

There is also a threshold range where the requirements are met for irradiated modules. This constitutes a milestone for the ITk Strip system, showing that the detector module prototypes delivered the desired performance even before fine-tuning the readout electronics and in high noise conditions, as found at the beam tests. However, the decreased collected charge and the increased noise due to radiation damage vastly reduce the operational range. Operation conditions are found for thresholds between 0.34 fC and 0.56 fC. While these ranges are small, the signal-to-noise ratio measured is well above the ITk Strip requirement of ten for all the modules.

In addition, the hit reconstruction efficiency was evaluated for different regions in the module. The analysis encompassed crucial areas, such as the intersegment regions between two strip rows. The results obtained demonstrate that the sensors, readout electronics, and tuning mechanisms implemented, such as threshold trimming, ensure consistent and homogeneous hit reconstruction efficiency that satisfies the 99% requirement throughout the entire module.

The tracking resolution and cluster size dependence with threshold were also investigated. For non- and irradiated modules, hits with cluster size one drive the detector's resolution for all threshold levels. Consequently, the measured resolution agrees with the expectation for single-strip clusters and binary readouts. In irradiated modules, due to the enhanced cross-talk, an increase of two strip hits was observed but, as mentioned, the resolution does not change significantly as a function of the threshold.

The beam test studies conducted in the framework of this thesis prove the ITk Strip will provide the required tracking reconstruction and detection efficiency performance during its entire operation lifetime under High-Luminosity LHC conditions. In addition, the results presented were crucial for successfully passing the ITk Strip Module Final Design Review [165] and the ITk Strip ASICs [166], as well as barrel modules Production Readiness Reviews [167].

The High-Luminosity LHC will likely not be the last collider built. The high-energy physics community, endorsed by the 2020 Update of the European Strategy for Particle Physics, is performing feasibility studies of the physics potential of a 100 TeV proton-proton collider. Regardless of the final shape of the accelerator, silicon sensors will continue to be the preferred choice for future tracking detectors. As the area covered by silicon in the tracking detectors of the experiments is expected to grow up to two times, it is imperative to explore silicon technologies that not only deliver the physics performance requirements but also scale up sensor manufacturing cost-effectively.

The CMOS technology has already been successfully employed for hybrid and monolithic-active pixel sensors in particle physics, and it has been the industry standard in Very Large-Scale Integration technology for over forty years. Therefore, CMOS technology is a prime candidate for future tracking detector applications as it combines industry and particle detector community know-how. However, the so-called stitching process must be used to produce strip sensors with an area of in the order of 10×10 cm^2, as in the case of the ATLAS ITk studied in this thesis. The stitching is required because the maximum size of the CMOS process photolithography masks is limited to 5 cm^2, with many foundries using 2×2 cm^2 reticles. Therefore, manufacturing sensors exceeding the reticle sizes requires stitching or connecting different reticles.

CMOS strip sensors fabricated in the LFoundry 150 nm process using reticle stitching were studied. Up to five reticles were stitched together to produce two sensor sizes and three designs. The designs influence the electric field distribution within the sensor and, therefore, the radiation hardness. The present study was designed to determine whether the stitching process impacted the sensor performance before and after irradiation.

The sensor's electrical characterization showed depletion voltages ranging from 30 to 35 V, with the Low-dose design having a higher depletion voltage than the Regular one. The higher depletion voltage of the Low-dose agrees with the expectation as the design has a higher effective doping concentration due to the extra n-well. In addition, breakdown voltages above 250 V were measured with a leakage current below 0.01 $\mu\text{A}/\text{cm}^2$.

Charge collection measurements with a beta source demonstrated that the sensors collect the expected amount of charge for a minimum ionizing particle across the entire active area before irradiation. After irradiation up to a fluence of 1×10^{15} $n_{\text{eq}}/\text{cm}^2$, the sensors are fully functional and collect between 20 to 40% less charge. The Regular design displays the best radiation hardness of all the designs. Furthermore, in the post-irradiated measurements, the amount of collected charge was uniform over all the stitched areas, evidencing no degradation of the stitching process after irradiation. These results were published in [144] and [158].

The measurements and results presented in this thesis demonstrate that large-area silicon strip sensors for particle detection applications can be successfully manufactured using standard CMOS technology in a commercial foundry using the reticle stitching processes. The latter constitutes an extremely important first step toward developing silicon strip detectors that can fully profit from industry-standard processes and potentially include elements of the readout electronics in the same substrate as the sensing volume.

Appendix A

ITSDAQ Noise Occupancy Tests

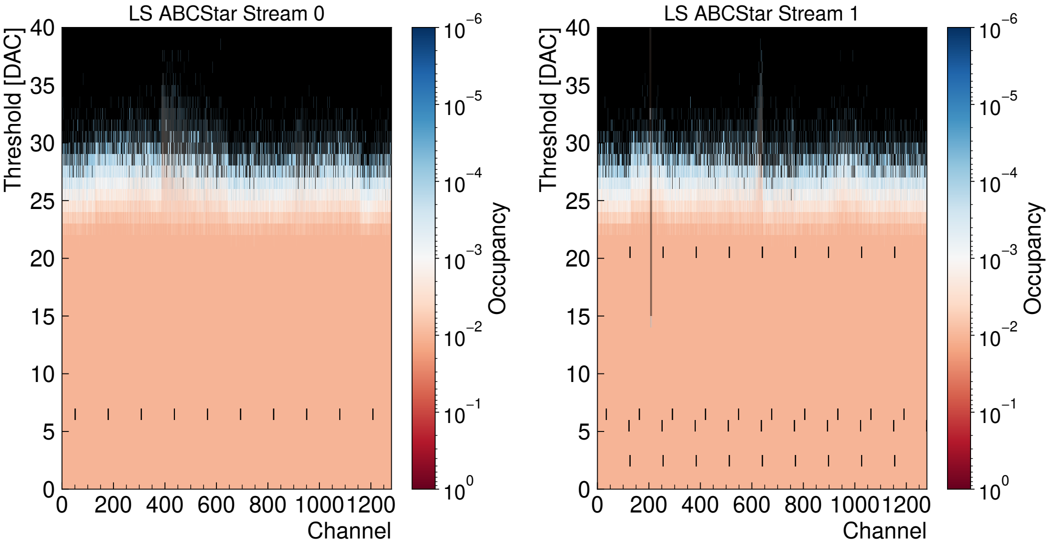

Figure 79.: Noise occupancy as a function of the applied threshold in the channel discriminators for the LS 2019 module.

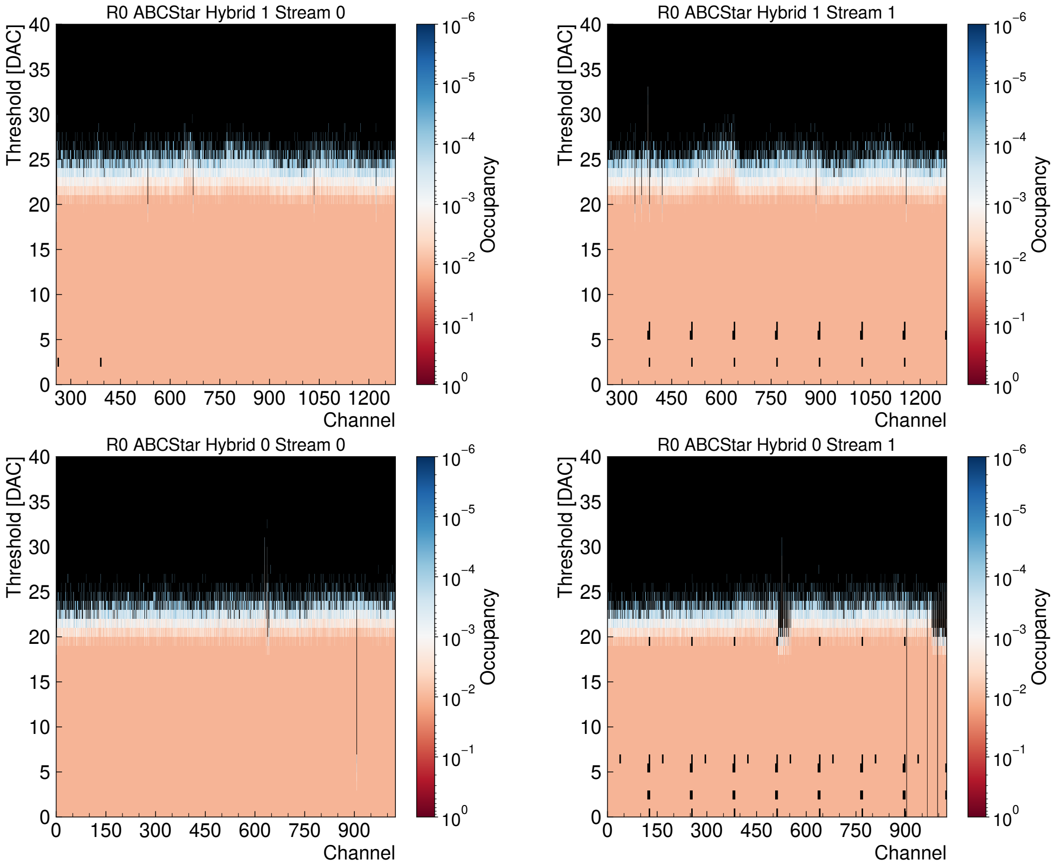

Figure 80.: Noise occupancy as a function of the applied threshold in the channel discriminators for the R0 2019 module.

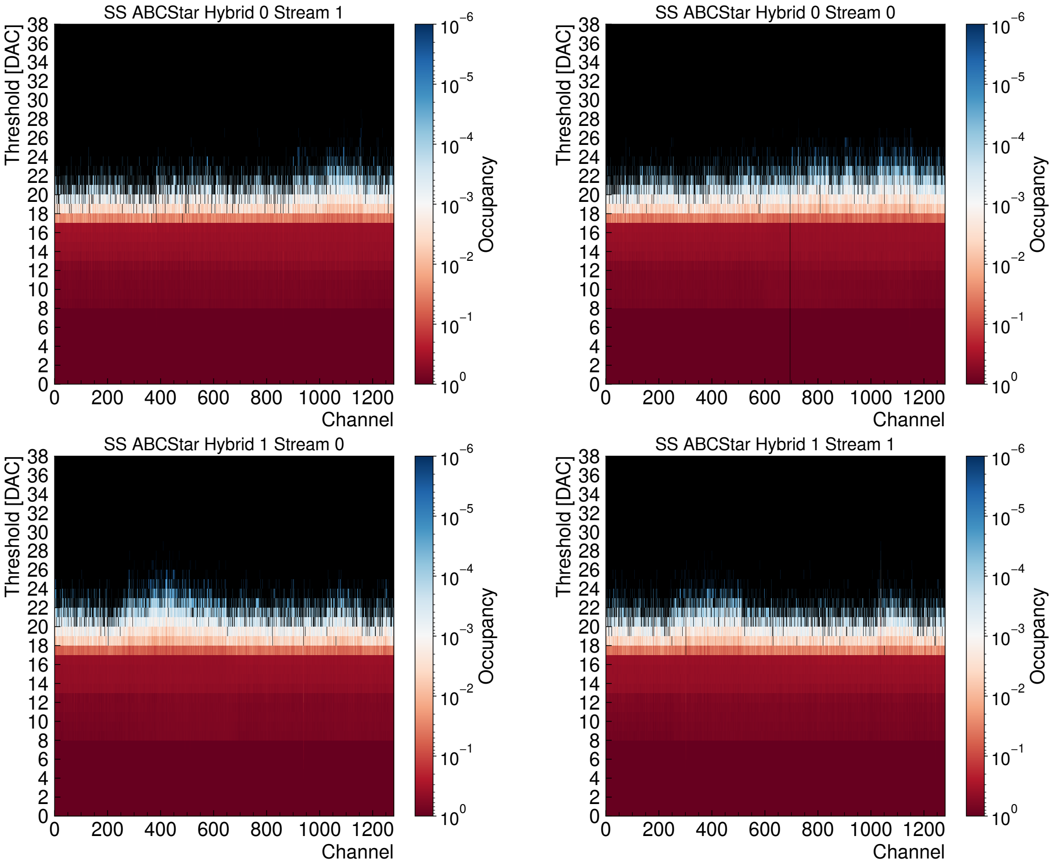

Figure 81.: Noise occupancy as a function of the applied threshold in the channel discriminators for the SS 2021 module.

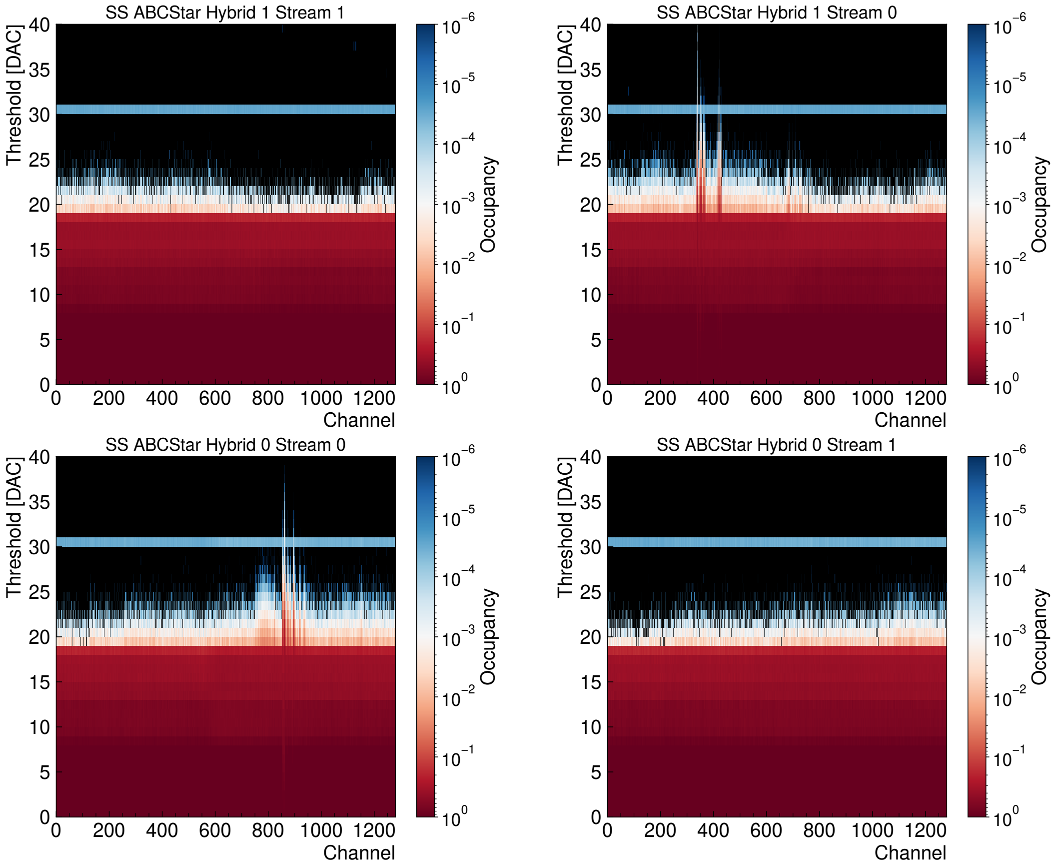

Figure 82.: Noise occupancy as a function of the applied threshold in the channel discriminators for the SS 2022 module.

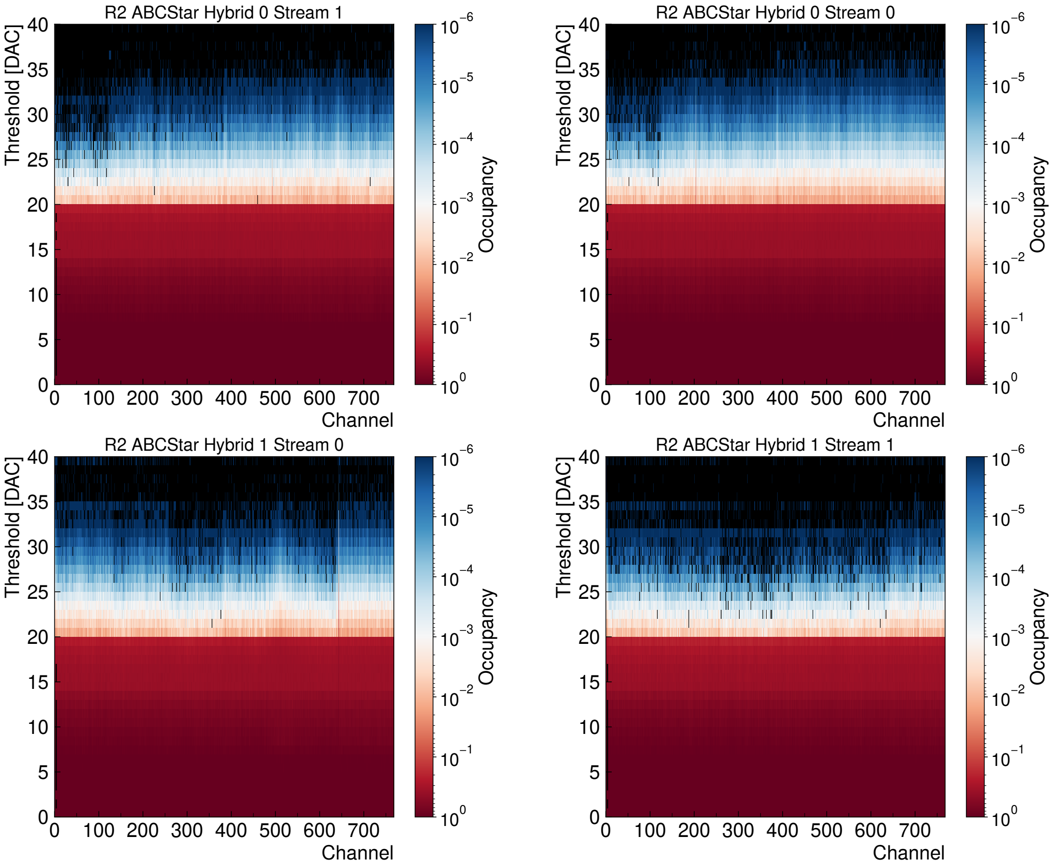

Figure 83.: Noise occupancy as a function of the applied threshold in the channel discriminators for the R2 2022 module.

Appendix B

Beam Test Reconstruction and Analysis Supplements

Telescope Performance Plots

Figure 84 shows the biased residual distributions for the x and y positions of the Mimosa26 telescope geometry employed in the 2019 beam test campaign.

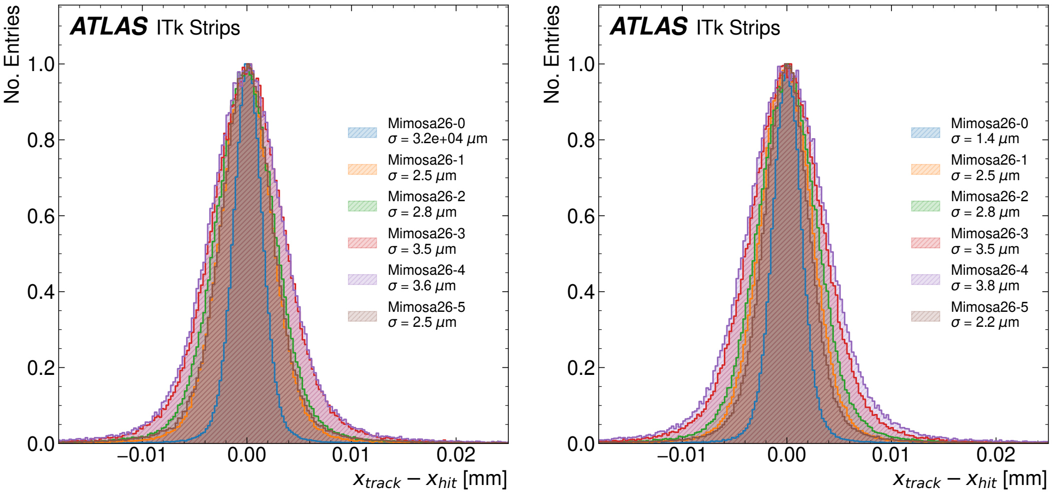

(a) **(b)**

Figure 84.: Residual distributions for (a) x and (b) y positions for the Mimosa26 planes geometry employed at the DESY beam test campaign in 2019. For both directions, an excellent alignment and resolutions below 4 µm for all the planes.

The timing plane is also part of the telescope setup and is used for time tagging the reconstructed tracks for efficiency calculation. Hence, it needs to be properly aligned. The timing plane uses a pixel detector with a pixel size of 50 × 250 µm^2, corresponding to binary resolutions of approximately 15 and 72 µm. Figure 85 shows the biased residual distributions obtained for the x and y positions of the timing plane in the 2019 beam test campaign. It can be observed that both distributions are well-centered around zero and that the obtained RMS matches the expected resolutions.

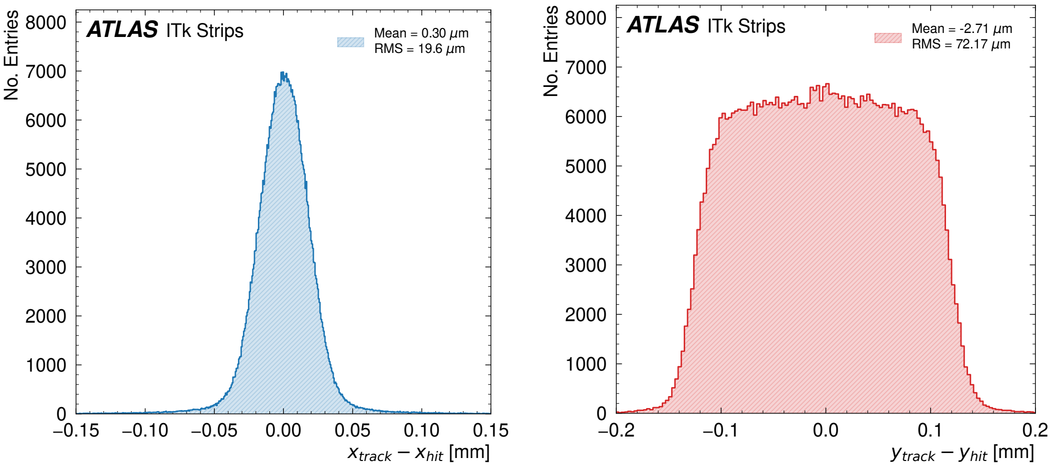

(a) **(b)**

Figure 85.: Residual distributions for (a) x and (b) y positions for the timing plane employed at the DESY beam test campaign in 2019. For both directions, excellent alignment is obtained.

LS Module 2019

Residual Distributions

The DUT residual distribution for a selection of thresholds of 24, 60, 70, 90, and 100 DAC is shown in Figure 86. The DAC thresholds correspond to 0.36, 2.52. 4.00, 4.40, and 5.28 fC. Only the x coordinate is sensitive to alignment in strip sensors. The y position is checked only to ensure the track passes through the DUT. The obtained RMS values show good agreement with the expected binary resolution of the module for all the thresholds. The distributions for the other studied positions show almost identical behavior.

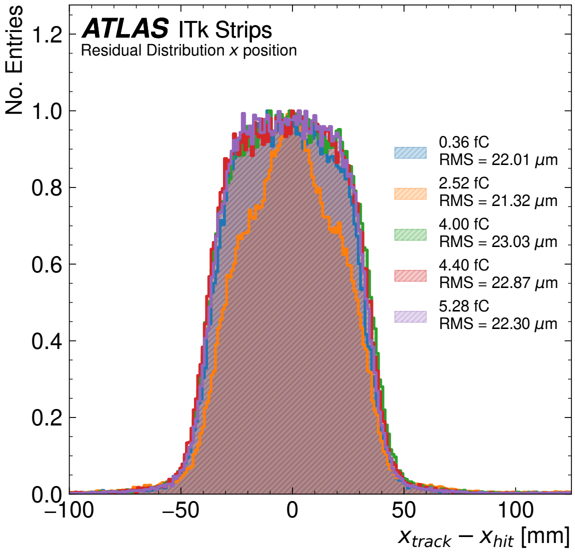

Figure 86.: Unbiased residual distributions for the x positions for the non-irradiated LS module 2019. The RMS values are in agreement with the expected resolution, given by Equation 26.

Efficiency and operational windows

The ITk Strip modules must operate with an efficiency higher than 99% and a noise occupancy below 10^{-3}. Therefore, in addition to the position shown in Figure 47a on the *away* strip segment, three more positions, an additional one in the away segment and two in the *under* segment, were investigated. Figure 87 shows the efficiency curves obtained for all the positions and the operational window plots for the three additional ones. In Figure 87a, it is observed that the efficiency response of the module is uniform for all the positions over a large range of thresholds. In addition, all the investigated positions meet the requirement of having an efficiency higher than 99%.

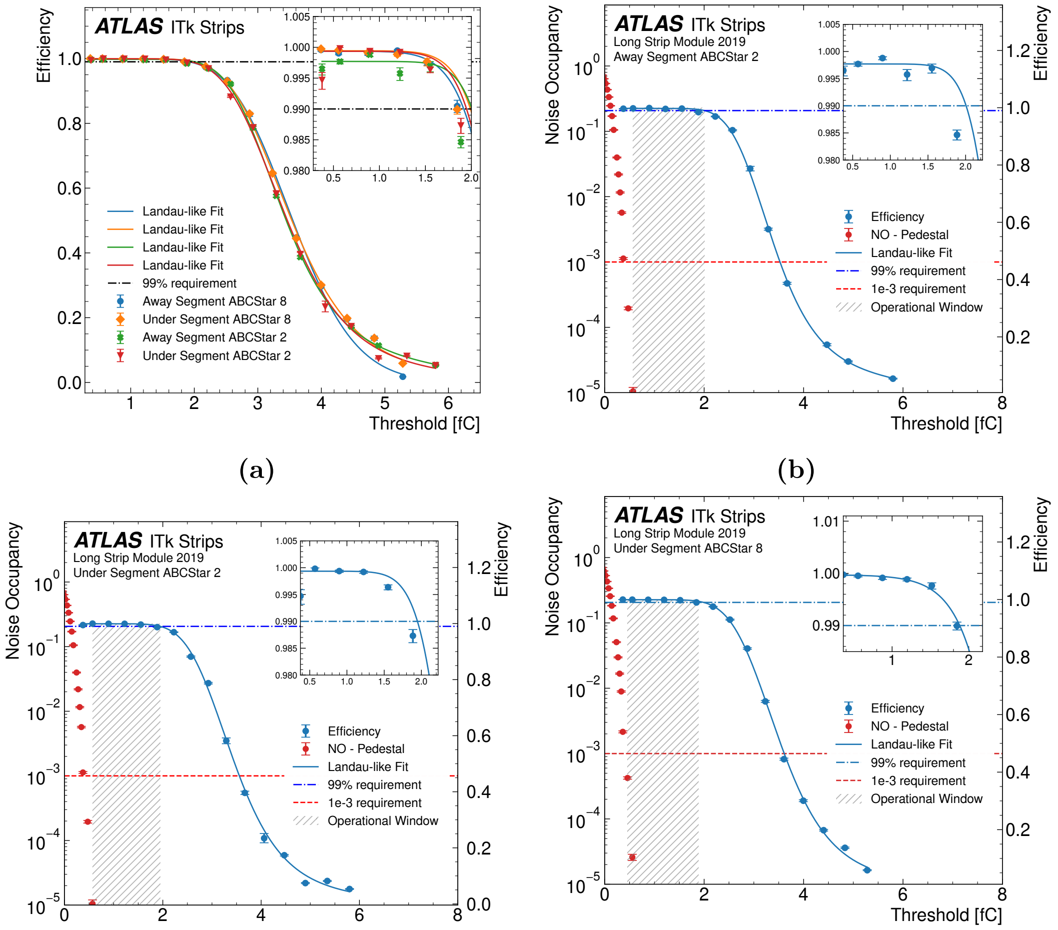

(a) (b) (c) (d)

Figure 87.: (a) efficiency as a function of the threshold for all the investigated positions in the LS 2019 module. Efficiency and noise occupancy as a function of the threshold for (b) position on the ABCStar 7 on the away segment, (c) position on ABCStar 8 on the under segment, and (d) position on ABCStar 3 on the under segment. In (a), (b), and (c), the operational window for the position is indicated.

Figures 87b, 87c and 87d show the efficiency and noise occupancy as a function of the threshold. It can be observed that a comfortable operation window is found for all the positions.

R0 2019 Module

Efficiency and operational windows

Three more positions, two in the away and one in the under segment of hybrid-1 were investigated in the R0 module. The lower two segments, read out by the ASICs in hybrid-0, were unreachable. Figure 88 shows the efficiency and noise occupancy as a function of the threshold for the analyzed positions. It can be observed that there is a wide range of thresholds where the operational requirements are satisfied.

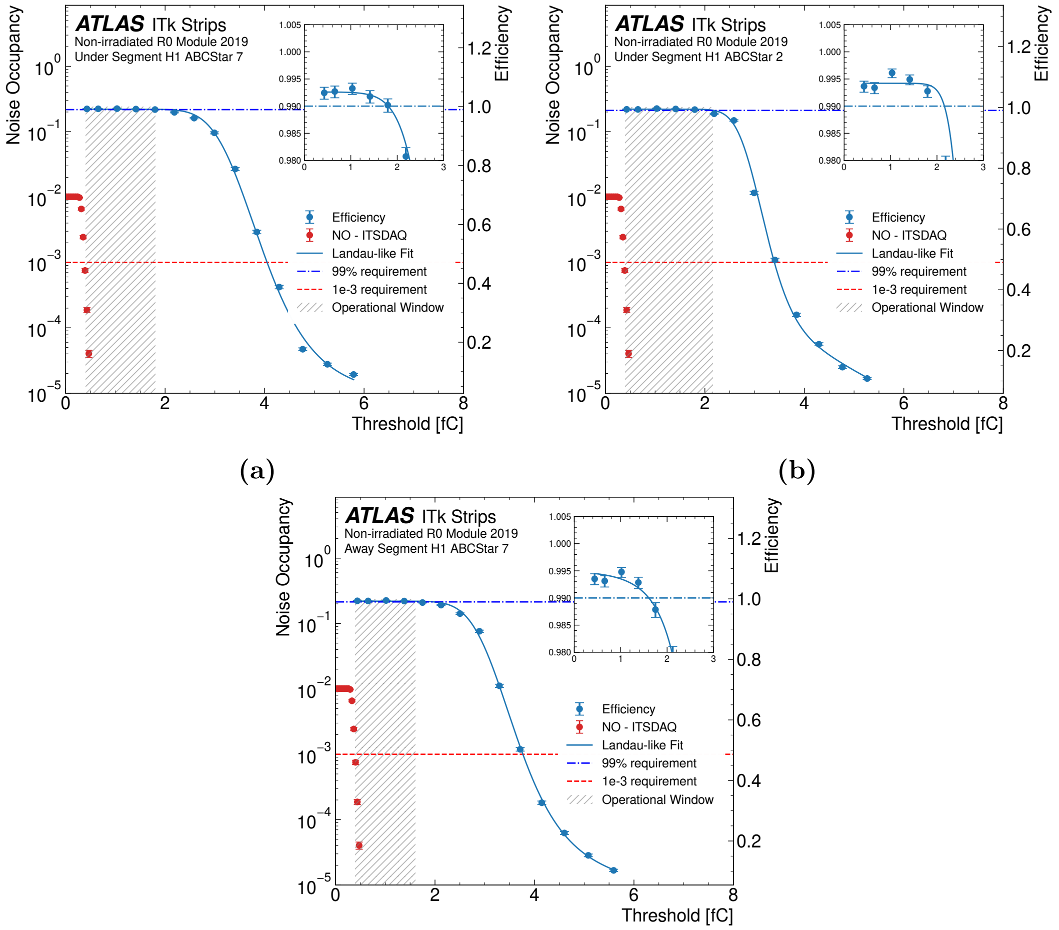

(a)

(b)

(c)

Figure 88.: Efficiency and noise occupancy as a function of the threshold for the ABCStar 7 (a) and ABCStar 2 (b) in the *under* segment of hybrid 1 (H1) and for the ABCStar 7 in the *away* segment in hybrid 1 (H1). The noise occupancy has been obtained from the ITSDAQ noise occupancy test.

SS 2021 Module

Efficiency and operational windows

Due to the constraints in the range of the movable stages during the beam test campaign, the lower two strip rows were unreachable. Therefore, two more positions were analyzed in the SS 2021 module. One on ABCStar 4 of the away segment and one on the ABCStar 5 of the under segment. Figure 89 shows the efficiency and noise occupancy as a function of the threshold for the two measured positions. An operational window ($0.33 - 0.55$ fC) is found for both ASICs.

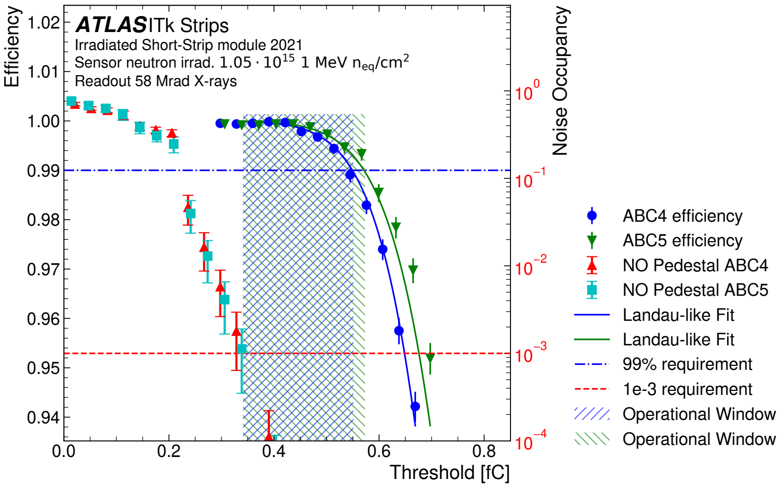

Figure 89.: Efficiency and noise occupancy as a function of the threshold for two ASICs in the irradiated SS 2021 module. An operation window is found for both ABCStar ASICs [168].

Residual Distributions

Figure 90 shows the unbiased residual distribution for one of the positions where all thresholds have been included. The residual distribution for all cluster sizes has an RMS of 29.72 µm which is approximately 36% larger than the binary resolution expectation. In contrast, the distribution for cluster size one has an RMS of 23.41 µm about 7% larger than the expectation. Both values agree with the predicted behavior as the binary resolution given by $pitch/\sqrt{12}$ is only valid for single strip clusters. When larger cluster sizes are considered, the resolution deteriorates as the clustering algorithm does not have charge information, and clusters with sizes larger than two push the residuals to larger values.

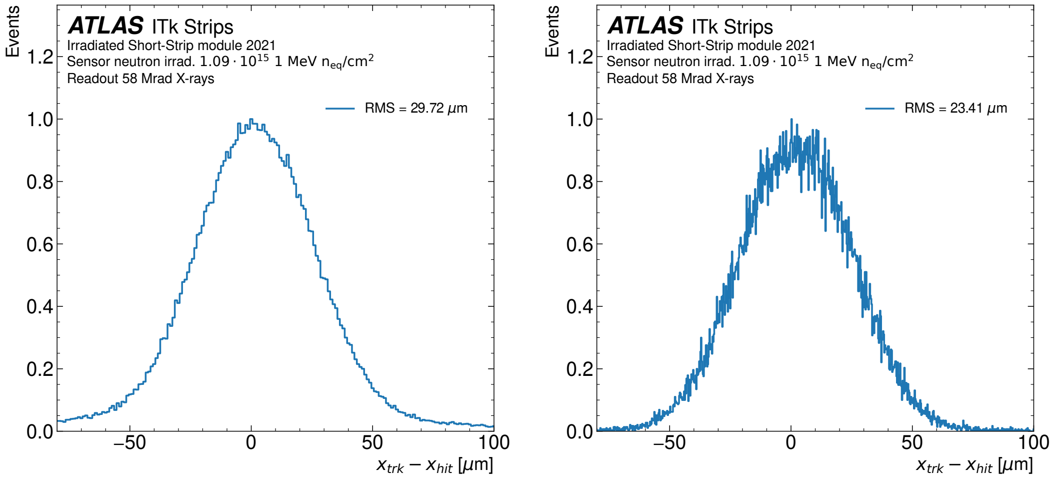

(a) (b)

Figure 90.: Irradiated SS 2021 unbiased residual distributions for (a) all cluster sizes and (b) cluster size one. The distributions are rescaled to the [0, 1] interval for easier comparison.

SS 2022 Module

Figure 91 shows the efficiency and noise occupancy as a function of the threshold for one position in each of the four strip segments in the SS 2022 module. For all the analyzed positions, a range of thresholds is found where the modules can operate with efficiency higher than 99% and a noise occupancy below 10^{-3}.

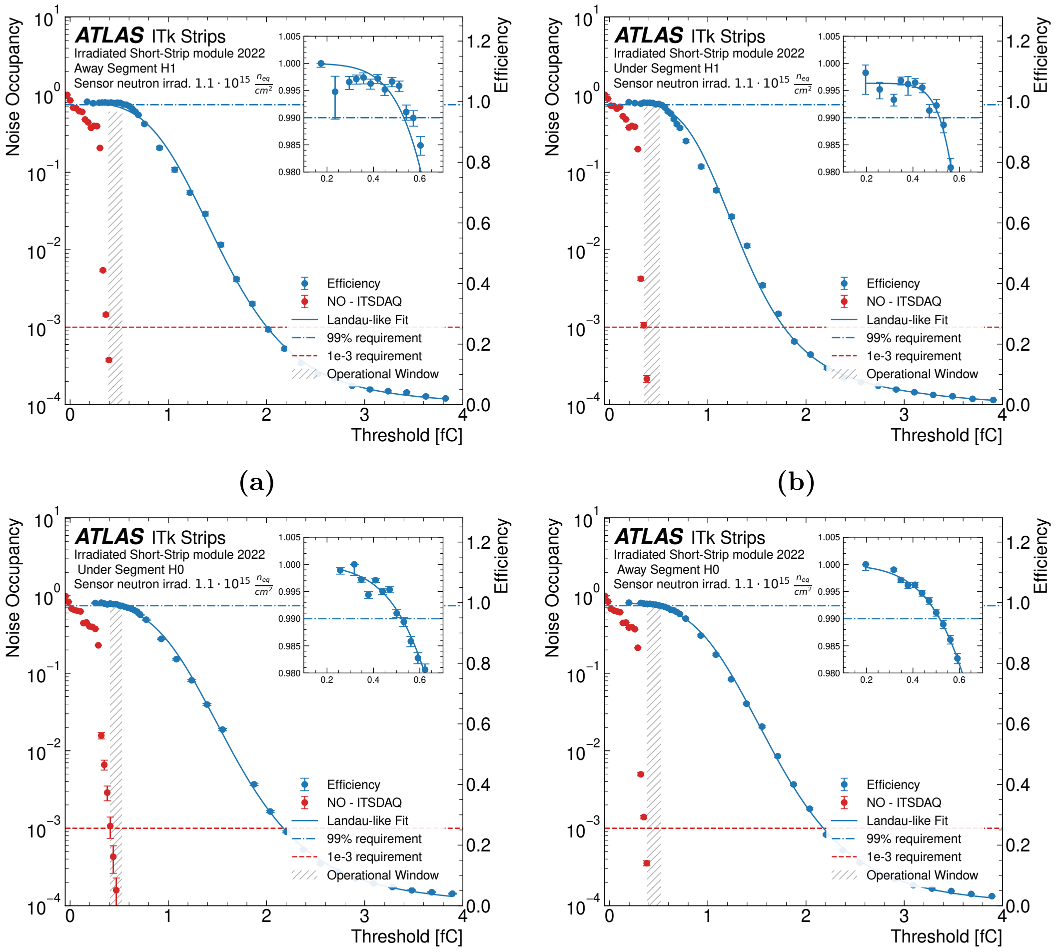

(a) (b)

(c) (d)

Figure 91.: Efficiency and noise occupancy as a function of the threshold for the *away* (a) and (b) *under* segments in hybrid 1 (H1) and for the *away* (c) and *under* (d) segments in hybrid 0 (H0) of the irradiated SS 2022 module. The noise occupancy has been obtained from the ITSDAQ noise occupancy test.

Appendix C

Investigated Modules

Table 6.: List of investigated modules and the respective sensor and readout iteration used. Sensor irradiation fluences, readout electronics TID, and the safety factors employed are also summarized.

Module	Sensor	Sensor Irrad. [10^{15}n$_{eq}$/cm^2]	Safety Factor	Chipset	Chipset TID [Mrad]	Safety Factor
LS 2019	ATLAS17LS	N/A	N/A	StarV0	N/A	N/A
R0 2019	ATLAS12EC	N/A	N/A	StarV0	N/A	N/A
Irrad. SS 2021	ATLAS18SS	1.1	1.5	StarV0 PPA	58	1.8
Irrad. SS 2022	ATLAS18SS	1.1	1.5	StarV0 PPB	N/A	N/A
Irrad. R2 2022	ATLAS18R2	1.1	1.5	StarV0 PPB	66	3.1

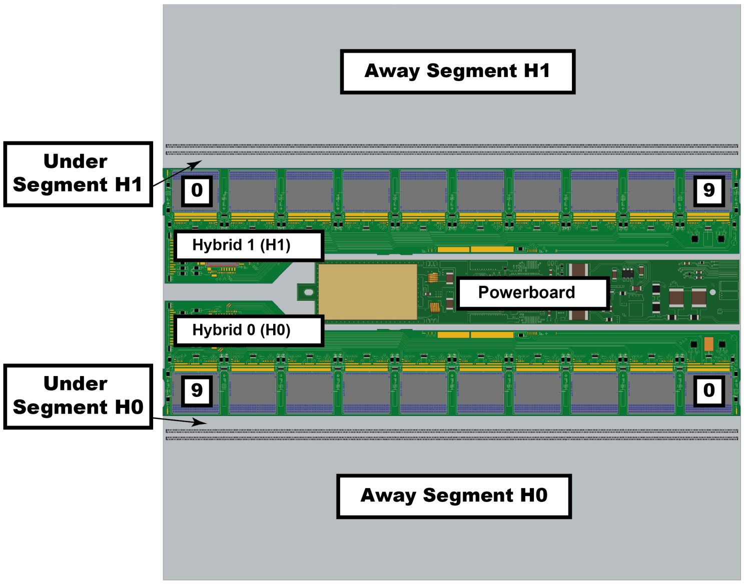

Figure 92.: Drawing of the Short Strip module depicting the naming convention for strip regions used in this thesis. The first and last ABCStar ASICs of each hybrid are identified with numbers.

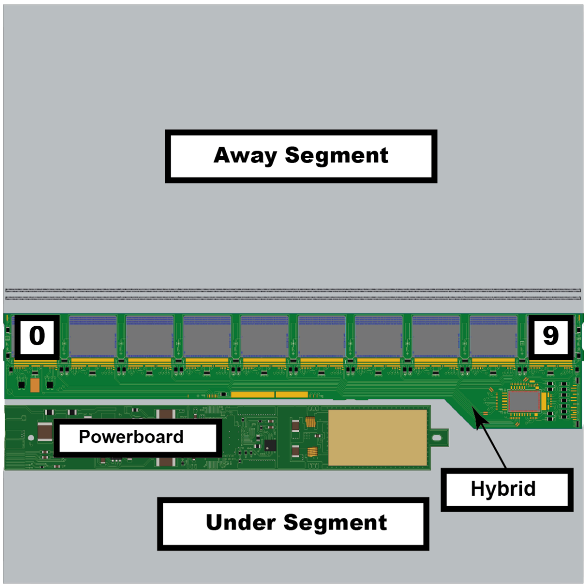

Figure 93.: Drawing of the Long Strip module depicting the naming convention for strip regions used in this thesis. The first and last ABCStar ASICs of each hybrid are identified with numbers.

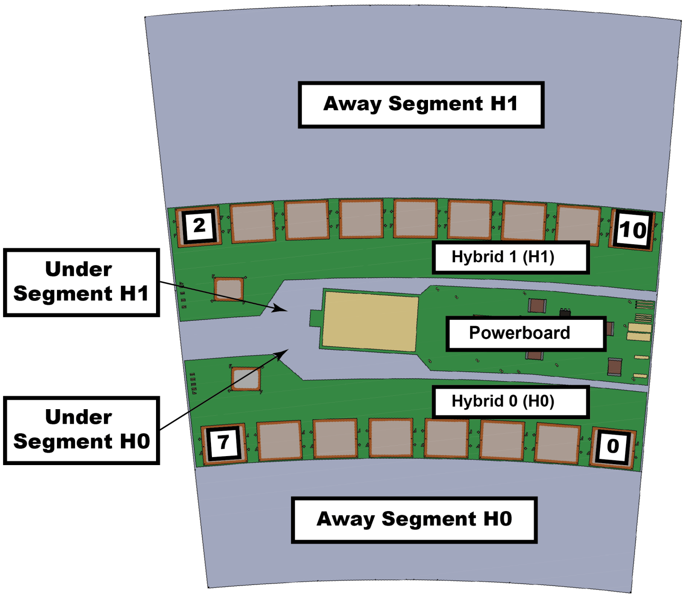

Figure 94.: Drawing of the R0 module depicting the naming convention for strip regions used in this thesis. The first and last ABCStar ASICs of each hybrid are identified with numbers.

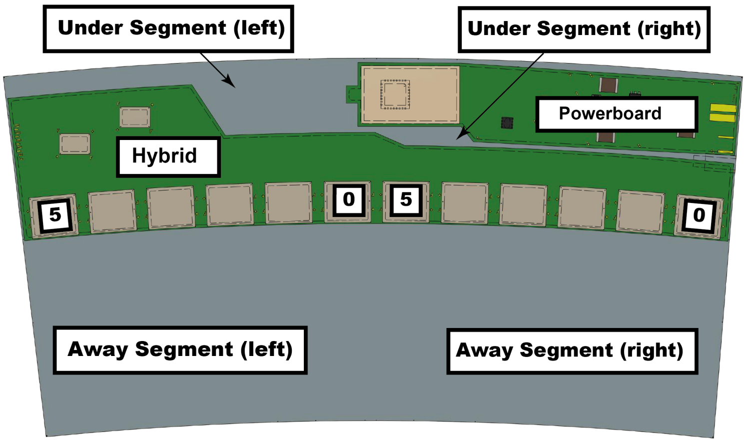

Figure 95.: Drawing of the R2 module depicting the naming convention for strip regions used in this thesis. The R2 module has a single hybrid, but the ABCStar ASICs send data to two HCCs. Hence, the ASICs are distributed as shown, and the strip rows are further divided between left and right.

Bibliography

[1] E. H. Heijne, *"Semiconductor detectors in the low countries"*, *Nucl. Instrum. Meth. A.* **509**, 1 (2003)

[2] W. Shockley, *"The theory of p-n junctions in semiconductors and p-n junction transistors"*, *BSTJ* **28**, 435 (1949)

[3] J. Bardeen & W. H. Brattain, *"The Transistor, A Semi-Conductor Triode"*, *Phys. Rev.* **74**, 230 (1948)

[4] K. G. McKay, *"A. Germanium Counter"*, *Phys. Rev.* **76**, 1537 (1949)

[5] E. Heijne et al., *"A silicon surface barrier microstrip detector designed for high energy physics"*, *Nucl. Instrum. Meth.* **178**, 331 (1980)

[6] J. Kemmer, *"Fabrication of low noise silicon radiation detectors by the planar process"*, *Nucl. Instrum. Meth.* **169**, 499 (1980)

[7] B. Hyams et al., *"A silicon counter telescope to study short-lived particles in high-energy hadronic interactions"*, *Nucl. Instrum. Meth.* **205**, 99 (1983)

[8] ATLAS Collaboration, *"Measurements of Higgs boson production and couplings in diboson final states with the ATLAS detector at the LHC"*, *Phys. Lett. B* **726**, 88 (2013), [Erratum: Phys.Lett.B 734, 406–406 (2014)]

[9] CMS Collaboration, *"Observation of a New Boson at a Mass of 125 GeV with the CMS Experiment at the LHC"*, *Phys. Lett. B* **716**, 30 (2012)

[10] Particle Data Group Collaboration, R. L. Workman et al., *"Review of Particle Physics"*, *PTEP* **2022**, 083C01 (2022)

[11] S. O. Bilson-Thompson et al., *"Quantum gravity and the standard model"*, *Class. Quantum Grav.* **24**, 3975 (2007)

[12] A. Arbey & F. Mahmoudi, *"Dark matter and the early Universe: A review"*, *Prog. Part. Nucl. Phys.* **119**, 103865 (2021)

[13] M. Li et al., *"Dark Energy: A Brief Review"*, *Front. Phys.* **8**, 828 (2013)

[14] L. Canetti et al., *"Matter and antimatter in the universe"*, *New J. Phys.* **14**, 095012 (2012)

[15] A. de Gouvêa, *“Neutrino Mass Models”*, *Annu. Rev. Nucl. Part. Sci.* **66**, 197 (2016)

[16]

[17] ATLAS Collaboration, *“Technical Design Report for the ATLAS Inner Tracker Strip Detector”*, `https://cds.cern.ch/record/2257755`

[18] ATLAS Collaboration, *“Technical Design Report for the ATLAS Inner Tracker Pixel Detector”*, `https://cds.cern.ch/record/2285585`

[19] L. Evans & P. Bryant, *“LHC Machine”*, *JINST* **3**, S08001 (2008)

[20] E. Mobs, *“The CERN accelerator complex. Complexe des accélérateurs du CERN”*, General Photo, `https://cds.cern.ch/record/2197559`

[21] S. Fartoukh et al., *“LHC Configuration and Operational Scenario for Run 3”*, `https://cds.cern.ch/record/2790409`

[22] The ATLAS Collaboration, *“The ATLAS Experiment at the CERN Large Hadron Collider”*, *JINST* **3**, S08003 (2008)

[23] CMS Collaboration, *“The CMS Experiment at the CERN LHC”*, *JINST* **3**, S08004 (2008)

[24] LHCb Collaboration, *“LHCb detector performance”*, *Int. J. Mod. Phys. A* **30**, 1530022 (2015)

[25] ALICE Collaboration, *“The ALICE experiment at the CERN LHC”*, *JINST* **3**, S08002 (2008)

[26] ATLAS Collaboration, *“ATLAS inner detector: Technical Design Report, 1”*, `https://cds.cern.ch/record/331063`

[27] ATLAS Collaboration, *“ATLAS inner detector: Technical Design Report, 2”*, `https://cds.cern.ch/record/331064`

[28] ATLAS Collaboration, *“ATLAS pixel detector: Technical Design Report”*, `https://cds.cern.ch/record/381263`

[29] G. Aad et al., *“ATLAS pixel detector electronics and sensors”*, *JINST* **3**, P07007 (2008)

[30] A. Abdesselam et al., *“The barrel modules of the ATLAS semiconductor tracker”*, *Nucl. Instrum. Meth. A* **568**, 642 (2006)

[31] ATLAS Collaboration, *“The ATLAS semiconductor tracker end-cap module”*, *Nucl. Instrum. Meth. A* **575**, 353 (2007)

[32] A. Ahmad et al., *“The Silicon microstrip sensors of the ATLAS semiconductor tracker”*, *Nucl. Instrum. Meth. A* **578**, 98 (2007)

[33] ATLAS Collaboration, *"The ATLAS TRT Barrel Detector"*, *JINST* **3**, P02014 (2008)

[34] ATLAS Collaboration, *"The ATLAS TRT end-cap detectors"*, *JINST* **3**, P10003 (2008)

[35] ATLAS Collaboration, *"The ATLAS Transition Radiation Tracker (TRT) proportional drift tube: Design and performance"*, *JINST* **3**, P02013 (2008)

[36] ATLAS Collaboration, *"The ATLAS Insertable B-Layer: from construction to operation"*, `http://cds.cern.ch/record/2221972`

[37] ATLAS Collaboration, *"ATLAS central solenoid: Technical Design Report"*, Electronic version not available, `https://cds.cern.ch/record/331067`

[38] ATLAS Collaboration, *"ATLAS calorimeter performance: Technical Design Report"*, `https://cds.cern.ch/record/331059`

[39] ATLAS Collaboration, *"ATLAS liquid-argon calorimeter: Technical Design Report"*, `https://cds.cern.ch/record/331061`

[40] ATLAS Collaboration, *"ATLAS tile calorimeter: Technical Design Report"*, `https://cds.cern.ch/record/331062`

[41] ATLAS Collaboration, *"ATLAS muon spectrometer: Technical Design Report"*, `https://cds.cern.ch/record/331068`

[42] ATLAS Collaboration, *"ATLAS magnet system: Technical Design Report, 1"*, `https://cds.cern.ch/record/338080`

[43] ATLAS Collaboration, *"Experiment Briefing: Keeping the ATLAS Inner Detector in perfect alignment"*, General Photo, `https://cds.cern.ch/record/2723878`

[44] C. Da Via et al., *"3D silicon sensors: Design, large area production and quality assurance for the ATLAS IBL pixel detector upgrade"*, *Nucl. Instrum. Meth. A* **694**, 321 (2012)

[45] ATLAS Collaboration, *"The Inner Detector"*, URL:https://atlas.cern/discover/detector/inner-detector. Accessed: 14.01.2022, `https://atlas.cern/discover/detector/inner-detector`

[46] V. L. Ginzburg & I. M. Frank, *"Radiation of a uniformly moving electron due to its transition from one medium into another"*, J. Phys. (USSR) **9**, 353 (1945)

[47] *"High-Luminosity Large Hadron Collider (HL-LHC): Technical Design Report V. 0.1"*, https://e-publishing.cern.ch/index.php/CYRM/issue/view/40

[48] ATLAS Collaboration, *"ITk Pixel Layout Updates"*, URL: https://atlas.web.cern.ch/Atlas/GROUPS/PHYSICS/PLOTS/ITK-2020-002/. Accessed: 16.01.2022

[49] C. Haber et al., *"Production and testing of the powerboard for ATLAS ITk Strip barrel modules"*, *JINST* **18**, C01043 (2023)

[50] W. Lu et al., *"Development of the ABCStar front-end chip for the ATLAS silicon strip upgrade"*, *JINST* **12**, C04017 (2017)

[51] L. Poley et al., *"The ABC130 barrel module prototyping programme for the ATLAS strip tracker"*, *JINST* **15**, P09004 (2020)

[52] Y. Unno et al., *"Development of n+-in-p large-area silicon microstrip sensors for very high radiation environments – ATLAS12 design and initial results"*, *Nucl. Instrum. Meth. A.* **765**, 80 (2014)

[53] ATLAS Collaboration, *"Technical Specification for the Supply of Silicon Sensors for the ATLAS Inner Tracker upgrade project"*, URL: https://edms.cern.ch/document/2781829/1. Accessed: 16.01.2022

[54] C. Lacasta et al., *"Design of the first full size ATLAS ITk strip sensor for the endcap region"*, *Nucl. Instrum. Meth. A.* **924**, 137 (2019)

[55] C. G. Argos et al., *"Front-end Electronics of the Forward Strip Detector for the ATLAS HL-LHC Upgrade"*, *PoS (TWEPP2018)* **343**, 014

[56] K. Mahboubi et al., *"The front-end hybrid for the ATLAS HL-LHC silicon strip tracker"*, *JINST* **9**, C02027 (2014)

[57] A. Affolder et al., *"DC-DC converters with reduced mass for trackers at the HL-LHC"*, *JINST* **6**, C11035 (2011)

[58] H. Bethe, *"Zur Theorie des Durchgangs schneller Korpuskularstrahlen durch Materie"*, Annalen der Physik **397**, 325 (1930)

[59] F. Bloch, *"Bremsvermögen von Atomen mit mehreren Elektronen"*, Zeitschrift für Physik 1933 81:5 **81**, 363 (1933)

[60] Particle Data Group Collaboration, P. Zyla et al., *"Review of Particle Physics"*, PTEP **2020**, 083C01 (2020)

[61] H. Kolanoski & N. Wermes, *"Particle Detectors: Fundamentals and Applications"*, OUP Oxford (2020)

[62] L. Landau, *"On the energy loss of fast particles by ionization"*, J. Phys. (USSR) **8**, 201 (1944)

[63] P. V. Vavilov, *"Ionization losses of high-energy heavy particles"*, Sov. Phys. JETP **5**, 749 (1957)

[64] H. Bichsel, *"Straggling in thin silicon detectors"*, Rev. Mod. Phys. **60**, 663 (1988)

[65] SiLab-Bonn, *"`pylandau`"*, URL: https://github.com/SiLab-Bonn/pylandau. Accessed: 16.03.2022

[66] P. A. Cerenkov, *"Visible radiation produced by electrons moving in a medium with velocities exceeding that of light"*, Phys. Rev. **52**, 378 (1937)

[67] Y.-S. Tsai, *"Erratum: Pair production and bremsstrahlung of charged leptons"*, Rev. Mod. Phys. **49**, 421 (1977)

[68] E. Rutherford, *"The scattering of alpha and beta particles by matter and the structure of the atom"*, Phil. Mag. Ser. 6 **21**, 669 (1911)

[69] F. Bloch, *"Über die Quantenmechanik der Elektronen in Kristallgittern"*, *Z. Phys.* **52**, 555 (1929)

[70] S. Sze, *"Semiconductor Devices: Physics and Technology"*, John Wiley & Sons Singapore Pte. Limited (2012)

[71] G. Anner, *"Planar Processing Primer"*, Springer Netherlands (2012)

[72] L. B. A. Hommels et al., *"Detailed studies of full-size ATLAS12 sensors"*, *Nucl. Instrum. Meth. A* **831**, 167 (2016)

[73] C. Hu, *"Modern Semiconductor Devices for Integrated Circuits"*, Prentice Hall (2010)

[74] A. Chilingarov, *"Temperature dependence of the current generated in Si bulk"*, *JINST* **8**, P10003 (2013)

[75] C. Leroy & P. Rancoita, *"Silicon Solid State Devices and Radiation Detection"*, World Scientific Publishing Company Pte Limited (2012)

[76] H. Spieler & K. (Firm), *"Semiconductor Detector Systems"*, OUP Oxford (2005)

[77] W. Shockley, *"Currents to conductors induced by a moving point charge"*, *J. Appl. Phys.* **9**, 635 (1938)

[78] S. Ramo, *"Currents Induced by Electron Motion"*, *Proc. IRE* **27**, 584 (1939)

[79] G. Lindström et al., *"Radiation hard silicon detectors—developments by the RD48 (ROSE) collaboration"*, *Nucl. Instrum. Meth. A.* **466**, 308 (2001)

[80] I. Pintilie et al., *"Stable radiation-induced donor generation and its influence on the radiation tolerance of silicon diodes"*, *Nucl. Instrum. Meth. A.* **556**, 197 (2006)

[81] V. Van Lint, *"Mechanisms of Radiation Effects in Electronic Materials"*, Wiley (1980)

[82] G. Lindström et al., *"Radiation hardness of silicon detectors – a challenge from high-energy physics"*, *Nucl. Instrum. Meth. A.* **426**, 1 (1999)

[83] M. Moll, *"Radiation damage in silicon particle detectors: Microscopic defects and macroscopic properties"*, Ph.D. Thesis, University of Hamburg, 1999

[84] M. Moll, *"Displacement damage in silicon detectors for high energy physics."*, *IEEE Trans. Nucl. Sci.* **65**, 1561 (2018)

[85] M. Moll et al., *"Leakage current of hadron irradiated silicon detectors – material dependence"*, *Nucl. Instrum. Meth. A.* **426**, 87 (1999)

[86] M. Moll et al., *"Relation between microscopic defects and macroscopic changes in silicon detector properties after hadron irradiation"*, *Nucl. Instrum. Meth. B.* **186**, 100 (2002)

[87] O. Krasel et al., *"Measurement of trapping time constants in proton-irradiated silicon pad detectors"*, *IEEE Trans. Nucl. Sci.* **51**, 3055 (2004)

[88] N. Wermes, *"Pixel Detectors"*, `https://cds.cern.ch/record/913132`

[89] M. Krammer, *"Halbleiterdetektoren. Detektoren in Der Hochenergiephysik - GSI"*, URL: https://web-docs.gsi.de/~wolle/Schuelerlabor/TALKS/DETEKTOREN/VO-0-Inhalt.pdf. Accessed: 24.01.2022

[90] D. J. Fitzgerald & A. S. Grove, *"Mechanisms of Channel Current Formation in Silicon P-N Junctions"*, in *"Fourth Annual Symposium on the Physics of Failure in Electronics"*, 315-332

[91] Y. Unno et al., *"Evaluation of p-stop structures in the n-side of n-on-n silicon strip detector"*, *IEEE Trans. Nucl. Sci.* **45**, 401 (1998)

[92] G. Pellegrini et al., *"Technology of p-type microstrip detectors with radiation hard p-spray, p-stop and moderated p-spray insulations"*, *Nucl. Instrum. Meth. A* **579**, 599 (2007), Proceedings of the 6th "Hiroshima" Symposium on the Development and Application of Semiconductor Detectors

[93] F. Hartmann, *"Evolution of Silicon Sensor Technology in Particle Physics"*, Springer Berlin Heidelberg (2008)

[94] R. Diener et al., *"The DESY II Test Beam Facility"*, *Nucl. Instrum. Meth. A* **922**, 265 (2019)

[95] H. Jansen et al., *"Performance of the EUDET-type beam telescopes"*, *EPJ Tech. Instrum.* **3**, 7 (2016)

[96] EUDET Project, *"EUDET: Detector RD towards the International Linear Collider"*, URL: https://www.eudet.org/. Accessed: 17.02.2022

[97] J. Baudot et al., *"First test results of MIMOSA-26, a fast CMOS sensor with integrated zero suppression and digitized output"*, *IEEE Nucl Sci Symp Conf Rec (2009)* , 1169 (2009)

[98] P. Ahlburg et al., *"EUDAQ-a data acquisition software framework for common beam telescopes"*, *JINST* **15**, P01038 (2020)

[99] L. Caminada et al., *"ATLAS FE-I4 ASIC"*, *PoS* **Vertex 2012**, 023 (2013)

[100] M. Backhaus et al., *"Development of a versatile and modular test system for ATLAS hybrid pixel detectors"*, *Nucl. Instrum. Meth. A* **650**, 37 (2011)

[101] CLICdp Collaboration, J. Kröger et al., *"User Manual for the Corryvreckan Test Beam Data Reconstruction Framework, Version 1.0"*

[102] T. B. others, *"EUTelescope: A modular reconstruction framework for beam telescope data"*, *JINST* **15**, P09020 (2020)

[103] M. J. Williams, *"Evaluation of fine-pitch hybrid silicon pixel detector prototypes for the CLIC vertex detector in laboratory and test-beam measurements"*, PhD thesis. Glasgow University of Glasgow, 2020

[104] C. Kleinwort, *"General Broken Lines as advanced track fitting method"*, *Nucl. Instrum. Meth. A* **673**, 107 (2012)

[105] V. Blobel et al., *"Fast alignment of a complex tracking detector using advanced track models"*, *Comput. Phys. Commun.* **182**, 1760 (2011)

[106] F. James & M. Roos, *"Minuit - a system for function minimization and analysis of the parameter errors and correlations"*, *Comput. Phys. Commun.* **10**, 343 (1975)

[107] The ROOT Authors, *"ROOT Reference Guide: MINUIT2"*, URL: https://root.cern/doc/master/md_math_minuit2_doc_Minuit2.html#Minuit2Page. Accessed: 24.03.2022

[108] M. A. Vos et al., *"Charge collection with binary readout from a test beam perspective"*, URL: https://cds.cern.ch/record/685474

[109] R. Yonamine et al., *"Study and optimization of the spatial resolution for detectors with binary readout"*, *Nucl. Instrum. Meth. A* **830**, 130 (2016)

[110] The ROOT Authors, *"TEfficiency Class Reference"*, URL: https://root.cern.ch/doc/master/classTEfficiency.html. Accessed: 26.03.2022

[111] The ROOT Authors, *"TEfficiency Class Reference, Clopper Pearson Section"*, URL: https://root.cern.ch/doc/master/classTEfficiency.html#ae80c3189bac22b7ad15f57a1476ef75b. Accessed: 26.03.2022

[112] J. Dopke, Private Communication, 27.05.2022

[113] A. Rivetti, *"CMOS: Front-End Electronics for Radiation Sensors"*, CRC Press (2018)

[114] F. Campabadal et al., *"Beam tests of ATLAS SCT silicon strip detector modules"*, *Nucl. Instrum. Meth. A* **538**, 384 (2005)

[115] A. Abdesselam et al., *"The Data acquisition and calibration system for the ATLAS semiconductor tracker"*, *JINST* **3**, P01003 (2008)

[116] ATLAS Collaboration, *“ISTDAQ Documentation”*, URL: https://atlas-strips-itsdaq.web.cern.ch/index.html. Accessed: 27.05.2022

[117] P. Phillips, *“Design, development, characterisation and operation of ATLAS ITk strip staves”*, PhD thesis. University of Oxford, 2021

[118] L. A. M. Wiik-Fuchs et al., *“First Double-Sided End-Cap Strip Module for the ATLAS High-Luminosity Upgrade”*, *PoS (TWEPP2018)* **343**, 015 (2019)

[119] Y. Unno et al., *“ATLAS17LS – A large-format prototype silicon strip sensor for long-strip barrel section of ATLAS ITk strip detector”*, *Nucl. Instrum. Meth. A* **989**, 164928 (2021)

[120] ATLAS Collaboration, *“ATLAS ITk Electronics Specification: Autonomous Monitor And1 Control (AMACv2) ASIC”*, URL: https://edms.cern.ch/document/1809591/1

[121] B. Smodiš & L. Snoj, *“The JSI TRIGA Mark II Reactor, Slovenia”*, IAEA (2016), http://inis.iaea.org/search/search.aspx?orig_q=RN:47096894

[122] Institut Jožef Stefan Ljubljana, *“TRIGA Mark II research reactor”*, URL: https://www.eneep.org/about/ijs/. Accessed: 20.06.2022

[123] ATLAS Collaboration, *“ATLAS ITk Electronics Specification: Autonomous Monitor And1 Control (AMACStar) ASIC”*, URL: https://edms.cern.ch/document/1809591/1

[124] T. C. Gosart et al., *“Quality control testing of the AMAC ASIC for the HL-LHC ATLAS ITk Strip Detector”*, *JINST* **18**, C02013 (2023)

[125] A. Renardi, *“The silicon strip detector of the ATLAS Inner Tracker: from individual sensing units to multi-module petal structures”*, PhD Thesis. University of Dortmund, 2022

[126] M. Moll et al., *“Leakage current of hadron irradiated silicon detectors – material dependence”*, *Nucl. Instrum. Meth. A* **426**, 87 (1999)

[127] Craig Anthony, Sawyer, *“Project Status: ATLAS ITk Strip Overview”*, ITk Week 8-12 May, 2023. Geneva, Switzerland. URL: https://indico.cern.ch/event/1223748/#26-project-status

[128] E. Rossi, *“Characterization of Silicon Modules and Sensors for the ATLAS Inner Tracker Strip Detector”*, PhD thesis. DESY, 2020

[129] Craig Anthony, Sawyer, *“The ATLAS ITk Strip Detector System for the Phase-II LHC Upgrade”*, 15th "Trento" Workshop on Advance Silicon Radiation Detectors, 2020. URL: https://indico.cern.ch/event/813597/contributions/3727954/.

[130] M. Mikestikova, *“Evaluation of Bulk and Surface Radiation Damage of Silicon Sensors for the ATLAS Upgrade”*, *PoS (Vertex2014)* **227**, 050

[131] K. Hara et al., *"Charge collection study with the ATLAS ITk prototype silicon strip sensors ATLAS17LS"*, *Nucl. Instrum. Meth. A* **983**, 164422 (2020)

[132] A. Abba et al., *"Testbeam studies of pre-prototype silicon strip sensors for the LHCb UT upgrade project"*, *Nucl. Instrum. Meth. A* **806**, 244 (2016)

[133] S. Lindgren et al., *"Testing of surface properties pre-rad and post-rad of n-in-p silicon sensors for very high radiation environment"*, *Nucl. Instrum. Meth. A* **636**, S111 (2011)

[134] S. Spannagel & H. Jansen, *"GBL Track Resolution Calculator v2.0"*, URL: https://doi.org/10.5281/zenodo.48795

[135] Y. Unno et al., *"Beamtest of nonirradiated and irradiated ATLAS SCT microstrip modules at KEK"*, *IEEE Trans. Nucl. Sci.* **49**, 1868 (2002)

[136] S. Haywood, *"Helix fits with Stereo Measurements"*, URL: https://cds.cern.ch/record/685939

[137] *"2020 Update of the European Strategy for Particle Physics (Brochure)"*, `https://cds.cern.ch/record/2721370`

[138] W. Riegler, *"FCC-hh detector overview"*, URL: https://indico.cern.ch/event/727555/contributions/3461232/. The Fifth International Future Circular Collider (FCC) Conference. Accessed: 11.06.2022

[139] T. Hemperek, *"Exploration of advanced CMOS technologies for new pixel detector concepts in High Energy Physics"*, PhD thesis. Universität Bonn, 2018

[140] A. Hoffman et al., *"CMOS Detector Technology"*, *Exp. Astron.* **19**, 111 (2006)

[141] R. Turchetta et al., *"Large area CMOS image sensors"*, *JINST* **6**, C01099 (2011)

[142] S. E. Bohndiek et al., *"Characterization and Testing of LAS: A Prototype Large Area Sensor With Performance Characteristics Suitable for Medical Imaging Applications"*, *IEEE Trans Nucl Sci* **56**, 2938 (2009)

[143] LFoundry, *"LFoundry Technology 150nm"*, URL: http://www.lfoundry.com/en/technology. Accessed: 11.06.2022

[144] L. Diehl et al., *"Characterization of passive CMOS strip sensors"*, *Nucl. Instrum. Meth. A* **1033**, 166671 (2022)

[145] Suss MicroTech, *"Wafer prober Suss Microtech PA200HR"*, URL: https://www.suss.com/en. Accessed: 07.02.2023

[146] Tektronix, *"Keithley 237"*, URL: https://download.tek.com/datasheet/237.pdf. Accessed 07.02.2023

[147] Keysight, *"Keyseight HP 4284A"*, URL: https://www.keysight.com/de/de/product/4284A/precision-lcr-meter-20-hz-to-1-mhz.html. Accessed: 07.02.2023

[148] F. Lex, *"Electrical characterisation of a new type of silicon strip sensors"*, Bachelor thesis. Albert-Ludwigs-Universität Freiburg, 2020

[149] Kühn, Susane, *"Untersuchung der Strahlenhärte von Siliziumsensoren mit einer Betaquelle"*, Diploma thesis. Albert-Ludwigs-Universität Freiburg, 2006

[150] Michael Köhler, *"Double-Sided 3D Silicon Detectors for the High-Luminosity LHC"*, PhD thesis. Albert-Ludwigs-Universität Freiburg, 2011

[151] IAEA, *"Live Chart of Nuclides: nuclear structure and decay data"*, URL: https://www-nds.iaea.org/relnsd/vcharthtml/VChartHTML.html. Accessed: 14.06.2022

[152] R. Marco-Hernandez, *"A portable readout system for silicon microstrip sensors"*, *Nucl. Instrum. Meth. A* **623**, 207 (2010)

[153] S. Löchner & M. Schmelling, *"The Beetle Reference Manual - chip version 1.3, 1.4 and 1.5"*, `https://cds.cern.ch/record/1000429`

[154] The HDF Group, *"The HDF5® Library & file format"*, URL: https://www.hdfgroup.org/solutions/hdf5/. Accessed: 14.06.2022

[155] Niels G. Sorgenfrei, *"Investigation of Stitched Passive CMOS Strip Sensors"*, Master thesis. Albert-Ludwigs-Universität Freiburg, 2022

[156] The ROOT Authors, *"TProfile Class Reference"*, URL: https://root.cern.ch/doc/master/classTProfile.html. Accessed: 15.06.2022

[157] Leena Diehl, *"Investigation of Silicon Sensors Suitable for Collider Experiments in High Luminosity Environments"*, PhD thesis. Albert-Ludwigs-Universität Freiburg, 2022

[158] L. Diehl et al., *"Evaluation of passive CMOS strip sensors"*, *Nucl. Instrum. Meth. A* **1039**, 167031 (2022)

[159] J. Bronuzzi et al., *"Principle of the electrically induced Transient Current Technique"*, *JINST* **13**, P05021 (2018)

[160] V. Eremin, E. Verbitskaya & Z. Li, *"The origin of double peak electric field distribution in heavily irradiated silicon detectors"*, *Nucl. Instrum. Meth. A* **476**, 556 (2002), Proc. of the 3rd Int. Conf. on Radiation Effects on Semiconductor Materials, Detectors and Devices

[161] N. Sorgenfrei, Private Communication, 10.11.2022

[162] G. Kramberger, *"Reasons for high charge collection efficiency of silicon detectors at HL-LHC fluences"*, *Nucl. Instrum. Meth. A* **924**, 192 (2019)

[163] L. Wiik-Fuchs et al., *"Annealing studies of irradiated p-type sensors designed for the upgrade of ATLAS phase-II strip tracker"*, *Nucl. Instrum. Meth. A* **924**, 128 (2019)

[164] L. Diehl et al., *"Investigation of charge multiplication in irradiated p-type silicon strip sensors designed for the ATLAS phase II tracking detector"*, *Nucl. Instrum. Meth. A* **967**, 163900 (2020)

[165] ATLAS Collaboration, *"ATLAS ITK Strip Module Final Design Review"*, URL: https://indico.cern.ch/event/837485/

[166] ATLAS Collaboration, *"Production Readiness Review of the ITk Strip ABCStar"*, URL: https://indico.cern.ch/event/1078090/

[167] ATLAS Collaboration, *"ATLAS ITK Strip Barrel Modules Production Readiness Review"*, URL: https://indico.cern.ch/event/1269138/

[168] A. Rodriguez Rodriguez et al., *"Efficiency vs noise occupancy and residuals distribution of irradiated ATLAS ITk Short Strip module measured by DESY test beam in 2021: Dependence of efficiency and noise occupancy of irradiated ATLAS ITk Short Strip module and its residuals distribution studied at DESY-II Testbeam Facility in 2021"*, `https://cds.cern.ch/record/2798394`

Acknowledgments

I want to take a moment to express my sincere thanks to some incredible people who have been an integral part of my Ph.D. journey. First and foremost, I am immensely grateful to my supervisor Dr. Ulrich Parzefall and Prof. Jakobs. Thanks, Uli, for trusting in me, giving me this incredible opportunity, and becoming a good friend along this journey.

I owe a huge debt of gratitude to Dr. Jens Dopke. He has been an absolute lifesaver, always there to help me out and share his knowledge. Jens, I can not express how grateful I am. Thank you so much for everything.

Naturally, I must give a big shout-out to the group in Freiburg. To Cedric, Sven, Krzysztof, and Frank, thanks for all your support, the amazing conversations about everything, and the time together. You made this adventure a fun one. In addition, I would like to thank Frederik, Riccardo, Marc, Dennis, Carlos, Ines, Roman, Ilia, Christian, Karsten, Niels, Fabian, and Benedict for all the great moments over group discussions and coffee breaks and for the help that all of you gave me at many points during these years. I particularly want to thank Christina Skorek, who is the glue that holds the group together. Chris, I can not thank you enough for your support. To Leena, thanks for your unwavering support. Thanks for helping with so much German paperwork and language and for all your advice through these years. Thanks for being a fantastic colleague and office companion, for all the proofreading, assistance, and corrections but most importantly, thanks for your friendship. You have also been a lifesaver.

Outside Freiburg, I want to thank the ATLAS ITk test beam crew, especially Jiri, for making the test beam time, particularly the night shifts, so entertaining and for all the support over these years. To John, Jan-Hendrik, Radek, Callan, Getika, and Bruce for all the invaluable assistance with technical inquiries, proofreading and fruitful discussions. In addition, I want to thank Marta Baselga for her help with proofreading and encouragement and a former ITk Strip and current Littelfuse colleague Alessia Renardi for all her emotional support and positive vibes.

To the Cuban support team, Dariel, Elizabeth, Jose, and Marta (yes, I include you here). We have come a long way together and keep helping each other, even at a distance. Thanks for so many consultations and proofreading, but more importantly,

for always bringing that positive energy when I needed it the most.

Last but definitely not least, I want to thank my family for all the emotional support and motivation. Especially, I want to thank my mom Claribel, my aunt Editha, and Onkel Werner. You have been accompanying and supporting me my entire life, particularly during the hardest times of my studies. You have paved the way to what I am.

To my lovely wife, Annie, we started this journey together and have gone through thick and thin, and now, we are both becoming doctors. Thank you for always being there for me, and thanks for your love.